The Fabrication of Paper-based Multi-walled Carbon Nanotubes Electrode Sensors Using Inkjet Printer

Lancaster University

Saruta Deeprasert

This dissertation is submitted for the degree of
Doctor of Philosophy

October 2022

Department of Chemistry

‘Work hard in silence and let the success make a noise.’

Frank Ocean

Declaration

This thesis has not been submitted in support of an application for another degree at this or any other university. It is the result of my own work and includes nothing that is the outcome of work done in collaboration except where specifically indicated. Many of the ideas in this thesis were the product of discussion with my supervisor Professor Peter Fielden, and Professor Rob Short.

Abstract

Paper-based electrode sensors are low-cost, biodegradable and easy to fabricate, and are usually developed for single-use detection, to avoid cleaning and cross-contamination. Nanomaterials have gained wide interest as key components for paper-based electrode sensors, as they can be easily deposited onto paper substrates. The aim of this research is to prepare a water-based multi-walled carbon nanotubes (MWCNTs) ink for paper-based electrode sensor fabrication using a home inkjet printer (Canon PIXMA TS205). Different MWCNTs ink formulations were studied to identify the most compatible inks for inkjet printing. Pristine multi-walled carbon nanotubes functionalised with a carboxylic acid group mixed with sodium dodecyl sulphate provided the optimum homogeneity with high electrical conductivity and compatibility with the inkjet printer. This formulation was used to fabricate the MWCNTs-based electrode sensor on Whatman filter paper. However, one of the major challenges with paper-based sensors is water absorption by the paper substrate, making it inappropriate for multiple uses. Three types of coating, perflourocyclobutane (PFC), acrylic acid (AA) and allylamine (AAm), were plasma polymerised onto the paper substrate to enhance the paper substrate stability and electrode sensor performance. The purpose of using PFC is to make the paper substrate surface hydrophobic, to prevent water absorption that may degrade the electrode sensor, while AA and AAm are plasma polymerised to induce hydrophilicity to the surface of PFC-coated filter paper for MWCNTs printing and electrode sensor fabrication. The success of the plasma polymerisation technique and improved performance of the sensor was confirmed using a range of analytical techniques. This PhD project foreshadows the future development of paper-based sensors with high durability and enhanced performance.

Acknowledgements

First of all, I would like to thank Professor Peter Fielden and Professor Rob Short of Lancaster University for their supervision throughout this research project.

I would like to extend my gratitude to the members of my research group; Dr Alexandra Robson for the XPS characterisation and plasma polymerisation training and for providing guidance on XPS data interpretation, and Dr Nishtha Gaur for the guidance on the research chapter. I would also like to thank Dr Sara Baldock for SEM characterisation guidance and SEM data for my samples on this research project.

Outside of my research group, I would like to thank Dr Sussanah Coote, and Professor David Antonelli for taking part in the Panel meeting and providing guidance throughout this project.

I would like to thank my parents, Mrs Vilailuck Deeprasert and Mr Suchat Deeprasert, for providing me with the support and opportunities to pursue further studies on this research project.

Finally, I would like to thank all my friends, especially Dr Dhruv Trivedi for all his support and for making me have an amazing time during this PhD. I extend this gratitude to Miss Waramporn Pongrujaporn (Kwang) for her support and for keeping me sane.

Thank you to Charles Weir of Lancaster University, UK and to Kayla Friedman and Malcolm Morgan of the University of Cambridge for producing the Microsoft Word thesis template used to produce this document.

Contents

1 INTRODUCTION **1**

1.1 Thesis Aims and Objective 4

2 BACKGROUND AND LITERATURE REVIEW **5**

2.1 Nanotechnology 5

2.1.1 Types of Nanotechnology/Nanomaterial *5*

2.1.2 Advantages and Disadvantages of Nanotechnology *7*

2.2 CNTs 9

2.2.1 Types of CNTs *10*

2.2.1.1 Single-walled Carbon Nanotubes *11*

2.2.1.2 Multi-walled Carbon Nanotubes *13*

2.2.2 Properties of CNTs *13*

2.2.2.1 Mechanical Properties *13*

2.2.2.2 Thermal Properties *14*

2.2.2.3 Chemical Properties *14*

2.2.2.4 Electrical Properties *14*

2.2.3 Application of CNTs *15*

2.2.3.1 Medical Applications *15*

2.2.3.2 Electronic Applications *16*

2.2.3.3 Environmental Applications *16*

2.2.4 CNTs for Biosensor Fabrication (Relationship between Connectivity and Electrical Conductivity) *18*

2.2.5 Sidewall Functionalisation of CNTs *19*

2.2.6 Dispersion of CNTs in Organic Solvents *19*

2.2.7 Dispersion of CNTs in Aqueous Solvents *20*

2.3 Overview of inkjet Printing Deposition Techniques 21

2.3.1 Commercial Inkjet Printer *21*

2.3.1.1 Drop-on-Demand Inkjet Printer *21*

2.3.1.1.1 Thermal Inkjet Printing Technology *22*

2.3.1.1.2 Piezoelectric Inkjet Printing Technology *23*

2.4 Paper-based CNTs Electrode Sensor Devices 25

2.4.1 State of the Art: Paper Substrates 25
2.4.2 Paper-based Device Applications 26
2.4.3 Components of Electrochemical Sensor 28
2.4.4 Electrochemical Sensor Electrode Design 28
2.4.5 Types of the Electrochemical Sensor 29
2.4.5.1 Potentiometric Sensors 29
2.4.5.2 Conductometric Sensors 29
2.4.5.3 Amperometric Sensors 30
2.5 Plasma Polymerisation (PP) 30
2.5.1 Plasma 30
2.5.2 Cold Plasma (Non-Thermal/Equilibrium Plasma) 31
2.5.3 Formation of Polymer in Plasma 32
2.5.3.2 Stages of Plasma Polymerisation 32
2.5.3.2 Different Types of Monomers Used in Plasma Polymerisation 33
2.5.4 PP Apparatus 33
2.5.5 Factors Affecting PP 34
2.6 Surface Analysis and Characterisation 35
2.6.1 X-Ray Photoelectron Spectroscopy (XPS) 35
2.6.1.1 Principles 36
2.6.1.1.1 Photoelectron Generation 36
2.6.1.1.2 Auger Electrons 37
2.6.1.1.3 Surface Sensitivity 38
2.6.1.2 Chemical Environment 38
2.6.1.3 The Chemical Shift Effect 38
2.6.1.3.1 C1s Coreline shift 38
2.6.1.3.2 N1s Coreline Shift 39
2.6.2 Contact Angle (CA) Measurement 40
2.6.3 SEM Characterisation 40
3 MWCNTS INK FORMULATION PREPARATION AND CHARACTERISATION 42
3.1 Introduction 42
3.2 Experimental and Method 44
3.2.1 Material and Equipment 44

3.2.2 XPS Characterisation (Surface Analysis) *44*

3.2.3 Resistance Measurement *45*

3.2.4 Methodology *46*

3.2.4.1 MWCNTs Ink Formulation *46*

3.2.4.1.1 Formulation 1.1: Sidewall Functionalisation with Diluted Acid Mixture Through Magnetic Stirring *46*

3.2.4.1.2 Formulation 1.2 & 1.3: Preparation of Pristine-MWCNTs in Aqueous Solution with SDS/SDBS Surfactant *46*

3.2.4.1.3 Formulation 1.4: Pristine-MWCNTs-COOH Dispersed in Aqueous Solution Using SDS Surfactant *46*

3.2.4.2 Printer Cartridge Preparation *47*

3.2.4.3 CNTs Ink Printing Observation *47*

3.2.4.4 CNTs Ink Formulation Observation and Characterisation *47*

3.2.4.4.1 SEM Characterisation *47*

3.2.4.4.2 XPS Characterisation *48*

3.2.4.4.3 Resistance Measurement *48*

3.3 Results and Discussion 49

3.3.1 Ink Formulation Observation *49*

3.3.1.1 Formulation 1.1 .... *49*

3.3.1.1.1 Critical Concentration Determination Using Resistance Measurement *49*

3.3.1.1.2 SEM Characterisation *50*

3.3.1.2 Formulation 1.2 and Formulation 1.3 .... *51*

3.3.1.2.1 SEM Characterisation *51*

3.3.1.3 Formulation 1.4 .... *52*

3.3.1.3.1 Effects of Surfactant towards Ink Formulation *52*

3.3.1.3.2 SEM Characterisation *53*

3.3.1.3.3 XPS Characterisation *54*

3.3.2 Thermal Inkjet Printer and Piezoelectric Inkjet Printer *55*

3.3.2.1 Epson Inkjet Printer *55*

3.3.2.1.1 SEM Characterisation *56*

3.3.2.2 Canon Inkjet Printer *57*

3.3.2.2.1 Formulation 1.1 .... *58*

3.3.2.2.2 Formulation 1.4 ... *59*

3.4 Conclusion ... *61*

4 PAPER-BASED ELECTRODE SENSORS AND PAPER SUBSTRATES COMPARISON 62

4.1 Introduction ... 62

4.2 Experimental and Method ... 64

4.2.1 Material and Equipment ... *64*

4.2.2 Anodic Stripping Voltammetry (ASV) Analysis ... *64*

4.2.3 Methodology ... *65*

4.2.3.1 Observation of the Paper Substrate Interaction with the Formulated CNTs Ink ... *65*

4.2.3.2CNTs Printing on Different Types of the Paper Substrate ... *65*

4.2.3.3 Characterisation ... *65*

4.2.3.3.1 SEM Characterisation ... *65*

4.2.3.3.2 Resistance Measurement ... *66*

4.2.3.3.3XPS Characterisation ... *66*

4.2.3.3.4 ASV Analysis ... *66*

4.3 Results and Discussion ... 67

4.3.1 Paper Substrates Interaction Observation ... *67*

4.3.2 Fabricated Paper-based Electrodes and Printing Observation ... *68*

4.3.3 SEM Characterisation ... *69*

4.3.3.1 Fabricated CNTs Electrode Sensors ... *69*

4.3.3.2 Untreated Paper Substrates ... *71*

4.3.4 Resistance Measurement ... *71*

4.3.5 XPS Characterisation ... *72*

4.3.5.1 Untreated Whatman Filter Paper Grades 1 and 3 ... *72*

4.3.6 ASV Analysis ... *74*

4.4 Conclusion ... 77

5 PLASMA POLYMERISATION ON FILTER PAPER TO ENHANCE ELECTRODE SENSOR PERFORMANCE AND STABILITY USING PFC AND AA 79

5.1 Introduction ... 79

5.2 Experimental and Method ... 82

5.2.2 Plasma Polymerisation ... 82
5.2.3 CA Measurement ... 83
5.2.4 Methodology ... 84
5.2.4.1 PP on Whatman Filter Paper Grade 3 and Si Wafer (PFC and AA Coating) ... 84
5.2.4.2 PFC Plasma Coating ... 84
5.2.4.3 AA Plasma Coating ... 84
5.2.4.4 CNTs Inkjet Printing ... 84
5.2.4.5 Surface Characterisation ... 85
5.2.4.5.1 CA Measurement ... 85
5.2.4.5.2 XPS Characterisation ... 85
5.2.4.5.3 SEM Characterisation ... 85
5.2.4.5.4 Resistance Measurement ... 85
5.3 Results and Discussion ... 87
5.3.1 Interaction Between Plasma Coated Filter Paper and Water Solution ... 87
5.3.2 CA Measurement ... 88
5.3.2.1 PFC Coating ... 88
5.3.2.2 AA Coating ... 90
5.3.2.3 AA-PFC Coating ... 91
5.3.3 SEM Characterization ... 92
5.3.4 XPS Characterization ... 93
5.3.4.1 Comparison between PFC-Coated Filter Paper and Si Wafer ... 94
5.3.4.2 AA-PFC Filter Paper ... 99
5.3.4.3 CNTs Electrode Sensors on AA-PFC Filter Paper ... 102
5.3.4.3.1 XPS Characterisation of CNTs Electrode Sensor on AA-PFC Filter Paper ... 102
5.3.4.3.2 Resistance Measurement of CNTs Electrode Sensor on AA-PFC Filter Paper ... 104
5.4 Conclusion ... 106

6 PLASMA POLYMERISATION OF AAM ON PFC-COATED FILTER PAPER 108

6.1 Introduction 108

6.2 Experimental and Method 110

6.2.1 Material and Equipment 110

6.2.2 Methodology 110

6.2.2.1 PP on Whatman Filter Paper Grade 3 (PFC and AAm) 110

6.2.2.1.1 AAm Plasma Coating 110

6.2.2.2 CNTs Inkjet Prin AAm-PFC Filter paperting 110

6.2.2.3 Coated Filter Paper and CNTs Electrode Sensor Observation and Characterisation 110

6.2.2.3.1 CA Measurement 110

6.2.2.3.2 XPS Characterisation 110

6.2.2.3.3 Resistance Measurement 111

6.3 Result and Discussion 112

6.3.1 Contact Angle Measurement 112

6.3.2 XPS Characterisation 113

AAm-PFC Filter paper 113

6.3.2.2 CNTs Electrode Sensors on AAm-PFC Filter Paper 117

6.3.2.3 CNTs Electrode Sensors Fabrication on AAm-PFC Filter Paper .. 121

6.3.3 Resistance Measurement of the Fabricated Electrode Sensor on 5 W AAm-PFC Filter Paper 122

6.4 Conclusion 124

7 CONCLUSIONS 125

8 FURTHER WORKS 128

9 REFERENCES 130

10 APPENIDICES 147

List of Tables

Table 2.1: Types of nanomaterial 6

Table 2.2: Advantages and disadvantages of nanotechnology 7

Table 2.3: Differences between SWCNTs and MWCNTs 10

Table 2.4: Types and properties of the paper substrate 25

Table 2.5: Binding energy of carbon chemical state (reference for C1s spectra) [182,190,193] 39

Table 3.1: Atomic percentages of CNTs ink (formulation 1.4) on Whatman filter paper grade 1 54

Table 3.2: Area percentages of CNTs ink (formulation 1.4) on Whatman filter paper grade 1 54

Table 4.1: Atomic percentages of untreated Whatman filter paper grade 1 and 3 74

Table 4.2: Percent composition of untreated Whatman filter paper grade 1 and 3 74

Table 5.1: CAs between DI water/CNTs ink and AA-coated substrates (filter paper and Si wafer) at 5 W and 50 W for 10 min 91

Table 5.2: CAs between DI water/CNTs ink and AA-PFC substrates (filter paper and Si wafer) at 5 W and 50 W for 10 min 92

Table 5.3: Atomic percentages of untreated filter paper, PFC-coated filter paper at 20 W for 10 min and AA-coated filter paper at 5 W and 50 W for 10 min, 2 x 10^{-1} mbar 94

Table 5.4: Atomic percentages of PFC-coated Si wafer at 20 W for 10 min and AA-coated silicon wafer at 5 W, and 50 W for 10 min, 2 x 10^{-1} mbar 96

Table 5.5: Percent composition of untreated filter paper, PFC-coated filter paper at 20 W for 10 min and AA-coated filter paper at 5 W, 10 W and 50 W for 10 min, 2 x 10^{-1} mbar 98

Table 5.6: Percent composition of PFC coated silicon wafer at 20 W for 10 min and AA-coated silicon wafer at 5 W, 10 W and 50 W for 10 min, 2 x 10^{-1} mbar ... 98

Table 5.7: Atomic percentages of AA-PFC filter paper at 5 W, and 50 W for 10 min, 2 x 10^{-1} mbar 99

Table 5.8: Area percentages of acrylic acid coated on PFC filter paper at 5 W and 50 W for 10 min, 2 x 10^{-1} mbar 100

Table 5.9: Atomic percentages of CNTs ink droplet on untreated filter paper and fabricated CNTs electrode sensors on untreated filter paper, 5 W and 50 W AA-PFC filter papers 102

Table 6.1: XPS reference table with C1s binding energy for AAm 111

Table 6.2: CA measurement of AAm-PFC filter paper at different coating conditions with DI water and CNTs ink 112

Table 6.3: Area percentages of AAm-PFC filter paper at 5 W, and 20 W (2 x 10^{-1} mbar, 10 min) 113

Table 6.4: Atomic percentages of AAm-PFC filter paper at 5 W, 10 W, and 20 W (2 x 10^{-1} mbar, 10 min) 116

Table 6.5: N1s spectra atomic percentages of AAm-PFC filter paper at 5 W, 10 W, and 20 W (2 x 10^{-1} mbar, 10 min) 116

Table 6.6: Atomic percentages of fabricated CNTs electrode sensor on AAm-PFC filter paper at 5 W, and 20 W (2 x 10^{-1} mbar, 10 min) 120

Table 6.7: Area percentages of fabricated CNTs electrode sensor on AAm-PFC filter paper at 5 W, and 20 W (2 x 10^{-1} mbar, 10 min) 120

List of Figures

Figure 2.1: A timeline indicating various milestones in the discovery of CNTs 9

Figure 2.2: Structure of a) SWCNTs and b) MWCNTs (Russian Doll Model) 10

Figure 2.3: Types of CNTs 11

Figure 2.4: Chiral vector of SWCNTs 12

Figure 2.5: DOD thermal inkjet printing technology 22

Figure 2.6: DOD piezoelectric inkjet printing technology 23

Figure 2.7: Different types of piezoelectric inkjet printing techniques 24

Figure 2.8: Application of paper-based sensing devices [15–17,132–134] 27

Figure 2.9: Types of plasma in relation to electron density (N_e), energy (E), and temperature (K) [152] 31

Figure 2.10: Schematic diagram of the PP reactor used in this PhD research [160] . 34

Figure 2.12: Schematic diagram of XPS 36

Figure 2.12: Schematic diagram of XPS 37

Figure 2.13: Schematic diagram of CA measurement [160] 40

Figure 2.14: Schematic diagram of SEM characterisation 41

Figure 3.1: Schematic diagram of digital multimeter 45

Figure 3.2: Side-wall functionalised MWCNTs in water solution (5mg/mL) 49

Figure 3.3: Resistance measurement of *formulation 1.1* at 2.5 mg/mL to 6.0 mg/mL (1 cm length between probes measurement) 50

Figure 3.4: SEM images of formulation 1.1 (MWCNTs-COOH in DI water) at 5.0 mg/mL concentration on Whatman filter paper grade 1 51

Figure 3.5: SEM images of formulation 1.2 (pristine-MWCNTs with SDS in DI water) on Whatman filter paper grade 1 52

Figure 3.6: SEM images of formulation 1.3 (pristine-MWCNTs with SDBS in DI water) on Whatman filter paper grade 1 52

Figure 3.7: SEM images of formulation 1.4 (7 wt% SDS and 10 wt% MWCNTs-COOH in DI water) on Whatman filter paper grade 1 53

Figure 3.8: a) Wide and b) C1s spectra of CNTs ink (formulation 1.4) on Whatman filter paper grade 1 54

Figure 3.9: Formulation a) 1.1 (MWCNTs-COOH in DI water), b) 1.2 (pristine-MWCNTs with SDS in DI water), and c) 1.3 (pristine-MWCNTs with SDBS in DI water) printed on filter paper by Epson inkjet printer (50 printing cycles) 56

Figure 3.10: SEM images of a) 1.1, b) 1.2, and c) 1.3 printed on Whatman filter paper grade 1 using Epson inkjet printer (50 printing cycles) 57

Figure 3.11: a) Formulation 1.1 printed on filter paper by Canon inkjet printer (50 printing cycles) and b) SEM images of formulation 1.1 printed on filter paper 58

Figure 3.12: a) Electrode template, b) formulation 1.4 printed on Whatman filter paper grade 1 (50 printing cycles), SEM images of the electrode sensor, c) top-view, and d) and e) cross-section 59

Figure 3.13: Resistance measurement of formulation 1.4 printed on Whatman filter paper grade 1 (50 printing cycles) 60

Figure 4.1: A schematic of the ASV analysis setup 65

Figure 4.2: CNTs ink dropped on a) Whatman filter paper grade 1, b) glossy photo paper, and c) matte photo paper 67

Figure 4.3: Formulated CNTs ink printed on a) Whatman filter paper grade 1, b) glossy photo paper at 20 – 50 printing cycles, and c) Whatman filter paper grade 3 printing repeats at 50 printing cycles 68

Figure 4.4: Fabricated CNTs electrode sensor on Whatman filter paper grade 3 69

Figure 4.5: SEM top-view images of fabricated CNTs electrode sensors on a) Whatman filter paper grade 1, b) Whatman filter paper grade 3, and c) glossy photo paper 70

Figure 4.6: SEM top-view morphology of a) Whatman filter paper grade 3, and b) glossy photo paper 71

Figure 4.7: Resistance measurement of the fabricated CNTs electrode sensors on Whatman filter paper grade 1 and 3, and glossy photo paper 72

Figure 4.8: i) Wide spectra and ii) C1s spectra of untreated a) Whatman filter paper grade 1, and b) Whatman filter paper grade 3 73

Figure 4.9: ASV analysis of fabricated CNTs electrode sensors on Whatman filter paper grade 3 at 5 sec to 60 sec deposition time (condition: 10 ppm Cu in acetate) 75

Figure 4.10: ASV analysis of fabricated CNTs electrode sensors on Whatman filter paper grade 3 at 5 sec deposition time (condition: 10 ppm Cu in acetate)... 75

Figure 5.1: PP process of PFC and AA on Whatman filter paper grade 3 80

Figure 5.2: Structure of a) PFC and b) AA. 81

Figure 5.3: Plasma reactor 82

Figure 5.4: CA measurement system 83

Figure 5.5: a) untreated filter paper, b) PFC-coated filter paper (20 W, 2×10^{-1} mbar for 10 min), c) AA-PFC filter paper (50 W, 2×10^{-1} mbar for 10 min) dropped in water solution, d) water dropped on PFC-coated filter paper, and e) PFC-coated filter paper in water solution after one month 87

Figure 5.6: CA measurement of a) untreated filter paper and b) PFC coated filter paper (coating condition: 20 W, 2x10^{-1} mbar for 10 min) with i) DI water and ii) CNTs ink. 89

Figure 5.7: CA measurement of a) untreated Si wafer and b) PFC coated Si wafer (coating condition: 20 W, 2x10^{-1} mbar for 10 min) with i) DI water and ii) CNTs ink. 90

Figure 5.8: SEM images of untreated filter paper a) top view and b) cross-section, PFC-coated filter paper c) top view and d) cross-section and AA-PFC filter paper e) top view and f) cross-section. 93

Figure 5.9: a) wide spectra and b) C1s spectra of PFC-coated filter paper at 20W for 10 min, 2 x 10^{-1} mbar 94

Figure 5.10: a) wide spectra and b) C1s spectra of PFC-coated Si wafer at 20W for 10 min, 2 x 10^{-1} mbar 94

Figure 5.11: i) wide spectra and ii) C1s spectra of AA-PFC coated filter paper at a) 5 W, and b) 50 W for 10 min, 2 x 10^{-1} mbar 99

Figure 5.12: CNTs printed on a) untreated filter paper, b) 5 W AA-PFC filter paper and c) 50 W AA-PFC filter paper (AA coating condition: 5 10 min, 2 x 10 $^{-1}$ mbar) 102

Figure 5.13: Wide spectra of CNTs printed on a) untreated filter paper, b) 5 W, and c) 50 W AA-PFC filter paper, 10 min, 2 x 10 $^{-1}$ mbar 103

Figure 5.14: Resistance measurement of CNTs printed on 5 W AA-PFC filter paper and untreated filter paper 104

Figure 6.1: Chemical structure of allylamine [202] 108

Figure 6.2: Wide spectra of AAm-PFC filter paper (5 W, and 20 W at 10 min, 2 x 10 $^{-1}$ mbar) 113

Figure 6.3: C1s spectra of a) 5 W and b) 20 W AAm-PFC filter paper (10 min, 2 x 10 $^{-1}$ mbar)....115

Figure 6.4: N1s spectra of AAm-PFC filter paper at 5 W, 10 W, and 20 W (2 x 10^{-1} mbar, 10 min)....116

Figure 6.5: Wide spectra of CNTs on AAm-PFC filter paper at 5 W, and 20 W, 2 x 10^{-1} mbar, 10 min. 117

Figure 6.6: C1s spectra of CNTs on AAm-PFC filter paper at a) 5 W, and b) 20 W, 2 x 10^{-1} mbar, 10 min....118

Figure 6.7: CNTs electrode sensor on a) 5 W, and b) 20 W AAm-PFC filter paper (10 min, 2 x 10 $^{-1}$ mbar)....121

Figure 6.8: Resistance measurement of the fabricated electrode on untreated filter paper, 5 W AAm-PFC filter paper and 5 W AA- filter paper....122

List of Abbreviations and Acronyms

AA	Acrylic acid
AAm	Allylamine
ASV	Anodic stripping voltammetry analysis
CNTs	Carbon nanotubes
COO-, COOH	Carboxyl group
COOH/R	Carboxylate groups
(n,m)	Chiral index
c	Chiral vector
CT	Computerised tomography
CA	Contact angle
CEA	Colorectal cancer marker
CE	Counter electrode
DOD	Drop-on-demand
AFP	Hepatocarcinoma marker
ISFET	Ion-selective field-effect transistor
MRI	Magnetic resonance imaging
MWCNTs	Multi-walled carbon nanotubes
MWCNTs-COOH	Multi-walled carbon nanotubes functionalised with the carboxylic acid group
Nm	Nanometre

1D	One-dimension
pL	Picolitre
PP	Plasma polymerisation
PFC	Perflourocyclobutane
PP	Polypropylene
PDMs	Polydimethylsiloxane
PS	Polystyrene
PVC	Polyvinyl chloride
PVP	Poly(vinyl pyrrolidone)
(a_1, a_2)	Primitive lattice vector
Pristine-MWCNTs	Pristine multi-walled carbon nanotubes
Pristine-MWCNTs-COOH	Pristine multi-walled carbon nanotubes functionalised with the carboxylic acid group
rhBMP-2	Recombinant bone morphogenetic protein-2
REDOX	Reduction and oxidation reaction
RE	Reference electrode
SEM	Scanning electron microscope
SAM	Self-assembled monomer
SWCNTs	Single-walled carbon nanotubes
SDBS	Sodium dodecyl benzenesulfonate
SDS	Sodium dodecyl sulfate

3D	Three-dimension
2D	Two-dimension
WE	Working electrode
XPS	X-ray photoelectron spectroscopy
0D	Zero-dimension

1 Introduction

Nanotechnologies and nanomaterials are developing rapidly and providing many benefits to various fields, including environmental, medical, and agricultural applications [1]. The main advantage of nanomaterials is their small size, allowing them to interact with the surrounding materials more reactively than larger-scale material (bulk material) due to the highly enhanced surface contact area [1]. Nanomaterials range from 1 to 100 nanometres (nm) in size and can be categorised into four main types: nanowires, nanotubes, nanomembranes and nanopowders [2]. Each type of nanomaterial varies in structure, purposes, and application. Nanowires are nanomaterials ranging from a few micrometres to centimetres in length with random orientation [3,4]. They are commonly used to electrically detect species with high sensitivity. Nanotubes are similar to nanowires but higher in the diameter-to-length ratio (aspect ratio) [5]. They are an outstanding nanomaterial due to their strength and flexibility [6]. Nanotubes such as carbon nanotubes (CNTs) have been applied in many applications, including vehicle manufacturing and electrochemical sensors [7]. Nanomembranes are membranes with a thickness within the nm range (1 nm -100 nm) [8]. They have a large surface area suitable for liquid and gas filtration [3]. Nanopowder has a high surface area due to its high numbers of particles at the nanometre scale. They are used in applications such as bone repair and UV-resistant plastic [3].

This research thesis aims to use CNTs as a conductive material for electrochemical sensor fabrication. An extensive literature survey on CNTs, including types, deposition techniques and substrate preparation, has been discussed in *Chapter 2*. Briefly, CNTs are rolled-up graphene sheet(s) ranging from 1 nm to 100 nm in diameter [9]. Mainly, CNTs may be categorised into two major types: single-walled carbon nanotubes (SWCNTs) and multi-walled carbon nanotubes (MWCNTs) [10]. SWCNTs consist of a rolled-up graphene sheet, whereas

MWCNTs are composed of two or more concentric layers of the rolled-up graphene sheet(s) [11,12]. The significant difference between these two CNTs lies in their chemical stability. SWCNTs are more likely to be affected and damaged under harsh chemical and physical conditions than MWCNTs. For instance, in the acid mixture (a mixture of sulfuric acid and nitric acid), SWCNTs are liable to being degraded or shortened, which may change the SWCNTs properties, while the MWCNTs remained due to multiple layers of the graphene sheet(s); therefore, MWCNTs are more likely to withstand harsh chemical and physical conditions by maintaining their intrinsic properties. Besides, MWCNTs are higher in mechanical stability and have a lower production cost [13]. Hence, MWCNTs remain a desirable choice as a conductive material for many new technologies, especially electrochemical sensors [13,14]. They have been used to analyse specified chemicals, such as copper (Cu^{2+}) and nitrogen dioxide (NO_2), in food and clinical industries, aqueous system monitoring and applications of environmental interest [15–17].

Depending on the area of application, the CNTs-based electrode sensors need surface modification and appropriate fabrication techniques. These include side-wall functionalisation, organic solvent dispersion, and aqueous dispersion using surfactant [18,19]. These techniques will be explained further in *chapter 2*. Moreover, an appropriate substrate also reduces the surface electrical resistance and allows better interaction with the conductive material.

In this PhD project, paper substrates have been utilised as a base to fabricate a CNTs-based electrode sensor. Paper substrates have a long history with electronic applications and analytical measurements as they are low-cost and mass-producible, flexible, lightweight, disposable, and compatible with various materials [18,23,24]. The paper substrate material, thickness, pore size and porosity also play an essential role in determining the performance of the electrode sensor [15,20]. It would react differently to various types of added materials depending on the characteristic of the material.

The deposition technique affects the conductive material distribution and electrochemical sensor performance. Therefore, it is essential to deposit the conductive material homogeneously on the substrate surface to create consistent conductivity throughout the electrochemical sensor. Electrode sensors are fabricated by different deposition processes depending on their specific purpose and application. For example, drop-casting, screen-printing, inkjet printing, electrochemical deposition, and thermal decomposition have been reported as effective deposition techniques [21,22].

In previous research, inkjet printers have been used to fabricate electrode sensors, as they provide high electrode geometry accuracy and precision, are easy to operate, and are low cost [23]. They can be categorised into two major printing technologies: thermal and piezoelectric printing systems [24]. The systems differ in their ink ejection process [25] and will be discussed in *Chapter 2*. In inkjet printing, the printing head deposits the ink onto the substrate without touching the surface. This contactless deposition prevents scratches or changes in the substrate surface properties [26]. Therefore, this PhD project investigates how to use home-inkjet printer to print MWCNTs ink onto paper substrates.

As stated previously, the paper substrate will be used to fabricate the electrode sensor in this PhD project due to its high sensitivity, low cost, and ease of use [27]. However, they pose major drawbacks in terms of durability. Due to their hydrophilic nature, paper substrates are likely to degrade over time when submerged into a sample solution. To overcome this, plasma polymerisation (PP) will be investigated in this research to impart hydrophobicity (to prevent degradation in an aqueous environment) and hydrophilicity (to allow the CNTs printing). PP of perflourocyclobutane (PFC), acrylic acid (AA) and allylamine (AAm) on the paper substrate will be studied. PP aims to modify the surface properties of the substrate material to achieve desired properties without interfering with their bulk properties (e.g., morphology and porosity) [28]. As a result, paper-based electrochemical sensors will be fabricated with more extended durability.

1.1 Thesis Aims and Objective

This research aims to fabricate paper-based MWCNTs electrode sensors using a home inkjet printer. The objectives of this thesis are as follows:

- To identify the appropriate MWCNTs ink formulation (for inkjet printing) by comparing various ink formulations with side-wall functionalisation of MWCNTs and pre-functionalised MWCNTs dispersed in DI water using SDS and sodium dodecyl benzenesulfonate (SDBS) surfactants. The effect of MWCNTs diameter and length will be studied.

- To identify the most appropriate paper substrate for paper-based electrode sensor fabrication by inkjet printing. Whatman filter paper grades 1 and 3, parchment paper, matte paper and glossy paper will be studied.

- To fabricate and characterise fully paper-based MWCNTs electrode sensor devices and determine possible routes for improving the performance of paper-based devices.

- To enhance the durability and stability of the paper substrate by using PP of PFC, AA and AAm. This is to improve the electrode sensor durability, reproducibility, and performance by modifying the surface characteristic of the paper substrate without changing the paper morphology or porosity.

2 Background and Literature Review

2.1 Nanotechnology

Nanotechnology is the study of materials in a nanometre scale size, ranging from 1 to 100 nanometres. It is applied in many fields of study, including physics, chemistry, material science, and engineering [9] . Nanotechnology controls the material at its atomic scale and utilises the structure, characteristic, design, production, material application, devices, and system [29–31]. Therefore, it is an innovation for energy technology [32], environmental monitoring [29], manufacturing industries [33], electronic and optoelectronic fields [30] and even medical industries [32].

The properties of nanomaterials lie between bulk material and atomic-scale material characteristics [34]. Due to the increase in the surface area-to-mass/volume ratio, the material is more reactive; therefore, nanomaterials are appropriate for applications where a surface area or particle size plays an essential role in the performance [30,35]. The surface area increases as the size of the particle decrease; as a result, more active sites are presented and change or enhance the properties of that material [36].

2.1.1 Types of Nanotechnology/Nanomaterial

Different types of nanomaterial provide distinct chemical, physical and mechanical properties, depending on their morphology, structure, size, and shape, to serve varieties of applications. Nanomaterials are classified into four types according to their structural dimension, which includes zero (0D), one (1D), two (2D), and three (3D) dimensional nanomaterials [37]. Each dimension consists of different nanomaterials, which are being used in research fields and applications, as shown in **Table 2.1**.

Table 2.1: Types of nanomaterial

Dimension	**Description**	**Types**	**Applications**
0D nanomaterials	All dimensions are within the nanoscale (1-100 nm)	Nanoparticles	• Biomedical and pharmaceutical sector: cancer treatment (iron nanoparticles) [38], drug delivery systems (liposomes and micelles) [39], intravenous iron therapy (ferric nanoparticles stabilised in iron-oligosaccharide) [40], and covid-19 vaccine (lipid nanoparticles-mRNA) [41]
1D nanomaterials	One dimension larger than the nanoscale. Two dimensions within the nanoscale	Nanowire, nanorod, nanofiber, and nanotubes	• Tissue engineering (titanium dioxide (TiO_2) nanowire) [42], drug delivery (iron-based core-shell nanowire) [43], cancer diagnosis (silicon nanowire) [44], optical sensor (single polymer nanowire) [45], air filtration (iron oxide nanowire) [46], and sensors and flexible transparent electrodes preparation (copper nanowires) [47] • Energy storage (titanium dioxide nanorod) [48] • Biomedicine, flexible electronic devices (ex. soft bioelectronic) [37], and electrochemical electrode sensors (carbon nanotubes) [49]
2D nanomaterials	Two dimensions are larger than the nanoscale. One dimension within the nanoscale	Nanolayer, nanocoating, nanomembrane and plate-like shape nanofilm	• Soft optoelectronics (improving touch screens for phones and tablets) (graphene coating) [37,50] • Water and wastewater treatment using ultrafiltration techniques (tangential flow filtration (TFF)) to separate biomolecules and purification of drinking water (nanomembrane) [3,51] • Hard tissue replacement (Nanocrystalline TiO_2 coating) [52] • Biosensor (self-assembled monolayer (SAM)) [53]
3D nanomaterials	No dimension within the nanoscale. Combination of 1D and 2D nanomaterials	Biological nanomaterials, suspension and dispersion, composites, and polymer	• Drug delivery in the form of exosomes or regenerative medicine (biological nanomaterials) [54] • Paints and coatings, inks, drug delivery, and ceramic and nanocomposite processing (suspension and dispersion) [55] • Automotive sector [56], construction, and electronics (composites containing two or more components of nanoscale) • Solar cells, information processing, nanoscale electronic devices and new sensor technologies (polymer)

2.1.2 Advantages and Disadvantages of Nanotechnology

Even though nanotechnology has been used in various fields and applications due to the enhanced properties and performances over bulk material, the benefits do not come without some drawbacks [57]. Many reviews have been written about this to gain more understanding the nanotechnology and are summarised in the table below (**Table 2.2**).

Table 2.2: Advantages and disadvantages of nanotechnology

Advantages	**Disadvantages**
Manufacturing: • Enhances material properties [58] • Lighter and stronger with insulating properties and durability [58] • Smaller size product with similar or better properties compared to bulk material [34] Energy and Electronic: • New alternative sources of energy [59] • Transforms energy usage techniques and enhances fuel production efficiency [58] • Reduced production cost of energy generation [58] • Innovation of energy storage devices with high efficiency [59] • Ability to construct the electronic precisely at an atomic scale where smaller size electronic devices may be constructed [60] Medical: • Ability to construct a nanorobot for medical application, which makes the surgery more accurate and less time-consuming [61] • Ability to identify infected area more accurately or precisely due to better imaging [58] • Ability to repair injury cell-by-cell [25] • Ability to refine drugs and adjust the properties at a molecular scale [58]	Health issues: • Lack of accurate knowledge of health issues [62] • Higher possibility of inhalation, which could be harmful to human health, especially under long-term exposure [63] • Increase mass poisoning to human health if the coating of nanomaterial wears off and produces harmful compounds [2] Environmental effects: • Creates new toxic waste and pollutants [64] • Increases air and water pollution [64] • Lack of knowledge on the possible harm to the environment [64] Economics: • High research cost depending on the material used [65]

• Drugs become more effective and have fewer side effects [59] Environmental: • Ability to detect and remove harmful contaminants in a cheaper and more effective way [51] • Ability to filter specific sized materials/compounds [51] Economics: • With higher supply production of nanomaterial, the material cost decreases [58]	

2.2 CNTs

In nanotechnology and nanomaterials, nanotubes are among the most outstanding nanomaterials due to their flexibility and physical and chemical stability. There are different types of nanotubes, serving various applications and purposes, including silicon carbide (SiC) tubes, silicon tubes, and carbon nanotubes (CNTs), for example [11]. CNTs are commonly used in electrochemical fields as they provide high flexibility, mechanical and thermal strength, and high electrical conductivity. The discovery of CNTs was not until 1952 when the first clear images of CNTs were presented by L.V. Radushkevich and V. M. Lukyanovich [66]. **Figure 2.1** summarises the timeline of the discovery of CNTs briefly.

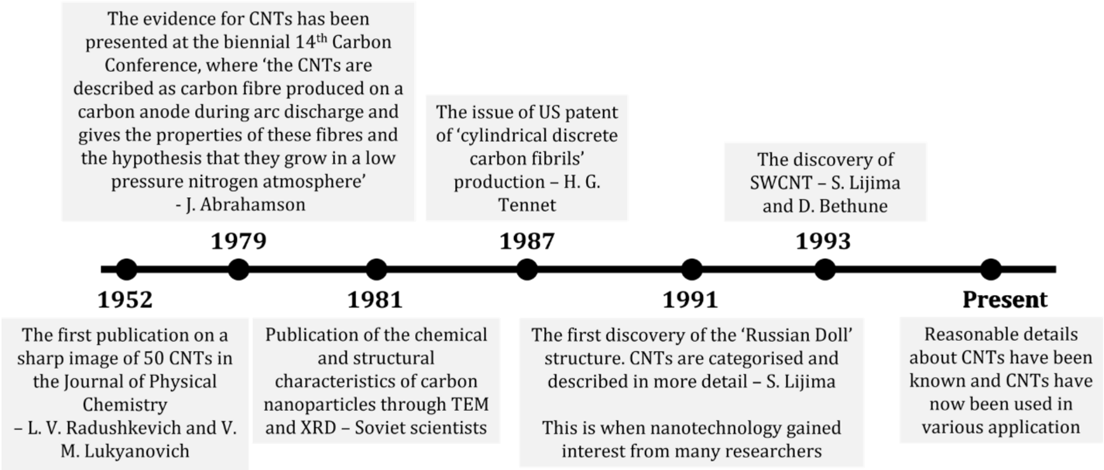

1952: The first publication on a sharp image of 50 CNTs in the Journal of Physical Chemistry – L. V. Radushkevich and V. M. Lukyanovich

1979: The evidence for CNTs has been presented at the biennial 14th Carbon Conference, where 'the CNTs are described as carbon fibre produced on a carbon anode during arc discharge and gives the properties of these fibres and the hypothesis that they grow in a low pressure nitrogen atmosphere' - J. Abrahamson

1981: Publication of the chemical and structural characteristics of carbon nanoparticles through TEM and XRD – Soviet scientists

1987: The issue of US patent of 'cylindrical discrete carbon fibrils' production – H. G. Tennet

1991: The first discovery of the 'Russian Doll' structure. CNTs are categorised and described in more detail – S. Lijima

This is when nanotechnology gained interest from many researchers

1993: The discovery of SWCNT – S. Lijima and D. Bethune

Present: Reasonable details about CNTs have been known and CNTs have now been used in various application

Figure 2.1: A timeline indicating various milestones in the discovery of CNTs [66]

CNTs are not only highly conductive to electricity, but they are also high in strength, flexibility, and chemical and physical stability [12,21,67]. CNTs may not contain any metallic bond but are still electrically conductive. The way CNTs conduct electricity is different from other conventional metal-based conductive materials. Due to the quantum mechanical rules called 'ballistic transport', the electrons travel within the CNTs without any interference from atoms that may create friction [68]. Therefore, with lower friction and high electrical conductivity, CNTs act as an alternative for conductive materials [12,21,67,69].

2.2.1 Types of CNTs

CNTs are nanomaterials composed of the rolled-up graphene sheet(s), forming cylindrical-structured molecules [70]. CNTs can be divided into two main types, SWCNTs and MWCNTs, as discussed briefly in *Chapter 1* (**figure 2.2**) [12].

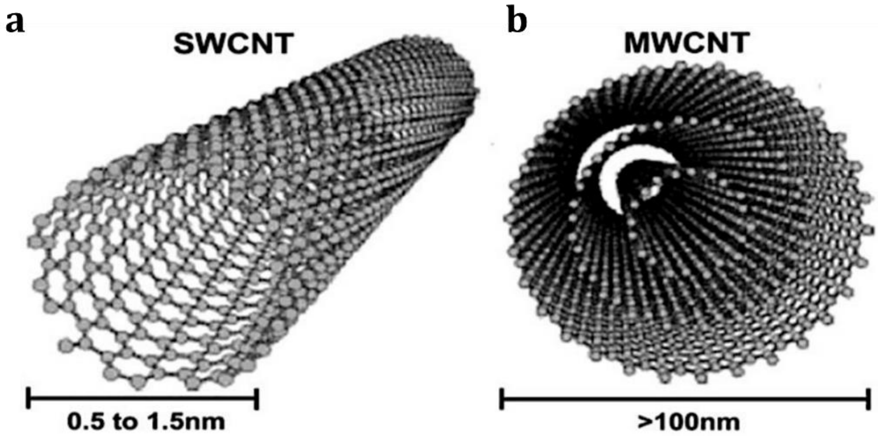

Figure 2.2: Structure of a) SWCNTs and b) MWCNTs (Russian Doll Model) [71]

SWCNTs and MWCNTs are among the strongest and stiffest conductive materials due to the sp^2 bonding formed between the carbon atoms within their structure [67]. These two types of CNTs are slightly different in certain aspects, as summarised in **Table 2.3** below [13].

Table 2.3: Differences between SWCNTs and MWCNTs [6,13,70,72,73]

SWCNTs	MWCNTs
One layer of the graphene sheet	Two or more layers of graphene
Requires catalyst for the synthesis	Do not require a catalyst for the synthesis
Difficult to synthesise bulk amount of CNTs as it requires special control	Easy to synthesise in bulk
High purity	Contain defects due to functionalisation and/or preparation process
Very flexible and very easy to twist	Lower flexibility due to more graphene layers
Simple structure	More complex structure
Likely to form more bundles	Less like to form bundles.
Higher production cost	Lower production cost

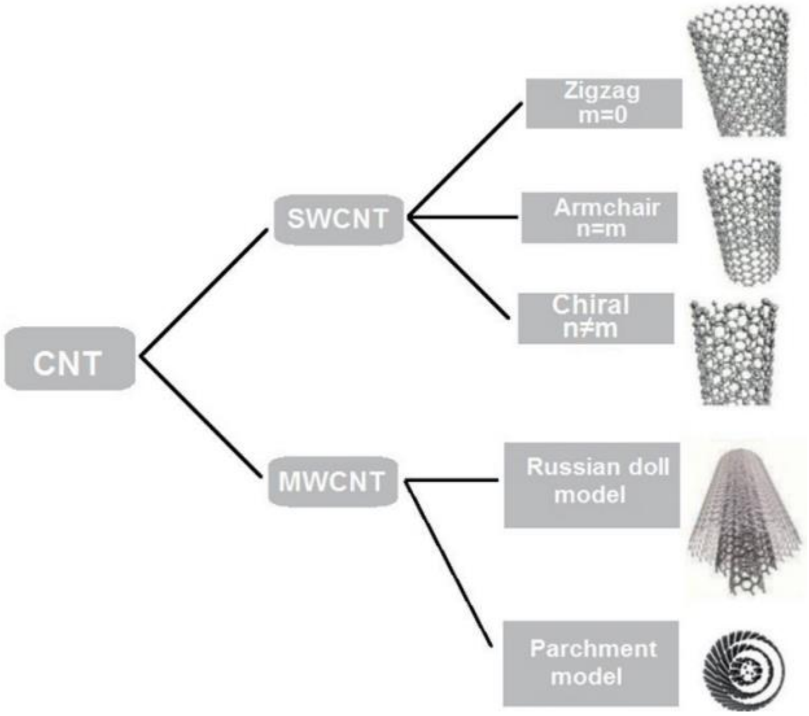

Figure 2.3: Types of CNTs [74]

2.2.1.1 Single-Walled Carbon Nanotubes

SWCNTs are a rolled-up graphene sheet with approximately 0.5 nm to 1.5 nm diameter and up to a few micrometres in length [71]. The diameter and length may vary depending on the preparation process for SWCNTs fabrication [12]. Generally, SWCNTs can be divided into three different forms: armchair, zig-zag, and chiral structures (**figure 2.3**) [75,76]. The chiral vector (c) of the rolled-up graphene sheet determines the structure of the CNTs, which strongly affects their bandgap, electrical conductivity and mechanical properties [66,75].

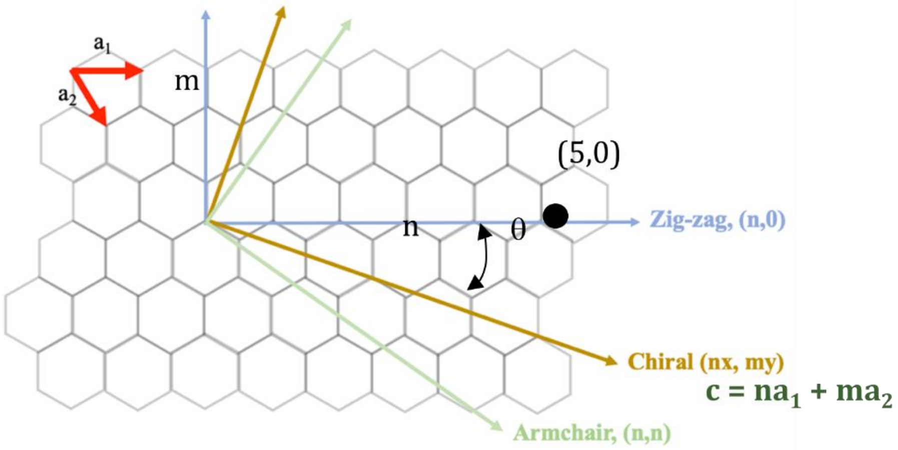

Figure 2.4: Chiral vector of SWCNTs [75]

$$c = na_1 + ma_2 \qquad \text{(Equation 1)}$$

c = chiral vector

n, m = chiral index

a_1, a_2 = primitive lattice vector

The chiral vector is the vector in the graphene lattice where two carbon rings connect, as defined in **Equation 1** [75]. The chiral index (n,m) is an integer similar to the x and y-axis, which describes the direction of the presented lattice and the chirality or twist of the CNTs. While the primitive lattice vector (a_1, a_2) represents a unit cell of the lattice structure [75]. a_1 is the vector nearest to the neighbour lattice point, which is lying along the 'zigzag' line, whereas a_2 is the vector at the lattice point closest to the a_1 axis (generally over the 'armchair' line) [77]. **Figure 2.4** illustrates the chiral vector that determines the structure of the CNTs, where,

- If the angle (Θ) is 0 °, the CNTs are called 'armchair'
- If the Θ is 30 °, the CNTs are called 'zig-zag'
- If the Θ is between 0 ° and 30 °, the CNTs are called 'chiral' [66,73]

It is challenging to control the formation of CNTs chirality; nevertheless, measurement and characterisation may be done to determine the difference in characteristics that may result from the chirality within the CNTs structure. For instance, depending on their chirality, SWCNTs could provide metallic or semiconducting properties. The SWCNTs exhibit metallic behaviour if n minus m is a multiple of 3, as in the case of armchair SWCNTs, while the rest would behave as a semiconducting material [13]. Due to the structure of rolling graphene, the electrons in the lattice structure are delocalised and reduce the charge flow. [75].

2.2.1.2 Multi-Walled Carbon Nanotubes

MWCNTs are similar to SWCNTs but are composed of multiple rolled-up graphene sheet(s) layers. However, unlike SWCNTs, MWCNTs tend to be larger in diameter, ranging from 2 to 100 nm on the outer layer [13]. There are two types of MWCNTs structure, Parchment and Russian doll model (**figure 2.3**) [73]. The parchment model is a single graphene sheet rolled up into multiple layers. The Russian doll model comprises two or more CNTs inside one another with several different diameters [78].

MWCNTs have gained lots of interest due to lower production costs and their ability to provide enhanced electrical and mechanical properties compared to SWCNTs [13,79]. Since MWCNTs contain multiple layers of graphene, it has high tensile strength and scope of introducing multiple functionalities/characteristics. Therefore, it prevents the destruction of the intrinsic structure during any chemical interaction from the surrounding environment [13]. Moreover, MWCNTs can obtain more combinations of graphene structures due to multiple layers of the graphene sheet. As a result, MWCNTs can provide different characteristics. Hence, MWCNTs may be used to fabricate sensors, transistors, and biological sensing labels in various applications [79,80].

2.2.2 Properties of CNTs

2.2.2.1 Mechanical Properties

CNTs have high elasticity and strength. The tensile strength of the CNTs can be up to approximately 100 -300 GPa [81]. Moreover, with the density of 1.3 g cm^{-3}, the specific strength of CNTs is as high as 48,000 kN m kg^{-1}, compared to high carbon steel, for example, with a specific strength of roughly 154 kN m kg^{-1}. CNTs can withstand high forces with a maximum extension before breakage of approximately 16 – 23 % of its original length [66].

2.2.2.2 Thermal Properties

CNTs can transmit a thermal conductivity as high as 6000 $Wm^{-1}K^{-1}$ at room temperature. CNTs can remain stable at temperatures up to approximately 750 °C and 2800 °C in air and vacuum, respectively [72]. In addition, the thermal expansion behaviour of CNTs is different from graphene sheets since CNTs are largely isotropic, while graphene sheet is anisotropic. Therefore, CNTs have a low thermal expansion coefficient for low-defects CNTs [72].

2.2.2.3 Chemical Properties

The cylindrical structure of CNT enhances their chemical properties. The curvature of CNTs allows hybridisation between π-orbital and σ-orbital to occur. Theoretically, since the CNTs diameter is proportional to the hybridisation rate, more orbital mismatch is introduced as the curvature increases; as a result, it enhances the chemical reactivity of CNTs [72]. Regarding their solubility, covalent side-wall functionalisation or end cap modification controls the solubility of CNTs in particular solvents [82]. It is difficult to covalently modify CNTs sidewalls as they consist of sp^2 bonding of carbon atoms. Thus, CNTs are classified as chemically inert materials [72].

2.2.2.4 Electrical Properties

CNTs are known for having high electrical conductivity. The electrons travel along CNTs graphene sheet layers freely in an axial direction without scattering [83,84]. The CNT's diameter plays a significant role in determining its resistivity. Thus, SWCNTs resistivity is lower than MWCNTs at approximately $1 \times 10^{-3} – 1 \times 10^{-4}$ Ω cm and $2 \times 10^{-3} – 1 \times 10^{-4}$ Ω cm, respectively [74], since the SWCNTs are smaller in diameter [13].

The density of CNTs is much lower than metals. For example, the density of SWCNTs and MWCNTs are 1.3 g cm^{-3} and 2.1 g cm^{-3}, while 8 g cm^{-3} for copper [81]. Therefore, CNTs would be suitable for many applications due to their high conductivity but low density [84]. However, if CNTs contain defects, there is an effect on their electrical performance due to the changes in electron flow [85].

2.2.3 Application of CNTs

2.2.3.1 Medical Applications

Since 2005, CNTs-based biomaterials have been used in medical applications for cancer treatment, regenerative medicine, and implant material [86]. Cancer treatment and diagnosis using CNTs biomaterials have been widely researched *in vito* for many years, but not until 2011, when two clinical trials on external CNTs devices for cancer diagnosis were investigated, *in vivo* [87,88]. According to Saito *et al.*, CNTs are now used as biomarkers and imaging, drug delivery systems (DDSs), and cancer treatment [86]. Currently, CNTs biomarkers have been reported to be used as a prostate cancer marker, colorectal cancer marker (CEA, CA19-9), and hepatocarcinoma marker [86]. Moreover, CNTs have been used as a highly sensitive contrast reagent for CT and MRI scans, for tumour and cancer cells [86,89,90].

CNTs are also reported to be used as regenerative medicine for bone and nerve tissue regeneration [86,91]. As reported by Cao *et al.*, grafted collagen-MWCNTs are used as a scaffold for muscle cell regeneration [92]. From 2002 to 2010, CNTs/polylactic acid has been reported to successfully enhances osteoblast and bone regeneration *in vivo* [86]. The experiment was carried out to regenerate the mouse back muscle; it is reported that bone formation using recombinant bone morphogenetic protein-2 (rhBMP-2) – MWCNTs regenerate faster than pure rhBMP-2 [93].

In artificial implants, materials like metal (e.g., stainless steel, titanium alloy and tantalum) and ceramic (e.g., zirconia ceramic) are used for bone and joint replacement [86]. However, these materials wear off over time and require revised surgery. In 2003, CNTs-based composite implants, such as MWCNTs conjugated with polyethylene, were developed to enhance the durability of the artificial implants [86]. *In vivo*, CNTs-based implants are used on mice; as a result, the implant binds with the bone without interfering with other internal bones or tissues, as reported by Pei *et al.* [94].

2.2.3.2 Electronic Applications

CNTs have high electrical and thermal conductivity, strength, flexibility, and stiffness. CNTs have metal-like electrical conductivity and high thermal conductivity [95]. With their unique properties, CNTs may be applied in a wide range of electronic applications such as energy storage, molecular electronics, and electrical emitters [96].

CNTs may be applied as electrodes in batteries and capacitors due to their large surface area, high electrical conductivity, and linear geometry. Compared to other carbon-based electrodes, CNTs-based electrodes have the highest reversible capacity for lithium-ion batteries [97]. Therefore, CNTs work as supercapacitors, current collectors, and gas diffusion layer [96].

CNTs also act as an electrode catalyst support in PEM fuel cells to enhance their performance. Since fuel cells require high durability, CNTs can deliver this objective due to their toughness [98]. Furthermore, CNTs are an ideal component for electronic circuit construction in connecting molecular electronics [99,100].

Due to CNT's size and properties, CNTs are well-known as electron emitters [96]. With the ability to construct an extremely small tip for the electron emitter, a more concentrated electric field can be created alongside the improvement in field emission. CNTs are appropriate for building low power devices with high current density and stability [101]. Therefore, CNTs are used in field emission flat panel displays where multiple electron guns can be installed for each display pixel [102,103]. With these characteristics, CNTs act as lightning arrestors and electron microscope sources [103].

2.2.3.3 Environmental Applications

CNTs show a promising outcome in environmental monitoring and wastewater filtration. Environmental issues such as air and water pollution are the most worrying harm to the environment and human beings [104]. Therefore, researchers have developed CNTs-based air and water filtration devices to remove bacteria and filter microscopic particles [103].

CNTs may be used to fabricate CNTs-based gas sensing devices for nitric oxide (NO), nitrogen dioxide (NO_2), ammonia (NH_3), and sulfur dioxide (SO_2) [105]. However, they are low in selectivity; therefore, CNTs are functionalised with metal oxides to improve their selectivity and sensitivity towards target species, with a faster responding time than pure CNTs-based gas sensor devices [104]. Furthermore, some gases have no colour, taste, or smell, which increases the difficulty of monitoring and treating them. Nevertheless, CNTs efficiently detect and remove gases as they are composed of a large active surface area leading to high adsorption and selectivity. Hence, many researchers are focusing on developing CNTs-based sensors and wastewater treatment devices [104].

CNTs also act as an absorbent to remove dyes and toxic chemicals [106]. For instance, many industries use dyes in their manufacturing process, leading to a high possibility of water pollution, which may harm human health. Therefore, the functionalisation of CNTs with chitosan hydrogel beads has been investigated for dye removal. The presence of amino and hydroxyl groups on chitosan helps CNTs remove dyes [107].

CNTs may be applied as heavy metal detection devices. Heavy metals in water are the most harmful contaminants to the environment and could be lethally harmful to humans. Therefore, CNTs have been used to absorb heavy metal ions such as copper (Cu^{2+}), nickel (Ni^{2+}), lead (Pb^{2+}), and zinc (Zn^{2+}). The oxidation of CNTs in acid solution improves the absorption capacity toward target heavy metal ions [104]. Sidewall functionalisation increases the interaction between the CNTs and the heavy metal ions [108].

Finally, CNTs may act as pesticide monitoring sensor devices. In agricultural practices, pesticides contain a toxic chemical that is hazardous to the environment. The research incorporated CNTs into a biosensor where CNTs act as a catalyst to create a signal for pesticide detection with high sensitivity [104]. Furthermore, CNTs may be used for solid-phase extraction as absorbents. The CNTs absorbent provides rapid and simultaneous electrochemical detection and extraction for pesticides [109].

2.2.4 CNTs for Biosensor Fabrication (Relationship between Connectivity and Electrical Conductivity)

In CNTs electrode sensor fabrication, it is essential to understand the relationship between the CNTs connectivity and the associated electrical conductivity. The connectivity between CNTs creates an electron pathway for current to flow, which determines the conductivity of a fabricated electrode [89]. In ink deposition, the CNTs ink ejects onto a substrate with random orientations, where the solvent evaporates and leaves the CNTs behind on the substrate surface in random orientations [110]. The CNTs that are in contact with other CNTs provide electron pathways for the current to flow and make the electrode usefully conductive. On the other hand, those CNTs that are completely isolated are less likely to facilitate any current flow in a sensing system [89].

Accordingly, the two major factors that may affect the CNT’s electrical conductivity are the CNTs concentration and length. Firstly, highly concentrated CNTs are more likely to be in contact with each other, which increases the current connectivity and enhances the material’s conductivity. Secondly, longer length CNTs are more likely to initiate inter-CNTs connectivity and conductivity than shorter CNTs [110]. CNTs Ink Formulation

CNTs are a challenging material as they are difficult to disperse in an aqueous solution due to their hydrophobic nature [67]. In an aqueous solution, CNTs agglomerate and form bundles due to the Van der Waal forces and p-p interactions [18,111]. According to previous research, Van der Waal forces depend on the radius of the CNTs, especially when the radius is lower than 7 nm. As a result, this could lead to printhead clogging when fabricating CNTs-based devices by inkjet printing, which is undesirable for ink deposition. Therefore, an appropriate solvent and modification process needs to be selected. According to previous research, CNTs ink is formulated through three main techniques: side-wall functionalisation/modification, organic solvent dispersion, and aqueous dispersion [19].

2.2.5 Sidewall Functionalization of the CNTs

The sidewall functionalisation technique is commonly used to disperse CNTs into an aqueous solution by adding CNTs into an acid mixture, allowing the oxidation process to occur and functionalise the CNTs sidewall with an appropriate functional group [82]. The most common acids used in this process are concentrated nitric acid [112], a mixture of nitric acid and sulfuric acid [113] or a mixture of sulfuric acid and hydrogen peroxide [114].

For instance, functionalising CNTs sidewall with a mixture of nitric acid and sulfuric acid consisted of three major steps:

1. free carbon atoms formation (initially from CNTs sidewall defects and from CNTs dispersion in acid mixture),
2. free carbon atoms saturation, and
3. sidewall functionalisation [115,116].

As a result, the functionalised CNTs may be dispersed in an aqueous solution (such as water).

Even though sidewall functionalisation using an acid mixture enhances the dispersibility of CNTs. This method may cause defects and break down the CNTs into shorter lengths [21]. This means that the length of the obtained CNTs may be unpredictable and vary in size. As a result, it may not be appropriate for applications where accuracy and precision are necessary. Nevertheless, for electrode fabrication by inkjet printing, shortened CNTs may improve the ink deposition by preventing nozzle clogging [19].

2.2.6 Dispersion of CNTs in Organic Solvent

In the organic solvent dispersion technique, CNTs do not require any modification or functionalisation. Instead, the organic solvent separates CNTs bundles and homogenises CNTs into the solvent [117]. Various hydrophobic organic solvents attract the CNTs sidewall, which is also hydrophobic. As a result, the organic solvent molecules on the surface of the CNTs repel and break the Van der Waal forces between the CNTs, which allow the CNTs to spread apart [110]. Dichloromethane and hexane, for example, may be used to disperse CNTs [117]. While in some cases, commercially available polymers, ranging from polyvinyl chloride (PVC), and polystyrene (PS) to poly(vinyl pyrrolidone) (PVP), may be used to enhance the dispersion of the CNTs in the organic solvent by acting as a dispersant[80].

An organic solvent-based CNTs ink is suitable on non-porous substrates, including glass, PVC, and ceramic substrates, since the organic solvent evaporates rapidly [110]. However, due to the organic solvent evaporation behaviour, there is a higher chance of the ink drying out and blocking the printhead. Therefore, it is important to completely seal the inkjet cartridge to avoid any evaporation of the solvent [110]. However, hydrophobic solvents may cause concerns on both health and environmental issues [118,119].

2.2.7 Dispersion of CNTs in Aqueous solvent

Dispersing CNTs in water is challenging due to the CNTs' hydrophobicity and associated Van der Waal forces [120]. A surfactant, an amphiphilic compound comprising a hydrophilic head and hydrophobic chain, is introduced to disperse CNTs in an aqueous solution [110,121]. The hydrophobic part of the surfactant attracts and adsorbs onto the CNTs sidewall that is also hydrophobic, leaving the hydrophilic head facing the aqueous solvent [122]. As a result, it reduces Van der Waal forces between CNTs and repels CNTs apart [110]. Several surfactants have been used in CNTs dispersion, such as SDS and SDBS [123]. The challenges of using surfactants are identifying the most appropriate surfactant for CNTs dispersion and dispersion techniques [124].

2.3 Overview of Inkjet Printing Deposition Techniques

2.3.1 Commercial Inkjet Printer

The commercial inkjet printer is user-friendly, cost-effective, high speed, precise, and highly available in the market; therefore, it has been applied in many fields, including the electrochemical research field [23]. Thus, inkjet printers could significantly reduce the production cost, especially for mass production [24].

A commercial inkjet printer (also known as a home-office inkjet printer) comes with different features and printing technologies depending on the desired purposes. Inkjet printers are differentiated into two major categories: continuous and drop-on-demand (DOD) inkjet printers. The most common printing technologies used among well-known brands are thermal inkjet printers and piezoelectric inkjet printers [25]. These inkjet printers can be modified and used to print any desired materials. However, since each printing technology operates distinctively, it tends to have different pros and cons that affect the printing performance.

Although continuous inkjet printers are fast, suitable for industrial applications, and prevent nozzle clogging, they have a higher initial cost than DOD inkjet printers. In addition, due to ink restriction, a continuous inkjet printer is not the most suitable printing technique for electrode printing [25].

2.3.1.1 DOD Inkjet Printer

DOD inkjet printers only eject ink when required; therefore, ink droplet deposition is more controllable than a continuous inkjet printer [125]. This technology does not require any droplet charging, deflection, or recycling system. Depending on the nozzle size, the ink droplets can be as small as 15 μm in diameter (150 to 200 pL), giving a higher image resolution than the continuous inkjet printer [25]. Several techniques are available to create pressure for ink deposition: acoustic, valve, electro-hydrodynamic, thermal, piezoelectric, and electrostatic ejection methods [24]. Nevertheless, thermal and piezoelectric inkjet printing is the most common technique, while other methods are still developing [25].

2.3.1.1.1 Thermal Inkjet Printing Technology

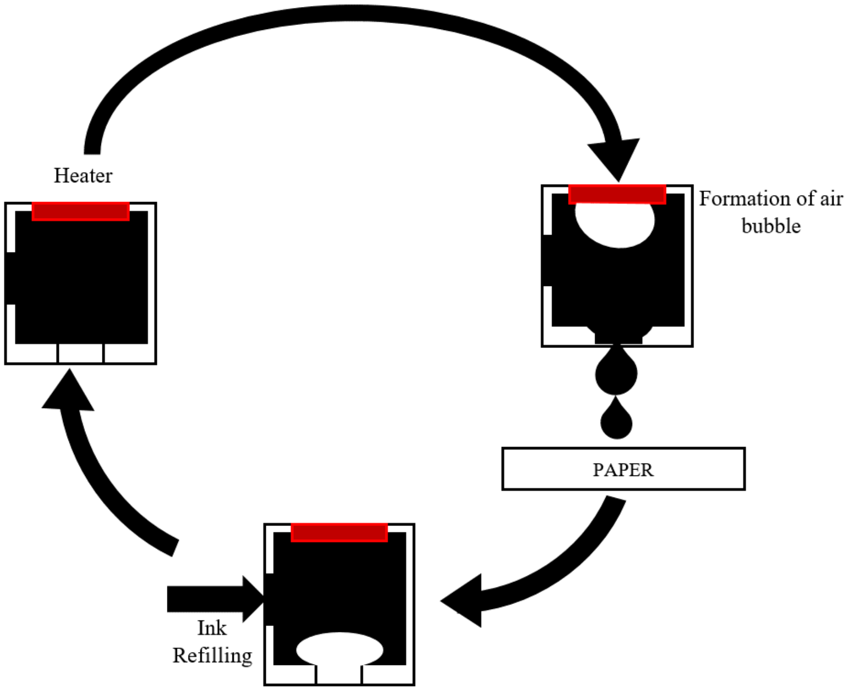

Figure 2.5: DOD thermal inkjet printing technology.

The thermal inkjet printer is low-cost, simple, high quality, and appropriate for various substrates [25]. In the ink deposition process, the printer uses electricity to electrify the resistor in the nozzle head to heat the ink. This creates rapid ink bubble expansion, pushing the ink through the nozzle head onto a substrate in a few microseconds (**figure 2.5**) [25,126]. However, since the printer requires a high temperature of up to 400°C, it may not be suitable for a specific type of ink. Furthermore, although the heating process is only for a few microseconds, some inks could degrade once exposed to high temperatures. Therefore, there is a limited number of ink options [25,126]. In ink droplets, the droplet size is approximately 50 pL larger than the ink droplet from the piezoelectric inkjet printer and with fewer varieties [25].

2.3.1.1.2 Piezoelectric Inkjet Printing Technology

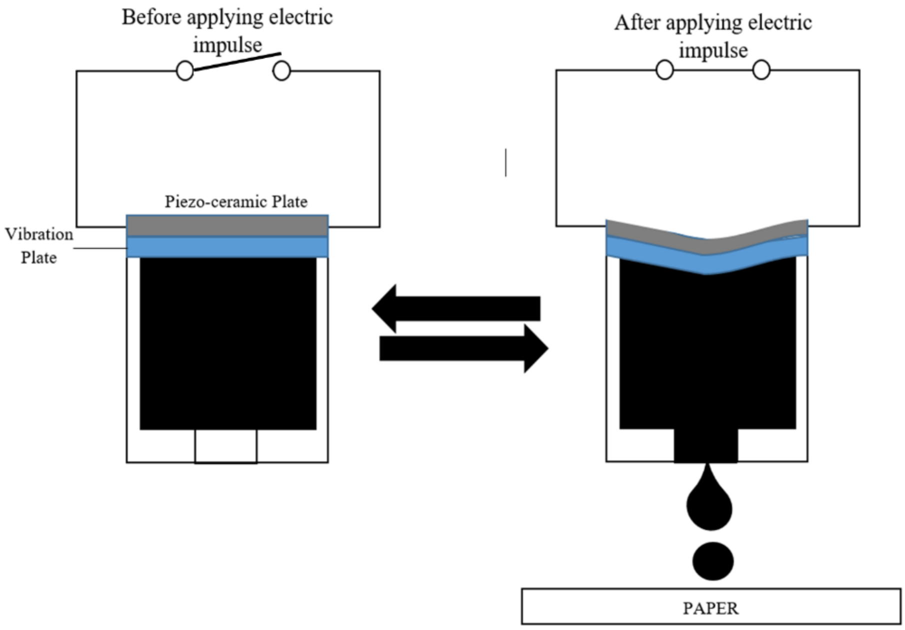

Figure 2.6: DOD piezoelectric inkjet printing technology.

The piezoelectric inkjet printer consisted of materials such as piezoelectric crystals or ceramics at the nozzle head. Once the electrical signal is applied to the microscopic piezoelectric material, the element bends and moves the vibration plate, allowing ink deposition to occur mechanically without heat [126]. In addition, the vibration plate or the diaphragm prevents any unwanted interaction between the ink and the piezoelectric elements **(figure 2.6)** [101]. Alternatively, if no impulse is applied, the piezoelectric material will remain in its initial position to prevent the ink from flowing through the printer nozzle [25].

The ejecting methods include squeeze, bend, shear, and push inkjet printing (**figure 2.7**) [25]. Firstly, the squeeze method involves a contraction of the piezoelectric elements once the electrical impulse is applied. As a result, the piezoelectric elements bend and squeeze the ink through the printer nozzle onto the paper [25]. Secondly, the bending technique involves bending the piezoelectric elements and the vibration plate (also known as the diaphragm) to eject the ink through the nozzle head [25,127]. Thirdly, shear inkjet printing may operate where more than one inkjet channel is present in the system. Once the electrical signal is applied, the upper half shear is followed by the lower half; as a result, the inner volume decreases and pushes out the ink through the printing nozzle [25,128]. The wall returns to its original shape by removing the electrical signal as all the printing systems do. Finally, the push mode deposits the ink by bending the piezoelectric element and the diaphragm as in the bending method [25,128].

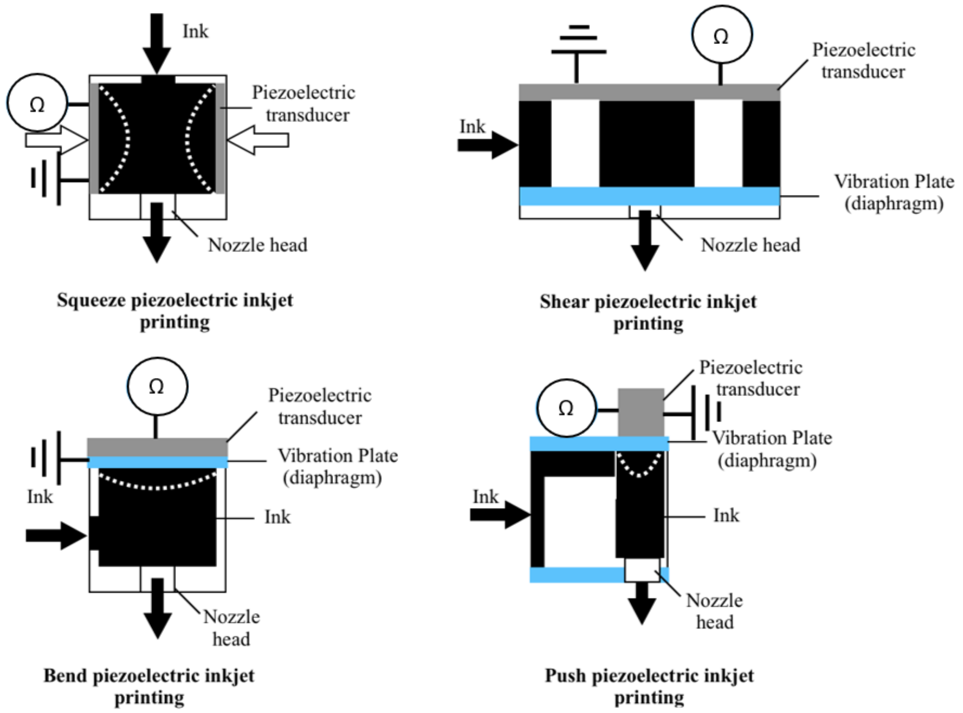

Figure 2.7: Different types of piezoelectric inkjet printing techniques

A piezoelectric inkjet printer differs from a thermal inkjet printer since no heating is involved in the printing process; therefore, more ink varieties are applicable. The printer could run for a more extended period. As a result, the ink droplet is more spherical and has more controllable droplet volumes that can go down to 1.5 pL [25]. As the volume of the ink droplet changes, the qualities and details of the printed image change. This is because smaller ink droplets produce finer images than larger droplets. Since no bubbles are created, ink deposition is more accurate [25]. However, good quality imaging comes with a price where a more expensive high-density nozzle head increases the production cost [119].

In conclusion, the inkjet printer is a useful alternative tool for developing technology through material deposition; it is suitable for paper-based device fabrication due to its simplicity, high resolution and accuracy, reasonable thickness control, and relatively low cost.

2.4 Paper-based CNTs Electrode Sensor Devices

2.4.1 State of the Art: Paper Substrates

Paper substrates are used in many research fields, including microfluidic devices and sensors, analytical chemistry, food industries, and environmental and medical applications [125,129]. Paper substrates are low-cost, thin, lightweight, flexible, compatible with various chemicals, and biodegradable [15,20]. Paper is composed of mainly cellulose but can provide different properties and characteristics according to its porosity, thickness, and flow rate, as summarised briefly in **Table 2.4**.

Table 2.4: Types and properties of the paper substrate

Type of Paper	Material	Properties	Ref.
Whatman Grade 1	Cellulose	Porosity: 11 µm, Thickness: 108 µm, Weight: 87 g m^{-2}	15
Whatman Grade 3	Cellulose	Porosity: 11 µm, Thickness: 390 µm, Weight: 97 g m^{-2}	15
Whatman Grade 4	Cellulose	Porosity: 20-25 µm, Thickness: 210 µm, Weight: 92 g m^{-2}	15
Glossy Paper	Inorganic filler blended cellulose	Porosity: 0.02-0.04 µm	130,131
180 gm office paper	Cellulose	Thickness: 190 µm	129

Since each type of paper substrate offers different properties and characteristics, several factors could affect their penetration behaviour:

- *Material:* Some paper substrate is composed of blended cellulose or material coating on top; therefore, the penetration rate of the solvent may vary according to the primary material of the substrate.
- *Porosity*: The paper substrate with a larger pore size is more likely to be penetrated faster than a smaller porosity substrate [15]. For example, the solvent is likely to penetrate Whatman filter paper grade 4 faster than Whatman filter paper grade 1 since its porosity is approximately 10-15 µm larger [15].

- *Thickness*: The substrate thickness significantly affects the stability and durability of the material. This is because thinner paper substrates can hold a lower volume of solvent, which is unsuitable for applications requiring a larger sample volume or longer detection time.

Therefore, it is essential to choose the paper substrate accordingly for inkjet printing with CNTs.

2.4.2 Paper-based Device Application

Figure 2.8 shows the summary of inkjet-printed paper-based devices application. Paper-based devices are widely used throughout the medical field as they are low-cost, user-friendly, and simple for clinical usage. One of the most recent paper-based devices application is a lateral flow SARS-CoV-2 antigen detection device. This paper-based device was widely used during the Covid-19 pandemic in the past two years [132,133]. Moreover, a paper-based device can detect specific substances in the urine, saliva, and blood. In urine, glucose, uric acid, lactate, nitrate, ketone, nucleic acid, ascorbic acid, protein, and other analytes can be detected and measured using paper-based devices [15,16]. At the same time, blood group, glucose level, diabetes markers, and glycated haemoglobin are identified from a blood sample [15].

Paper-based may also be used as an environmental monitoring system and food and safety monitoring devices. A paper-based device supports electrochemical sensors to detect heavy metals and toxic chemicals in contaminated areas [15]. For example, paper-based devices determine the concentration of the contaminant, optically and analytically. These include Cr(VI) Cu, Cd, Zn, Ag, Pb, Ni, and Hg. [17]. While in food safety and food and beverage monitoring device, the paper-based colourimetric sensor devices change colour if there is any deterioration within the product (biologically, chemically, or physically) [15,134]. Besides, due to the rules and regulations related to alcohol and quality control, paper-based devices may be used to measure alcohol level, carbohydrates and ethanol in beer [15].

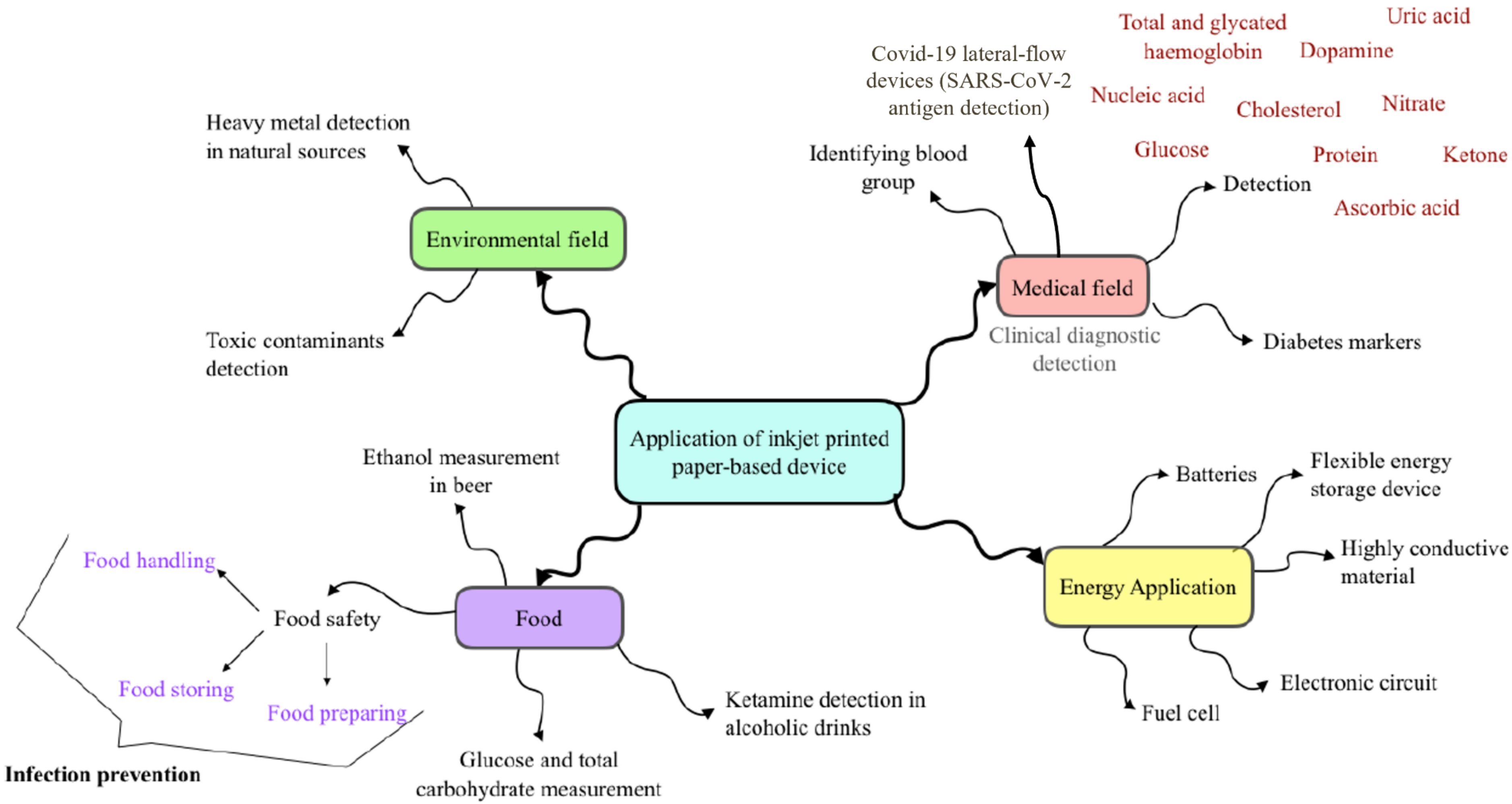

Figure 2.8: Application of paper-based sensing devices [15–17,132–134]

2.4.3 Components of Electrochemical Sensor

An electrochemical sensor usually consists of three electrodes which are the working electrode (WE), reference electrode (RE) and counter electrode (CE) [135]. These three electrodes have their role that helps each other to enhance the performance of the overall sensing device.

- WE: the main component of the electrochemical sensor. Therefore, the reaction of interest occurs on the WE, and the target analyte is detected in this area. The electron transfer takes place in a controlled process at the WE [135].

- RE: the standard electrode to compare the potential changes with the WE. Thus, the potential at the RE should be highly stable and should not fluctuate during the reaction since it can affect the detection performance [136]. Ideally, the current flow towards the RE is zero, and the CE is used to balance the current flow and keep the RE stable at virtual zero current [137].

- CE: Also known as an auxiliary electrode, it balances out the electrochemical reaction at the WE and closes the current circuit [138]. It prevents the current from flowing between the WE and the RE by allowing the current created to leave through the CE [139]. Although the CE is not involved in the reaction, it enhances the detection efficiency by preventing the current flow in the RE [140]. Commonly, the CE is made of platinum, iron, or graphite and usually has a larger surface area than the WE to prevent any current limitation that could slow down the electron transfer reaction on the WE [137].

2.4.4 Electrochemical Sensor Electrode Design

In electrode designs, electrode size and shape vary according to the application. Nevertheless, it comes with a similar concept. As reported by Kit-Anan and co-workers, the optimal electrode area ratio is 1:1:4 (WE: RE: CE), with the smallest gap possible between the WE and the RE. This is to do with the uncompensated resistance within the potentiostat circuit, which is usually not too significant if the sensing current is low (e.g., μA ranges) [139]. Nevertheless, the electrode area also influences the detection speed, mass transport, and current flow of the electrochemical system [141]. Therefore, the electrode size should be fabricated according to the sample volume to enhance the sensor's effectiveness.

The electrode designs may be fabricated according to the user's ideas and imagination. Although the design is changeable, the surface area ratio remains fixed to optimise the detection performance of the electrochemical sensor. For instance, in Nie's research group, the electrodes are designed to have a long rectangular shape in which the area of the RE is slightly smaller than the WE and the CE by 1.5 mm^2 [142]. This shape is very simple and easy to construct with no complicated shape or design. Other research groups also use the design but with different surface areas [139]. Despite the difference in the electrode designs, these electrodes share a similar area ratio [23,143].

2.4.5 Types of Electrochemical Sensor

There are three major electrochemical sensors which are potentiometric, conductometric, and amperometric electrochemical sensors [140].

2.4.5.1 Potentiometric Sensors

Potentiometric sensors have been commonly used for centuries as they are easy, simple, and low-cost. This method consisted of three major types: ion-selective electrodes, ion-selective field-effect transistors (ISFET), and coated wire electrodes [140]. The potentiometric sensor measures the potential difference between the RE and the WE. The potential difference appears when the potential at the WE or membrane changes with the environment while the RE remains fixed [135]. There is no counter electrode, as potentiometric measurements are at as close to zero current as possible.

2.4.5.2 Conductometric Sensors

A conductometric sensor is a simple and low-cost electrochemical sensor where a CE is not required. The sensor measures the changes in conductivity at different frequencies. The changes in conductivity may be used to quantify the concentration of analytes present in the sample solution [135]. Although a conductometric sensor is user friendly, it is non-selective [140]. Therefore, modifying the electrode surface enhances the selectivity, creating a simple and rapid conductometric sensor with high selectivity [140].

2.4.5.3 Amperometric Sensors

The amperometric sensor measures the current created from the oxidation or reduction reaction on the WE by applying a constant potential to the system [140]. There are two major types of amperometric sensors: a simple process where two electrodes immerse into the electrolytes at a controlled potential and complex instrumentation containing three electrodes where a RE is introduced into the system. The detection efficiency of the amperometric sensor is mainly affected by the material of the WE; therefore, it is important to choose an appropriate conductive material selectively [140].

2.5 Plasma Polymerization (PP)

2.5.1 Plasma

Plasmas are the fourth state of matter after solid, liquid and gas [144]. Plasma is quasi-neutral gas which consists of photons, metastable particles, radicals, ions, neutral, and electron species [145–148]. It can be found in the natural environment (e.g. lightning, stars, flames, and aurora) and can also be generated artificially using electron beams, laser, nuclear fusion, flames, or electrical discharge [145,149]. Electrical discharge or glow discharge is one of the most common approaches for plasma generation in which the plasma generated is referred to as 'non-equilibrium' or 'cold' plasma [148].

Generally, plasmas can be divided into two major types, thermal (equilibrium) and non-thermal (non-equilibrium) plasma, according to the temperature of the electrons, ions and neutral [150]. In thermal plasma, the temperature of the atoms and the heavy particles in plasma is the same [149,150]. In contrast, non-thermal plasma refers to a plasma with an electron temperature higher than the heavy particles (neutral particles and ions) at room temperature [150,151]. Further details on non-thermal plasma will be explained in *section 2.5.2.*

One of the outstanding features of plasma is that they are electrically conductive [152]. Plasma is electrically neutral since the number of positive and negative charges is similar, while the number of neutral molecules may vary [149,152]. **Figure 2.9** illustrates the overview of different types of plasma according to the relation between the temperature and electron density.

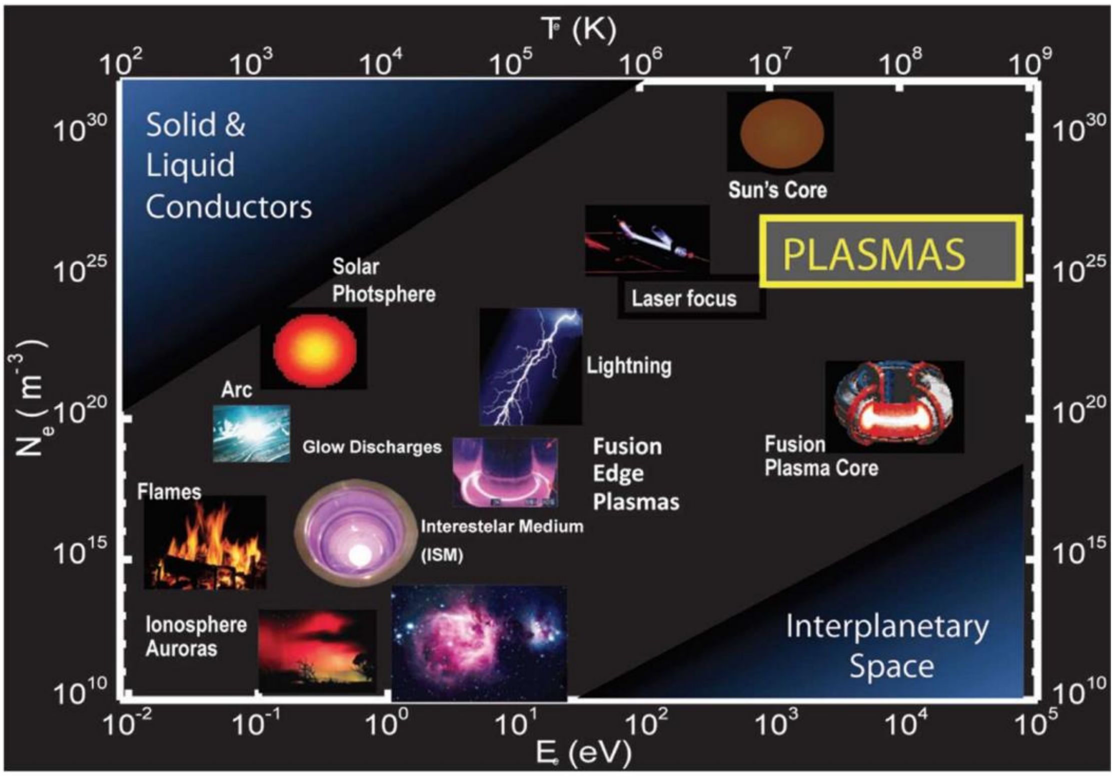

Figure 2.9: Types of plasma in relation to electron density (N_e), energy (E), and temperature (K) [152]

2.5.2 Cold Plasma (Non-Thermal/Equilibrium Plasma)

Cold plasma or non-equilibrium plasmas are the plasma generated in which the heavy particles (including ions) have different kinetic energy or temperature from the electrons [148]. In PP through electrical discharge from applied electrical power, the energy is received only by the electrons; therefore, the temperature or the kinetic energy of the electrons is much higher than that of the heavy particles, and the neutral atoms are at room temperature. The production of cold plasma can be ignited through electrical energy, which can be carried out under atmospheric or reduced pressure at room temperature [148].

The advantages of using cold plasma are the ability to modify and control the surface properties without interfering with the bulk properties of the solid materials [153]. Moreover, this prevents any thermal damage that may occur on the substrates due to the low temperature of heavy particles [148].

The properties that the cold plasma may alter include surface wettability, adhesion, energy, chemistry and topography, for example [149,154,155]. Therefore, cold plasmas are commonly used in biomedicine (e.g. wound healing and dental canal disinfection) [150], food industries (e.g. inactivate contamination of microbes in food) [156,157], and environmental sciences (e.g. wastewater treatment) [158].

2.5.3 Formation of Polymer in Plasma

PP is a technique to form polymeric materials using plasma state monomers or reactive species created in the plasma state [146]. PP is a one-step process where a thin film of material deposits onto the surface of the substrate [153]. The coating of plasma polymer provides the material's surface modification where the functional group retention can be controlled by adjusting the PP extrinsic parameters. These parameters include power, time, flow rate, and pressure [149,159]. Further details will be discussed in *section 2.5.5.*

PP occurs through ionisation of organic monomer gas at high-frequency electrical discharge [160]. For example, glow discharge uses an electrical field to provide energy to free electrons, and the collision between free electrons and neutral molecules reduces that energy. The energy transfer towards gas molecules creates chemically reactive species and becomes precursors for PP [145,147].

2.5.3.1 Stages of Plasma Polymerisation

PP consisted of three main stages:

- The initiation (ignition) process: Free radicals and atoms formation. The formation occurs through the collision of electrons and ions with the gas monomers [160].
- The generation process: Polymeric chains formation [160]

- The termination process: Polymer chains terminate, the plasma polymers generated form 3D complex networks on the substrate surface, with high cross-linking and branching. With such a structure, the plasma polymers are mechanically and chemically stable [28,149,153,161].

2.5.3.2 Different Types of Monomers Used in Plasma Polymerisation

In PP, monomers with different functional groups have been investigated to modify the substrate surface through functionalisation. These functionalities include primary amine (-NH2), hydroxyl (-OH), and carboxyl (-COOH) [162]. In this research, PP of amine-based and carboxyl-based monomers will be discussed.

PP of amine-based monomers is an efficient approach to modifying the chemical functionality and properties (e.g. wettability, adhesion and topography) of the substrate surface with nitrogen-containing functional group [155,163]. Amine groups ($-NH_2$) are known for their positive charges, which attract negatively charges molecules. PP of amine-based monomers have been widely used to introduce amine-rich coating to the substrate surface [155,162]. . This includes allylamine [164–166], ethylenediamine [167], heptylamine [168,169], propylamine[170], for example.

PP of monomers containing carboxyl groups (e.g. acrylic acid [171,172], acetic acid [173], and maleic anhydride[172]) provide a carboxyl-rich coating on the substrate surface. Acrylic acid is one of the most widely used carboxyl-based monomers for PP at atmospheric pressure [171,174,175]. This carboxyl-rich coating enhances the surface wettability, adhesion, retention and surface reaction [172].

2.5.4 PP Apparatus

There are different designs for plasma polymerisation reactor, but they share common features, including an enclosed chamber, a pumping mechanism to lower pressure for low-pressure systems, a technique of adding monomer(s), and a method of igniting and maintaining the plasma [159].

In the case of plasma polymerising functionalised coatings, the system is set to vacuum pressure (from 1×10^{-2} mbar to 1 mbar) in order to ignite the plasma at an appropriate input power [159]. Liquid nitrogen and a vacuum pump are used to create vacuum conditions inside the glass barrel for PP [160]. While the excitation can be provided using different techniques such as DC, RF, microwave, as well as continuous wave or pulsed. Depending on the PP reactor designs, the electrodes may be connected internally or externally to the chamber and coupled directly or indirectly to the power source [159]. **Figure 2.10** illustrates a schematic diagram of a PP reactor. This illustrates typical glass-barrelled reactor and is a stylised representation of the system used in this PhD research project. (Refer to *Chapter 5* for more details on the PP reactor used in this research project)

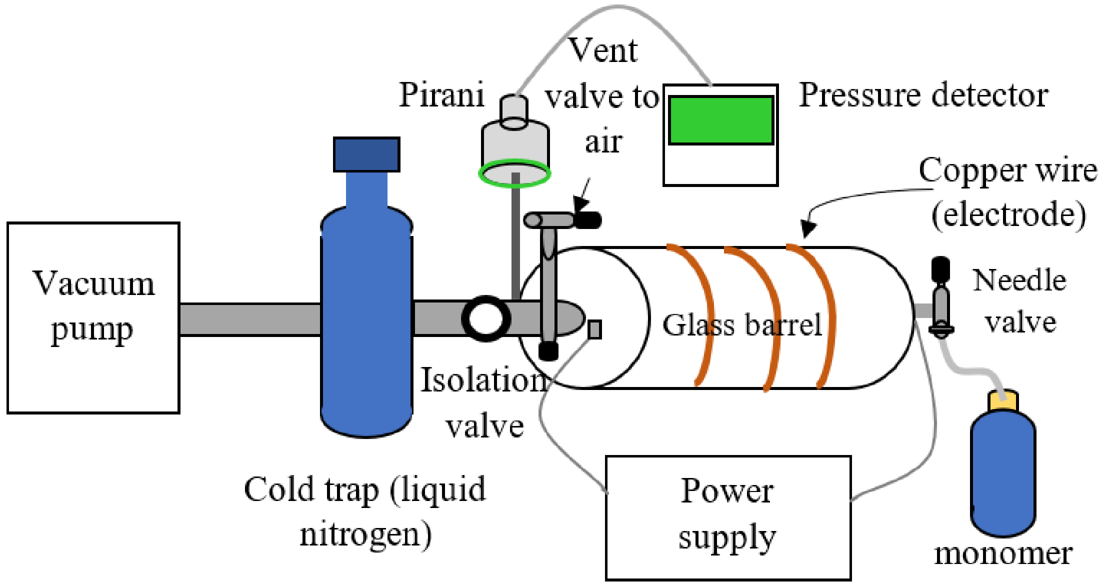

Figure 2.10: Schematic diagram of the PP reactor used in this PhD research [160]

2.5.5 Factors Affecting PP

PP can alter the surface chemistry and the properties of the substrate without interfering with the bulk properties of the substrate or being affected by the chemical reactivity or the substrate structure [28,176,177]. Varieties of functional group compounds can be coated onto the substrate at high concentration and stability, depending on the type of gas used [153,177,178]. However, many factors may affect the plasma chemical and physical properties and deposition efficiency [179]. The possible factors are:

- *Power/flow rate ratio*: High power /flow rate ratio may lead to an increase in the amount of chemical functionality retained by the deposit [144,177]

- *Power*: High power may lead to an increase in ionisation degree and plasma potential [144]

- *Flow rate*: High flow rate may lead to high system pressure, which increases the density of uncharged molecules within the system [144]

- *Pressure:* Vacuum condition is required to undergo PP. If the pressure fluctuates or exceeds the required condition for each plasma polymer, it may cause external contamination [176,177]. Additionally, the pressure also affects the functional groups retention and the plasma deposition rate of the PP process [159,180].

2.6 Surface Analysis and Characterisation

2.6.1 X-Ray Photoelectron Spectroscopy (XPS)

X-ray photoelectron spectroscopy, also known as electron spectroscopy for chemical analysis (ESCA), is a surface-sensitive analytic technique to study the sample's surface chemistry, including elemental composition, empirical formula, chemical state, and electronic state of the element [176,181,182]. It is widely used to characterise polymeric materials, qualitatively and quantitatively, potentially identifying the functional groups on the sample surface [183]. These functional groups may have resulted from the synthesis process or polymer processing by PP surface modification or other approaches (e.g. additive) [183].

The benefits of using this surface analysis are high surface sensitivity and the ability to identify the chemical state of the elements presented on the sample surface [182]. Almost all elements and surface composition can be detected by this technique, quantitatively, apart from helium and hydrogen [184]. Therefore, the XPS can be used to investigate and identify most materials.

Since every interaction between materials occurs on the material surface, the surface properties and chemical composition of the material significantly determine the material's wettability, adhesion, and charge transfer, for example [182]. Hence, it is essential to investigate and study the surface chemistry of the materials.

2.6.1.1 Principles

2.6.1.1.1 Photoelectron Generation

In XPS characterisation, soft x-ray beams are irradiated on a material surface in which the electrons in the sample absorb photons at a certain energy level, leading to photoelectron emission from the top 1 to 10 nm surface [176,182,184] (**figure 2.11**). These electrons escape the material surface without any energy loss and are therefore diagnostic of the element from which they originate. Electrons that lose energy (e.g through inelastic collisions) contribute to the background the photoelectron peak sits. The number of emitted electrons is counted over the electron's kinetic energy using an electron analyser/detector to generate a photoelectron spectrum [181]. **Figure 2.12** shows a schematic diagram of XPS.

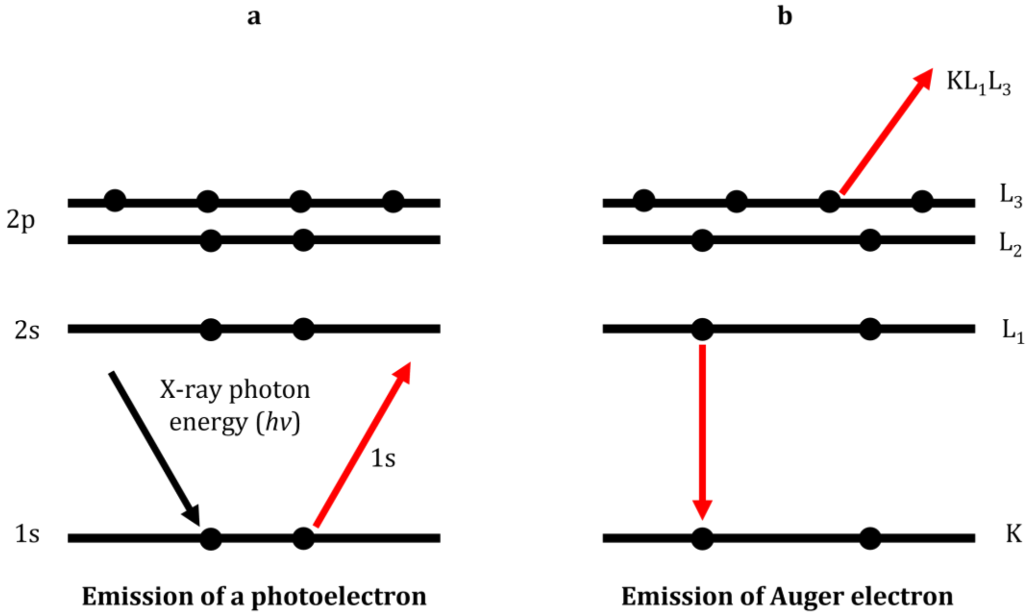

Figure 2.11: Photoelectron generation process by x-ray irradiation, emission of a) photoelectron and b) Auger electrons [185]

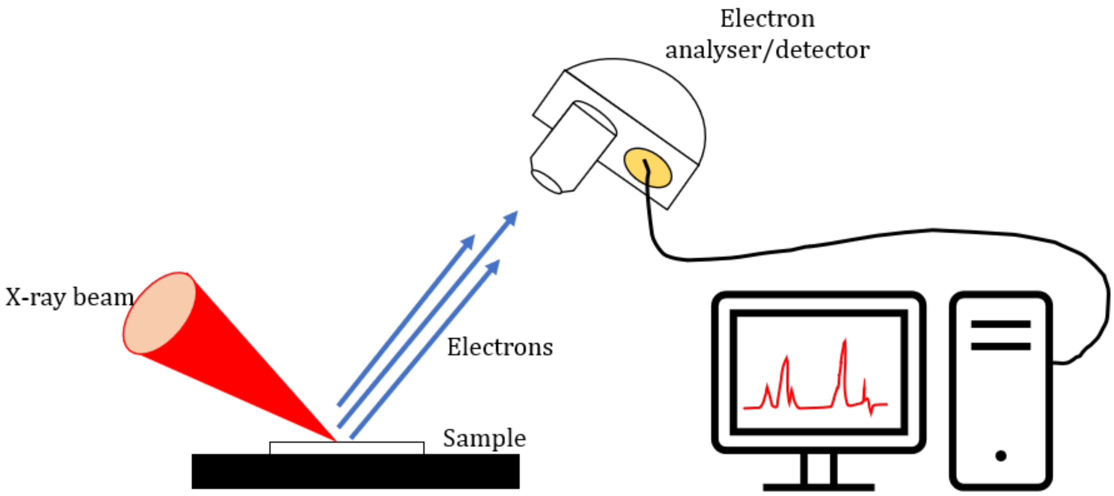

Figure 2.12: Schematic diagram of XPS

The photoelectron peaks with unique binding energy (BE) represent the element quantity and identity on the material surface. The binding energy can be calculated using **equation 2** [176].

$$E_b = hv - E_x - \phi_{sp} \qquad \text{(Equation 2)}$$

E_b = binding energy of the inner shell electron

hv = x-ray photon energy

E_k =kinetic energy

Φ_{sp} = spectrometer work function

2.6.1.1.2 Auger Electrons

Auger electron refers to a low-energy electron created during the relaxation process [186]. **Figure 2.11b** illustrates the process of Auger electrons. During the excitation of the atom by an X-ray beam, there is an electron loss in the core shell, creating an electron-hole [187]. This hole is filled by the electron from the outer shell (valence orbital), leading to a difference in energy. During this relaxation process, the excess energy is transferred to the outer shell and leaves the atoms in the forms of x-ray fluorescence and Auger electron emission [182,185,187]. The energy released by Auger electrons can be detected by the XPS.

2.6.1.1.3 Surface Sensitivity

XPS characterisation is a surface-sensitive technique because only the electron that escapes from the sample surface without any inelastic collision within the atomic structure of the sample will be detected and analysed as photoelectron peaks [182]. Generally, the x-ray beam penetrates many microns deep into the sample substrate. It is only the electrons that originate from near the surface (a top few nm) that can escape without energy losses that are diagnostic. While the electrons located deeply in the sample will lose all the energy before escaping the sample surface or reaching the detector, due to inelastic collision [182]. In some cases, the electrons involved in inelastic collisions will reach the detector and appear as a background signal due to their low energy. Therefore, the photoelectrons created at more than 2-5 nm deeper into the sample surface are less likely to escape the sample surface with enough energy to be detected [182,188].

2.6.1.2 Chemical Environment

XPS is a technique used to determine the oxidation state and the chemical environment of the sample material, where the survey spectra or wide spectra are used to identify the elemental composition of the sample surface [182,189]. While the core line spectra determine the most details in terms of the oxidation state presented on the sample surface [185].

2.6.1.3 The Chemical Shift Effect

Within a core level spectrum, the exact binding energy of electrons are influenced by the chemical environment [185]. The chemical shift occurs in relation to the electronegativity of the atoms bonded to carbon (the higher the electronegativity of the atoms, the larger the chemical shift). Therefore, it is essential to consider the chemical shift effect for XPS data analysis.

2.6.1.3.1 C1s Coreline shift

C1s binding energy is in the range of 248.5 – 285.0 eV [185,190,191]. When carbon is bound with other elements, there is a shift in binding energy caused by primary and secondary substituent effects [185]. In the case where carbon is bound to fluorine (the highest electronegative element), the largest core line shift is generated. For single fluorine substitution, the binding energy shifted by approximately 2.9 eV (primary shift) and 0.7 eV (secondary shift) [185]. While in the case of oxygen, the shift is slightly lower. The primary shift would be around 1.4 eV for single bond (C-O) and 2.8 eV for double bond (C=O) [185,191]. In terms of other functional groups, the shift is relatively small and does not show as much shift as per mentioned earlier [185].

2.6.1.3.2 N1s Coreline Shift

In the case of nitrogen-containing functional groups such as amine, amide, nitrile, and nitrogen in aromatic rings, where nitrogen is bound to carbon, the binding energy of the N1s spectrum lies in a range of 398.0 eV to 400.5 eV [192]. However, the chemical shift effect may occur if nitrogen is bound to atoms with a higher oxidation state than carbon. This leads to an increase in binding energy [185].

2.6.1.4 Summary of Carbon Chemical State Binding Energy

Table 2.5 summarises the binding energy of each carbon chemical state reference.

Table 2.5: Binding energy of carbon chemical state (reference for C1s spectra) [182,190,193].

Chemical State	**BE (eV)**
C-C or C=C	~284.8
O-C-O	~286.0
C-N	~286.0
C-O	~286.5
C-CFn	~287.1
C=O	~288.0
CF	~288.4
O-C=O	~289.0
CF-CFn	~289.9
CF_2	~292
CF_3	~293-4

2.6.2 Contact Angle (CA) Measurement

The CA is a quantitative measurement of an angle (ϴ) between the substrate surface and the liquid-vapour interface of a liquid droplet, defined by Young's equation (**Equation 3**) [176,194]. If the CA is low, the material is hydrophilic and hydrophobic at high CA, as shown in **figure 2.13**.

$$\gamma_{LV} cos\theta = \gamma_{SV} - \gamma_{SL} \qquad \text{(Equation 3)}$$

γ_{LV} = surface tension of liquid and vapour
γ_{SV} = surface tension of solid and vapour
γ_{SL} = surface tension of solid and liquid

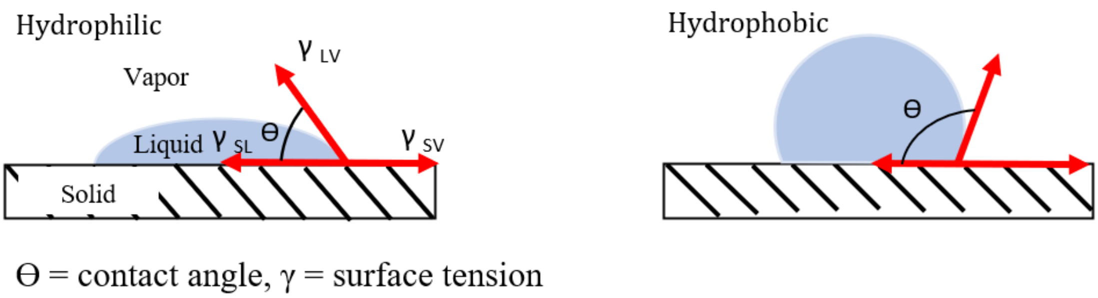

Figure 2.13: Schematic diagram of CA measurement [160]

2.6.3 SEM Characterisation

SEM characterisation is an electron microscope used to provide magnified images of the sample by scanning the sample surface with electron beams [195]. During the scanning, the electron passes through the lens until it reaches and enters the sample surface, where different interaction between electrons and the sample surface happens and creates a signal. The signals are detected and used to produce magnified images. **Figure 2.14** shows a schematic diagram of SEM.

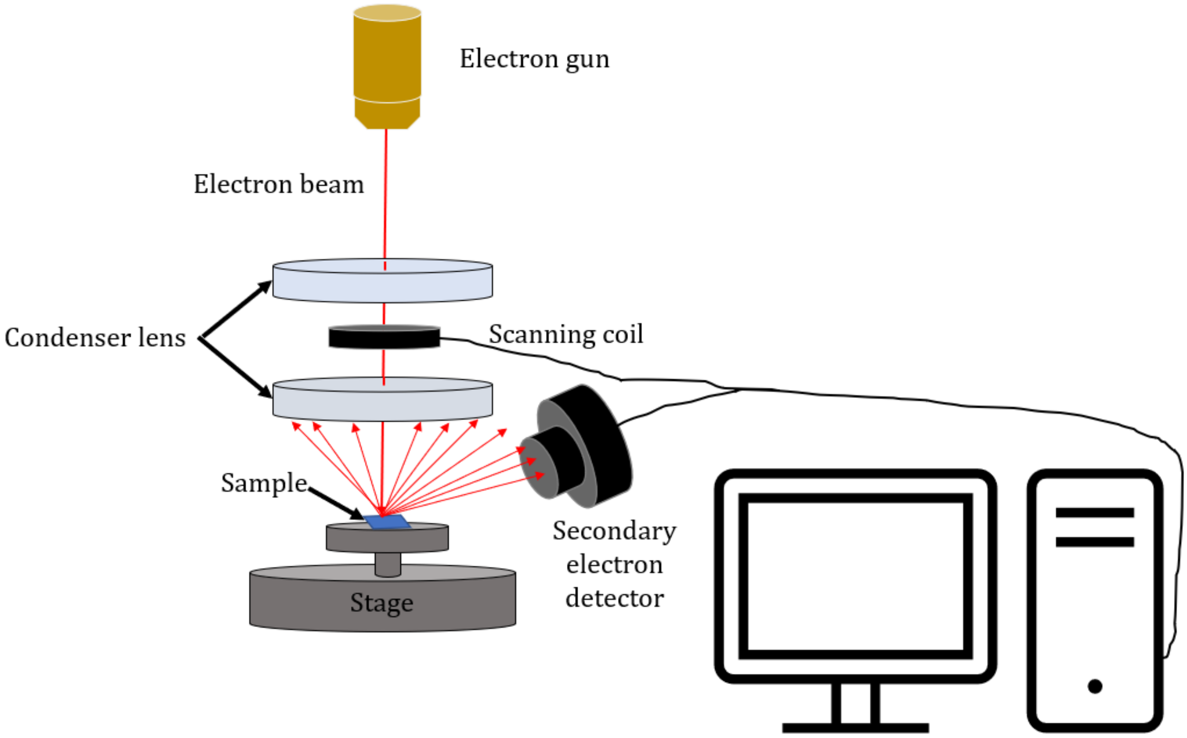

Figure 2.14: Schematic diagram of SEM characterisation

3 MWCNTs Ink Formulation Preparation and Characterisation

3.1 Introduction

This chapter focuses on formulating CNTs ink for electrode fabrication using the inkjet printer. The formulated CNTs ink aims to be compatible with a home inkjet printer and less hazardous and environmentally friendly; therefore, water-based ink is chosen as the solvent base for the ink. MWCNTs are selected for CNTs ink formulation as they are lower in cost but have higher mechanical and chemical stability [70,79]. (Refer to *Chapter 2* for details)

The first step is to identify the most homogenised CNTs ink compatible with inkjet printing. Side-wall functionalisation of a carboxylic acid group and aqueous dispersion technique will be investigated.

- Side-wall functionalisation using a mixture of nitric acid (HNO_3) and sulfuric acid (H_2SO_4). This is to functionalise and modify the CNTs sidewall to hydrophilic, to disperse in water solution.
- Aqueous dispersion using a surfactant such as sodium dodecyl benzenesulfonate (SDBS) and sodium dodecyl sulfate (SDS) to disperse CNTs in a water solution. The comparison between the two surfactants will be carried out to identify the most appropriate surfactant for CNTs dispersion in water solution and determine the suitable composition of the CNTs ink formulation.

- The combination of functionalised CNTs and a surfactant to observe the effects on their homogeneity. Even though the functionalisation of CNTs sidewall should provide hydrophilic properties, there is the possibility that some unfunctionalised CNTs remain. Therefore, this combination may enhance their dispersibility and printing performances.

To observe the associated ink dispersion and inkjet printing efficiency, these formulations will be examined on MWCNTs with different tube lengths and diameters.

The next step is to identify the most appropriate inkjet printer for CNTs ink deposition and electrode fabrication. There are two common types of inkjet printers: Thermal inkjet printers and Piezoelectric inkjet printers [25]. They differ in their printing technology and component; hence, the study of Canon inkjet printer (thermal) and Epson inkjet printer (piezoelectric) will be carried out [25,126]. (Refer to *Chapter 2* for details). Evaluation of the printing performance of the formulated inks will identify the appropriate inkjet printer for electrode fabrication and determine their compatibility.

To identify the most compatible CNTs ink, a range of analytical techniques were utilised:

1. Scanning electron microscopy (SEM) characterisation (*section 3.2.4.4.1*)
2. X-ray photoelectron spectroscopy (XPS) characterisation (*section 3.2.4.4.2*)
3. Resistance measurement (*section 3.2.4.4.3*)

3.2 Experimental and Method

3.2.1 Material and Equipment

Sulfuric acid (95%) was purchased from Fisher Scientific (CAS no: 7664-93-9). Ethanol (96%) (CAS no: 64-17-5), glycerol (CAS no: 56-81-5), multi-walled carbon nanotubes (MWCNT, 50-90 nm, >95%) (CAS no: 308068-56-6), nitric acid (70%) (CAS no: 7697-37-2), sodium dodecyl benzenesulfonate (SDBS) (CAS no: 25155-30-0), and sodium dodecyl sulfate (SDS) (CAS no: 151-21-3) were purchased from Sigma-Aldrich. Pre-functionalized multi-walled carbon nanotubes (MWCNT-COOH, 10- 30 µm length, 3-5 nm (inner diameter), 10-20nm (outer diameter), 99.9 w%), were purchased from CheapTube Inc.

An Epson XP960 A3 photo printer, and a Canon PIXMA TS205 printer and Canon black PG-745 cartridges were purchased from Seiko Epson Cooperation and Canon Inc., respectively. Whatman qualitative filter paper grade 1 (CAS no: 1001-917) was purchased from Merck. XPS was from Kratos Analytical Ltd., and SEM was from JEOL Ltd. The Digital multimeter (Fluke 116 True RMS HVAC Digital Multi-meter) was purchased from Fluke Cooperation, Netherland.

3.2.2 XPS Characterisation (Surface Analysis)

XPS analysis was performed using a Kratos Analytical Axis Supra X-ray photoelectron spectrometer (XPS) equipped with a monochromatic Al Kα source, operating at 1486.7 eV. Samples were mounted on a stage using CuBe plates. An internal flood gun was applied for neutralising charging effects on sample surfaces. Wide scan (survey) and high-resolution core-line (e.g., C1s, N1s, O1s) spectra were recorded at pass energies of 160 eV and 20 eV and step sizes of 1 eV and 0.1 eV respectively. Wide-scan and core-line spectra were recorded with a sweep time of 160 s and 120 s. Spectra were acquired using a take-off angle of 90° (relative to the surface), power of 225 W (15 kV x 15 mA) and an analysis area of 700 x 300 µm.

Data were acquired using Kratos Analytical ESCApe software. Data were converted into VAMAS format and analysed using CasaXPS (ver.2.3.23PR 1.0, Casa

Software Ltd). Spectra were quantified using linear baseline correction. All spectra were calibrated by offsetting the binding energy according to the C-C chemical state of the C1s spectrum, 285.0 eV. Peak fitting for core-line spectra was performed using expected chemical shifts from the literature [185,191].

Relative sensitivity factors (RSFs) were used to scale the measured raw peak area (selected peak region) and quantify the atomic composition information of the material surface. RSFs were set for each element, and the atomic compositions were calculated and analysed through CasaXPS software. *Appendix A* summarises the RSFs of the element used in this research project.

3.2.3 Resistance Measurement

There are multiple ways of measuring resistance using a digital multimeter. Generally, a small current is applied to the material, and the voltage drop is measured. The known current and the voltage drop measured will be used to calculate the material's resistance using Ohm's law (**Equation 4**). However, the probes may provide additional resistance to the measurement [196]. **Figure 3.1** shows a schematic diagram of a multi-meter.

$V = I \text{ x } R$ Equation 4

V = Voltage
I = Current
R = Resistance

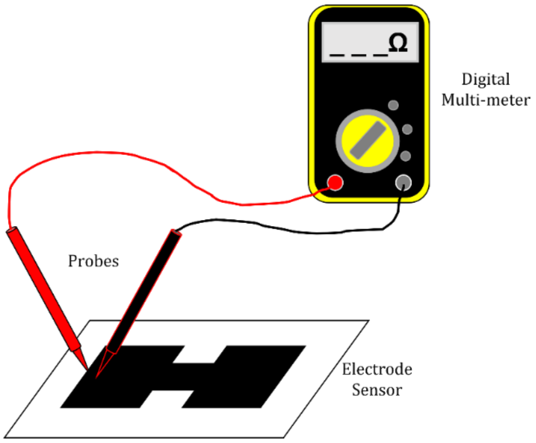

Figure 3.1: Schematic diagram of digital multimeter

3.2.4 Methodology

3.2.4.1 MWCNTs Ink Formulation

3.2.4.1.1 Formulation 1.1: Sidewall functionalisation with diluted acid mixture through magnetic stirring

Diluted acids were prepared by diluting 98% sulfuric acid (H_2SO_4) and 70% nitric acid (HNO_3) to 10 M and 4 M, respectively.

108 mg pristine-MWCNTs were added into 15 mL H_2SO_4 (10 M) and 5 mL HNO_3 (4M). The suspension was stirred vigorously at room temperature for 18 hr and 24 hr using magnetic stirring. Next, the solution was centrifuged at 4000 – 5000 rpm for 10 -15 min. The supernatant was collected, and vacuum filtered until the MWCNTs were completely pH 7. The functionalised MWCNTs were dried in an oven at 80 °C overnight and dispersed in DI water (5 mg/mL). Glycerol was added at a 1: 3 ratio (glycerol: water) and filtered with a 0.2 μm Millipore syringe filter. 1 mL of the ink formulation was sonicated until homogenised and ready for printing.

3.2.4.1.2 Formulation 1.2 & 1.3: Preparation of Pristine-MWCNTs in Aqueous Solution with SDS/ **SDBS surfactant**

50 mg of SDS (*formulation 1.2)* and SDBS (*formulation 1.3*) were dispersed in 20 mL of DI water in two separate vials, followed by 100 mg of MWCNTs in each solution. The mixtures were sonicated at room temperature for 30 min until the suspension was thoroughly homogenised. Then, the mixtures were centrifuged at 3000 rpm for 2 min to remove any MWCNTs bundles from the well-dispersed MWCNTs. This was conducted to prevent nozzle clogging during the printing process. The supernatant was collected, and glycerol was added at a volume ratio of 1:3 (glycerol: water).

3.2.4.1.3 Formulation 1.4: Pristine-MWCNTs-COOH dispersed in aqueous solution using SDS surfactant

7 wt% SDS was added into the water solution and sonicated until homogenised. Next, 10 wt% pristine-MWCNTs-COOH was added to the solution and sonicated until homogenised.

3.2.4.1.3.1 Weight-ratio Observation

To study the effect of surfactant on ink formulation homogeneity and identify the most appropriate amount of surfactant, the ink formulation was prepared with the same technique but varying in wt% of SDS, from 1wt% to 10wt%, and a fixed amount of MWCNTs at 7wt%.

Other MWCNTs ink formulations attempted are listed in *Appendix A*. These formulations varied in time, temperature, and homogenising process.

3.2.4.2 Printer Cartridge Preparation

For the Epson piezoelectric inkjet printer, no cartridge preparation is required as the cartridges were purchased ink-free.

For the Canon thermal inkjet printer, the sponge was removed from the cartridge. Then, the cartridge and the sponge were cleaned with ethanol and water separately until the cartridge was ink-free, using an ultrasonic bath. After the cleaning process, the cartridge was left to dry for 1-2 hr(s) at room temperature before adding the formulated ink.

3.2.4.3 CNTs Ink Printing Observation

The formulated inks were repeatedly printed as a straight line (1.5 cm x 10 cm) for 50 printing cycles to observe their consistency, accuracy, and precision. After each printing cycle, the printing was left to try for 2-3 min before the subsequent printing. This is to prevent any unnecessary inaccuracy caused during ink penetration and printing.

3.2.4.4 CNTs Ink Formulation Observation and Characterisation

3.2.4.4.1 SEM Characterisation

The formulated CNTs inks printed on Whatman filter papers were cut into 1 cm x 1cm sizes for SEM characterisation. The morphology of CNTs printings was characterised at 1000x, 10000X, 15000x, and 40000x. ImageJ software was used to quantify the number of CNTs deposition per unit area and the diameter and length of the CNTs. A standard of the mean was calculated.

3.2.4.4.2 XPS Characterisation

1 mL of CNTs ink was pipetted onto a paper substrate and characterised through XPS. Survey (wide spectra), and C1s, O1s, Na 1s, and S2s spectra were recorded at pass energies for 120.00 sec, three scanning for each sample per spectrum. The data were analysed by CasaXPS (ver.2.3.22PR 1.0, Casa Software Ltd). Peak fitting for core-line spectra was performed using expected chemical shifts from the literature [185,191].

3.2.4.4.3 Resistance Measurement

3.2.4.4.3.1 Critical Concentration Determination

Formulation 1.1 was prepared into different concentration from 0.25 mg/mL and 0.5 mg/mL to 6.0 mg/mL at 0.5 mg/mL intervals. 1mL of the formulated inks were dropped onto Whatman filter paper grade 1 using a pipette. Resistance was measured at 1 cm in length between probes. Ten measurements were conducted for each concentration, and a standard error of the mean was calculated.

3.2.4.4.3.2 Fabricated Electrode Sensor Resistance Measurement

The fabricated CNTs electrode sensor on filter paper resistance was measured at 1 mm – 20 mm (1 mm interval) length between probes. Three measurements were conducted for each interval, and a standard of the mean was calculated.

3.3 Results and Discussion

3.3.1 Ink Formulation Observation

3.3.1.1 Formulation 1.1

Figure 3.2 shows the CNTs ink of side-wall functionalised MWCNTs in water solution at 5 mg/mL. Visually, the CNTs are homogeneously dispersed in the water solution. Compared to the other CNTs ink formulations (*attempts 1-3*, *Appendix A*), *formulation 1.1* contains fewer CNTs clusters and precipitation. This is possibly due to more carboxylic acid group functionalisation on the CNTs sidewall, which initiates bonding with water molecules and enhances CNTs dispersion in water solution.

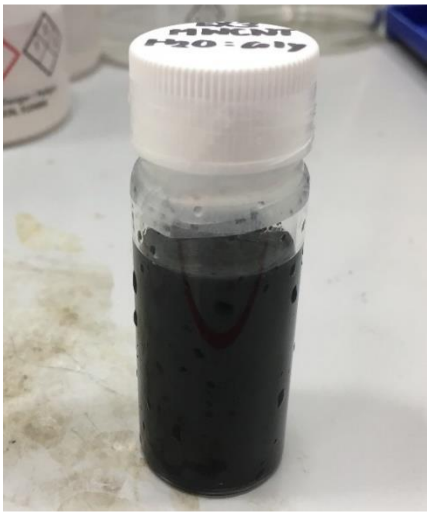

Figure 3.2: Side-wall functionalised MWCNTs in water solution (5mg/mL)

3.3.1.1.1 Critical Concentration Determination Using Resistance Measurement

Figure 3.3 shows the resistance of *formulation 1.1* at different concentrations (0.5 mg/mL to 6.0 mg/mL) on Whatman filter paper grade 1. This is to identify the critical concentration of the CNTs ink, where resistance becomes constant as a function of MWCNTs concentration.

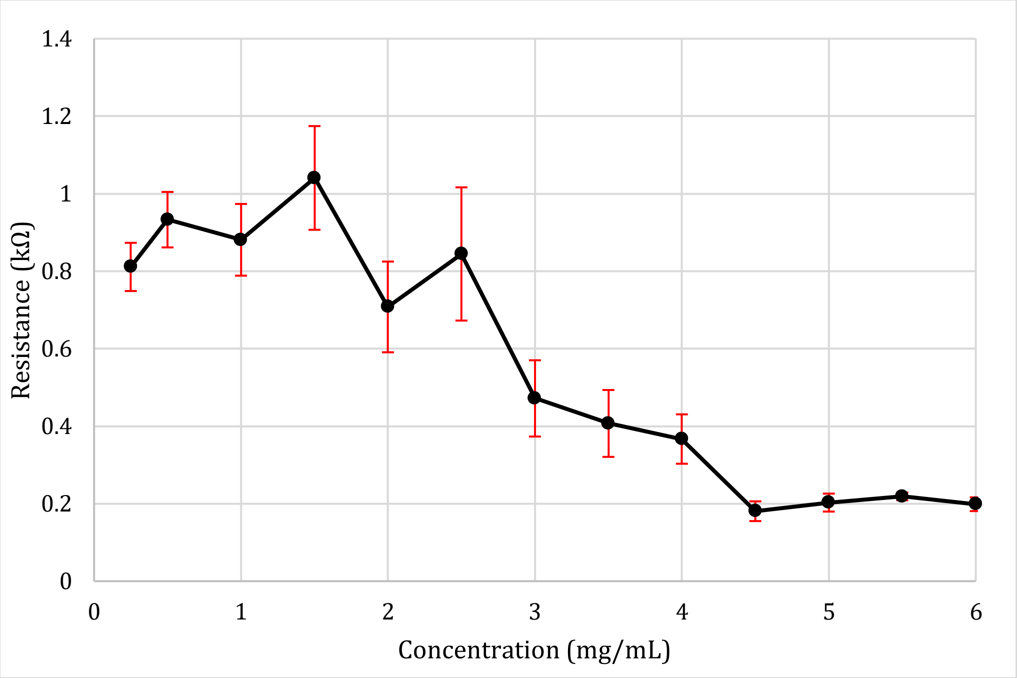

Figure 3.3: Resistance measurement of *formulation 1.1* at 2.5 mg/mL to 6.0 mg/mL (1 cm length between probes measurement)

Figure 3.3 shows high resistance (0.81± 0.06 kΩ at 0.25 mg/mL) until approximately 2.5 mg/mL (0.84 ± 0.17 kΩ). The resistance decreases gradually as the concentration increases and reaches its plateau at approximately 4.5 mg/mL with a resistance of 0.18 ± 0.03 kΩ. This is due to the concentration of MWCNTs present and their associated connectivity. When more MWCNTs are present, there is an increase in connectivity between CNTs. This is due to increased conduction pathways, allowing electrons to flow more effectively. This is determined quantitatively by measuring the resistance. Nevertheless, there is a finite point where the CNTs conductivity becomes stable. Therefore, *formulation 1.1* was prepared at a 5 mg/mL concentration for inkjet printing.

3.3.1.1.2 SEM Characterisation

Figure 3.4 shows the SEM images of *formulation 1.1* (5 mg/mL) deposited on Whatman filter paper grade 1. As shown in the images, CNTs are densely packed on the substrate surface with high connectivity, explaining the obtained conductivity. Quantitatively, the number of MWCNTs presented per unit area is approximately 17.0 ± 0.7 CNT/μm^2. The CNTs are approximately 78.6 ± 2.4 nm in diameter and 5.3 ± 0.2 μm in length. The measured CNTs length highlights the breakage of CNTs during acid treatment since the length of pre-treated MWCNTs (9.11 ± 0.03 μm) is longer, indicating challenges in controlling the length of CNTs that could lead to nozzle clogging during the printing process. Therefore, further investigation is required to improve the precision.

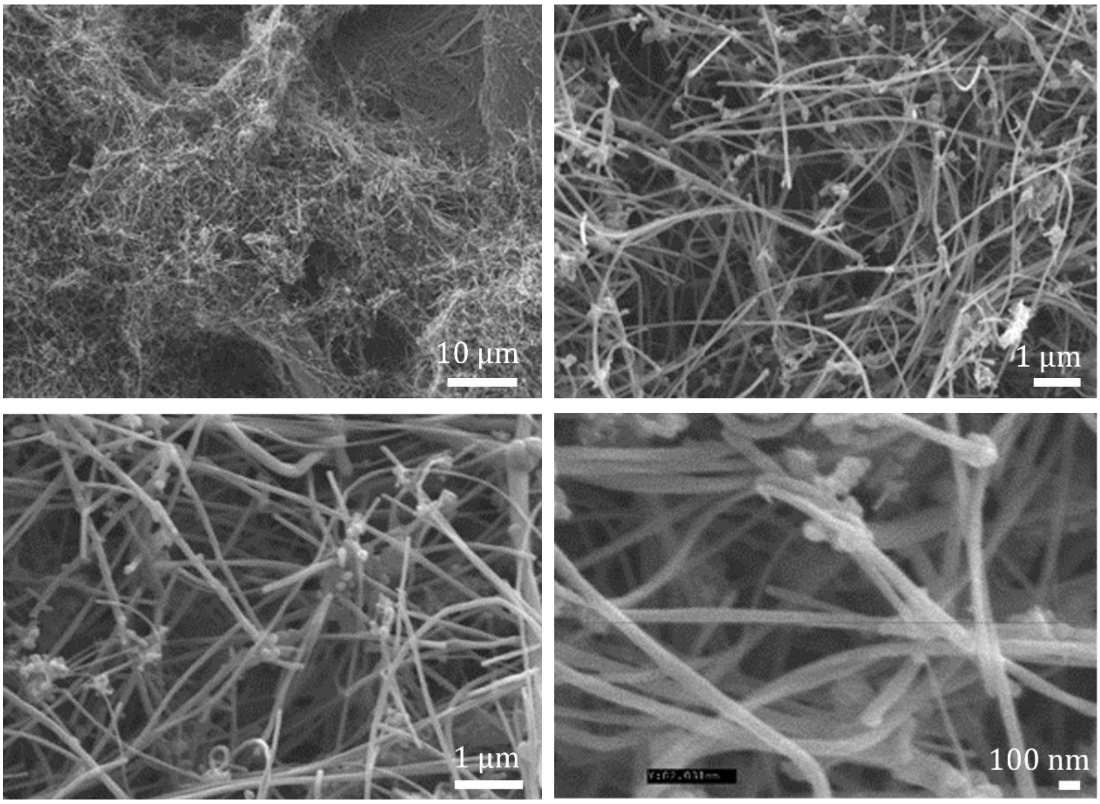

Figure 3.4: SEM images of *formulation 1.1* (MWCNT-COOH in DI water) at 5.0 mg/mL concentration on Whatman filter paper grade 1

3.3.1.2 Formulation 1.2 and Formulation 1.3

Since sidewall functionalisation may lead to CNTs breakage, aqueous dispersion using SDS (*formulation 1.2*) and SDBS (*formulation 1.3*) was investigated. Visually, the homogeneity of the formulated inks is very similar; nevertheless, the printing performances for these two formulations will be discussed later in the chapter.

3.3.1.2.1 SEM Characterisation

Figure 3.5 and 3.6 shows the SEM images of *formulation 1.2* (pristine-MWCNTs with SDS in DI water) and *1.3* (pristine-MWCNTs with SDBS in DI water), respectively. The CNTs deposition offers high connectivity between CNTs, at approximately 15.2 ± 0.4 CNT/μm^2 for both formulations. The number of CNTs presented is slightly lower compared to the previous formulation. This is possibly due to the length of CNTs, which is longer since there is no such CNTs modification in this dispersion process. Therefore, the length of the CNTs remains the same as the pristine-MWCNTs, at approximately 15.4 ± 0.4 μm.

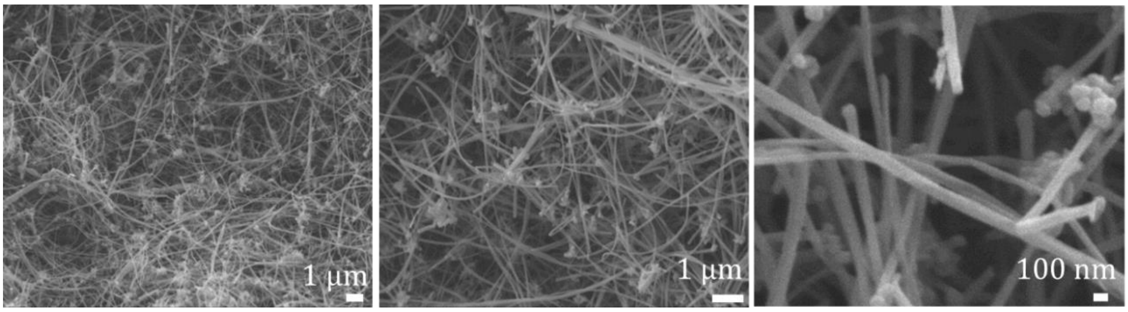

Figure 3.5: SEM images of *formulation 1.2* (pristine-MWCNTs with SDS in DI water) on Whatman filter paper grade 1

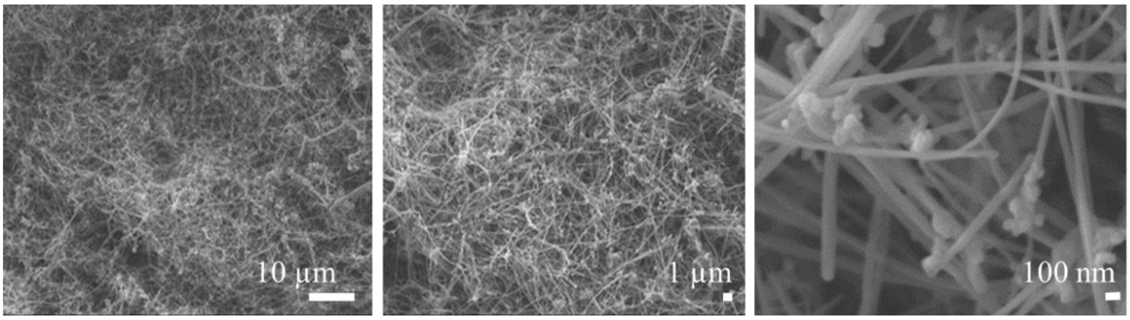

Figure 3.6: SEM images of *formulation 1.3* (pristine-MWCNTs with SDBS in DI water) on Whatman filter paper grade 1

3.3.1.3 Formulation 1.4

Formulation 1.4 comprises thinner but longer MWCNTs-COOH with 10 – 20 nm diameter and 10 -30 μm length. Pristine-MWCNTs-COOH was prepared with the addition of SDS surfactant to enhance their dispersibility. The purpose of using smaller MWCNTs is to observe their behaviour on the formulated CNTs ink homogeneity and their printing efficiency. The solution presented less clustering and aggregation, and the formulation required a much shorter preparation process. Using pristine-MWCNTs-COOH prevents unpredictable CNTs length and size varieties during the formulation process.

3.3.1.3.1 Effects of Surfactant towards Ink Formulation

Formulation 1.4 was prepared with a different wt% SDS (1 wt% to 10 wt%) but a fixed concentration of CNTs (10 wt%) to identify the optimal wt% SDS for CNTs ink formulation. The formulated CNTs inks were left standing overnight. As a result, the CNTs ink with less than 5 wt% SDS precipitates while the rest remain homogenised. This shows that the presence of SDS does influence the CNTs dispersibility. Theoretically, MWCNTs-COOH can disperse in the water solution since they contain carboxylic acid groups, which are polar; therefore, 'like-dissolves-like'. However, in this research, the addition of SDS shows an improvement in dispersibility. SDS likely formed a double layer on the MWCNTs-COOH. A hydrophilic head faced towards MWCNTs-COOH while the hydrophobic tail was attaching to another hydrophobic tail of another SDS surfactant. Despite that, further investigation will be required to confirm this statement.

3.3.1.3.2 SEM Characterisation

Figure 3.7 shows the SEM images of *formulation 1.4* (7wt% SDS and 10wt% MWCNT-COOH in DI water) deposited on Whatman filter paper grade 1.

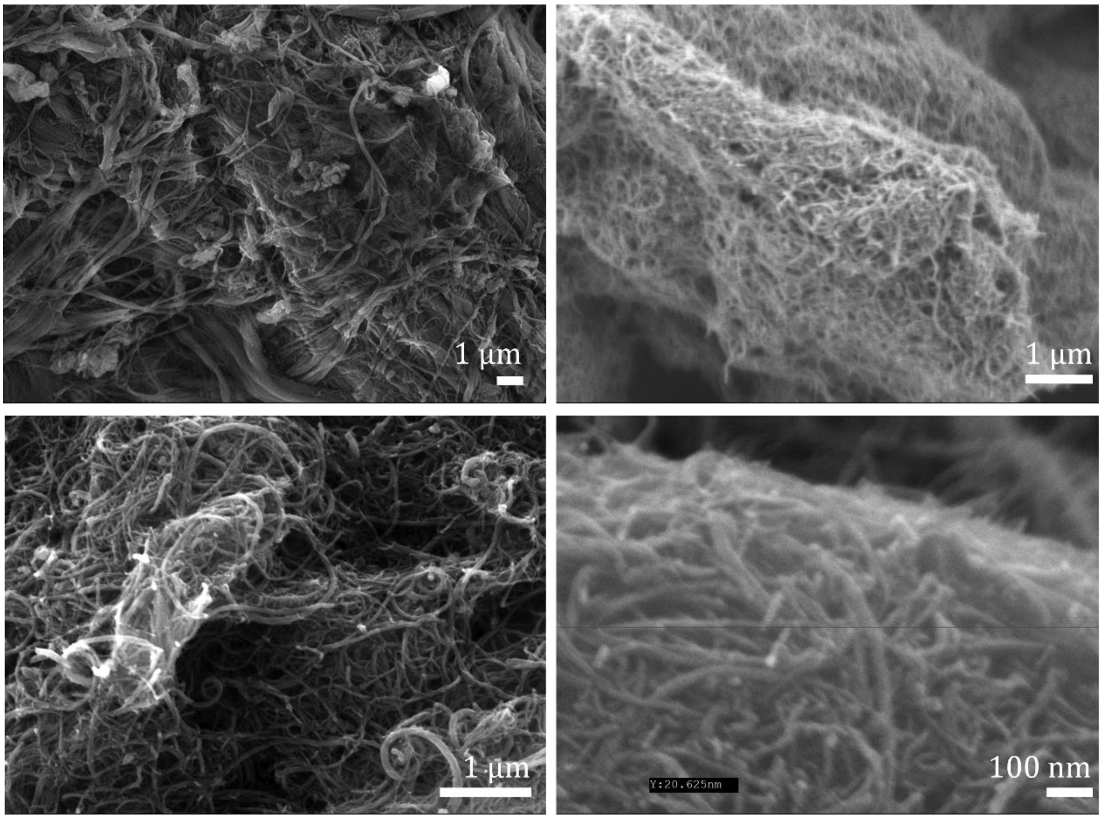

Figure 3.7: SEM images of *formulation 1.4* (7wt% SDS and 10wt% MWCNT-COOH in DI water) on Whatman filter paper grade 1

As shown in **Figure 3.7**, the CNTs are more densely packed than in *formulation 1.1* (**Figure 3.4**, *section 3.3.1.1.2*) due to their smaller diameter. Quantitatively, the number of CNTs presented per unit area is approximately 118.2 ± 3.9 CNT/µm^2

with 29.8 ± 0.8 nm in diameter and 10.1 ± 0.02 μm in length. With a higher number of CNTs, there is a higher chance that CNTs will be in contact with each other; hence, there is likely more connectivity and conductivity.

It can be concluded that *formulation 1.4* may likely perform more efficiently in inkjet printing as the CNTs are smaller in size and are less likely to cause nozzle clogging during the electrode preparation process through inkjet printing.

3.3.1.3.3 XPS Characterisation

To study the chemistry of the formulated CNTs ink, XPS was performed on *formulation 1.4*. **Figure 3.8** shows wide spectra and C1s spectra of *formulation 1.4.* The spectra consist of counts per second (cps) against the specific BE of the atom. The intensities of the BE are used to calculate the atomic percentages (%) of each element, as summarised in **Tables 3.1 and 3.2**.

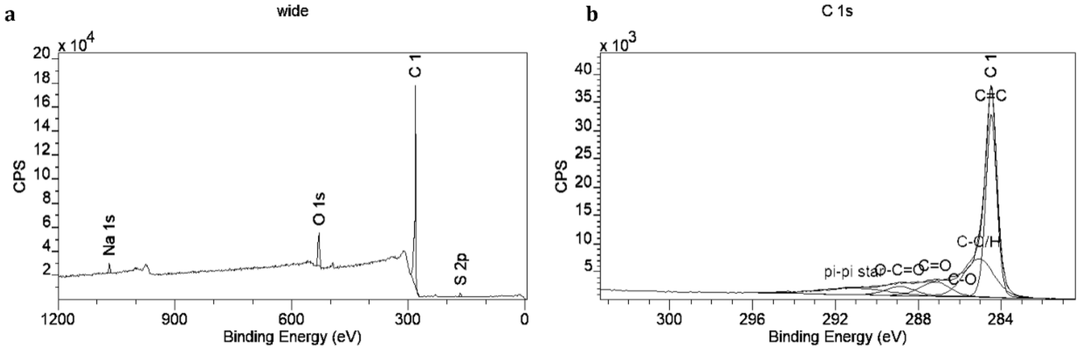

Figure 3.8: a) Wide and b) C1s spectra of CNTs ink (*formulation 1.4*) on Whatman filter paper grade 1

Table 3.1: Atomic percentages of CNTs ink (formulation 1.4) on Whatman filter paper grade 1

	C 1s	O 1s	S 2p	Na 1s
CNTs ink	90.6 %	7.9 %	0.9 %	0.7 %

Table 3.2: Area percentages of CNTs ink (formulation 1.4) on Whatman filter paper grade 1

	C=C	C-C/H	C-O	C=O	O-C=O	π -π*
BE (eV)	284.5	285.0	285.9	287.2	288.9	291.1
CNTs ink	45.4 %	26.0 %	2.2 %	9.6 %	6.3 %	10.5 %

The wide spectra, **Figure 3.8a**, shows the composition of CNTs ink at of 90.6 % carbon (C), 7.9 % oxygen (O), 0.9 % sulfur (S), and 0.7 % sodium (Na), **Table 3.1**.

S and Na content represents the SDS surfactant, while other compositions (C and O) were from the MWCNTs-COOH.

The C1s spectra, **Figure 3.8b**, shows 45.4 % C=C (284.5 eV), 26.0 % C-C/H (285.0 eV), 2.2 % C-O (285.9 eV), 9.6 % C=O (287.2 eV), 6.3 % O-C=O (288.9 eV), and 10.5 % π -π^* (291.1 eV) (**Table 3.2**). However, since the formulated ink was characterised on Whatman grade 1 filter paper, there is a possibility that the composition of the paper substrate is also presented in the data. Therefore, further XPS characterisation on the formulated ink will be investigated on different substrate types for comparison.

Figure 3.8b and Table 3.2 also highlights the ratio between C=C and π -π^* at 4.5:1 (C=C: π -π^*). The ratio will be used as a standard to investigate CNTs ink printing on the substrates.

3.3.2 Thermal Inkjet Printer and Piezoelectric Inkjet Printer Comparison and Observation

To identify the most appropriate inkjet printing system for electrode fabrication, the Epson inkjet printer and the Canon inkjet were used to print the formulated CNTs inks (*formulation 1.1 – 1.4*) onto Whatman filter paper grade 1 for 50 printing cycles.

3.3.2.1 Epson Inkjet Printer

Figure 3.9 shows the CNTs printing performance on Whatman filter paper grade 1. *Formulation 1.1* (**Figure 3.9a**), *formulation 1.2* (**Figure 3.9b**), and *formulation 1.3* (**Figure 3.9c**) was printed onto the filter paper for 50 printing cycles.

Figure 3.9: *Formulation* a) *1.1* (MWCNT-COOH in DI water), b) *1.2* (pristine-MWCNTs with SDS in DI water), and c) *1.3* (pristine-MWCNTs with SDBS in DI water) printed on filter paper by Epson inkjet printer (50 printing cycles)

As shown in **Figure 3.9**, darker shades can be spotted on all three ink formulations, indicating CNTs deposition, especially on *formulation 1.1* (**Figure 3.9a**). While fewer CNTs ink deposition is obtained from *formulations 1.2* (**Figure 3.9b**) *and 1.3* (**Figure 3.9c**) due to CNTs cluster formation in the ink cartridge during the printing process. Besides, no measurable conductivity is detected, indicating a lack of CNTs connectivity.

3.3.2.1.1 SEM Characterisation

Figure 3.10 illustrates the SEM images of *formulation 1.1* (**Figure 3.10a**), *formulation 1.2* (**Figure 3.10b**), and *formulation 1.3* (**Figure 3.10c**) printed on Whatman filter paper grade 1 for 50 printing cycles.

As shown in **Figure 3.10**, all three CNTs ink formulations show a lack of CNTs deposition, especially *formulations 1.2* (**Figure 3.10b**) and *1.3* (**Figure 3.10c**), confirming why there is no sign of conductivity detected. The lack of CNTs ink deposition is likely caused by the printer construction, where the printer is operated with a built-in print head and nonremovable sponge within the cartridge. Due to the experienced CNTs aggregation, the nozzle is clogged, and the printhead cannot be removed for cleaning. This prevents the printer from providing full ink deposition efficiency. Moreover, the sponge within the cartridge might have reduced the amount of MWCNTs passing through the nozzle head onto the paper.

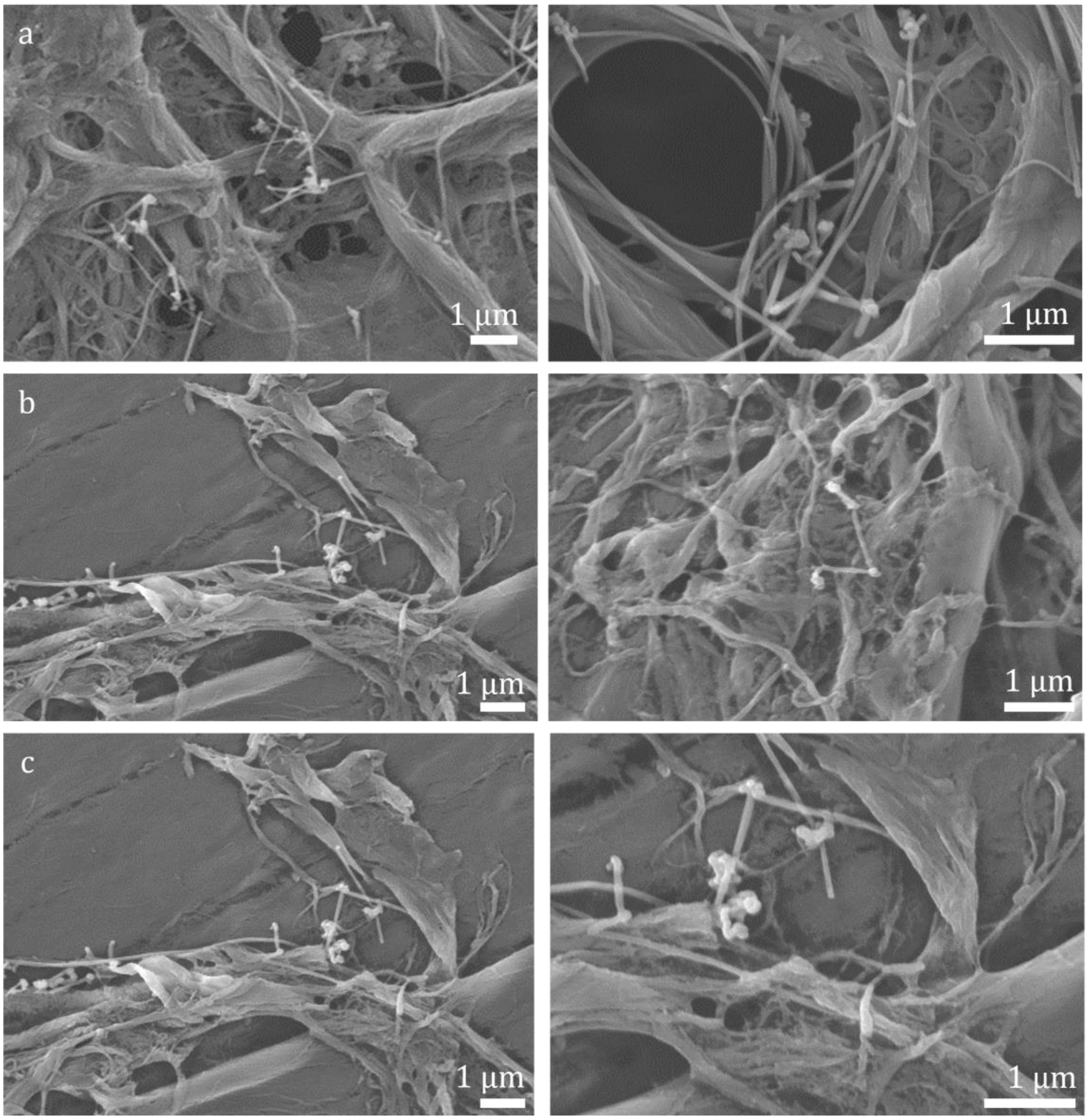

Figure 3.10: SEM images of a) *1.1*, b) *1.2*, and c) *1.3* printed on Whatman filter paper grade 1 using Epson inkjet printer (50 printing cycles)

It was concluded that the Epson inkjet printer might not be appropriate for CNTs inkjet printing, and *formulation 1.2* and *1.3* shows a lack of ink deposition and compatibility, which may not be suitable for electrode sensors fabrication.

3.3.2.2 Canon Inkjet Printer

The Canon inkjet printer differs from the Epson inkjet printer by the printing technology and the cartridge construction. In the case of the Canon inkjet printer, the printhead is attached to the cartridge, meaning that the printhead is replaceable. Therefore, this prevents the problems such as nozzle clogging. Besides, the sponge inside the cartridge can be removed entirely without affecting the printing efficiency. This means that the formulated ink will print without any blocking.

3.3.2.2.1 Formulation 1.1

Figure 3.11 shows the printing of *formulation 1.1* on Whatman filter paper grade 1 using a Canon inkjet printer for 50 printing cycles (**Figure 3.11a**) and the SEM images (**Figure 3.11b**).

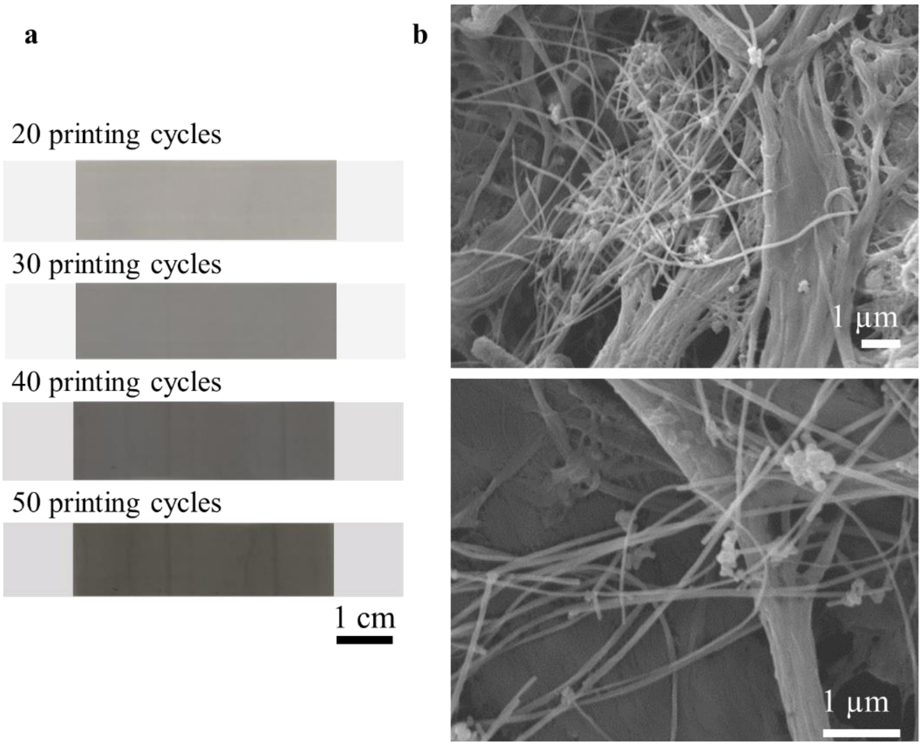

Figure 3.11: a) *Formulation 1.1* printed on filter paper by Canon inkjet printer (50 printing cycles) and b) SEM images of *formulation 1.1* printed on filter paper.

It can be seen in **Figure 3.11a** that the presence of CNTs appeared after 20 printing cycles, indicating more CNTs deposition on the paper substrate. The intensity increased as the printing continued. However, the ink spread out from the designated area. This is possibly due to the filter paper porosity and thickness, which allows the formulated ink to penetrate through. Therefore, using a thicker paper substrate could help to prevent this.

Figure 3.11b confirms the presence of CNTs deposition; however, there is an inconsistency in CNTs distribution throughout the paper substrate. Compare **Figure 3.11** to **Figure 3.9 and Figure 3.10**; more CNTs ink is deposited onto the filter paper using the Canon inkjet printer than the Epson inkjet printer, indicating better compatibility with CNTs ink. Therefore, the Canon inkjet printer will be used throughout this research.

Figure 3.9 to **Figure 3.11** also highlights that *formulation 1.1* may not be compatible for inkjet printing since both inkjet printers experienced nozzle clogging and lack of CNTs ink deposition. Therefore, it can be concluded that *formulation 1.1* is not compatible with electrode sensor fabrication.

3.3.2.2.2 Formulation 1.4

Figure 3.12 shows the electrode sensor design (**Figure 3.12a**), the fabricated electrode sensor using *formulation 1.4* (**Figure 3.12b**), the SEM image of the fabricated electrode sensor top view (**Figure 3.12c**), and cross-section (**Figure 3.12d and e**). **Figure 3.13** shows the resistance measurement of the fabricated electrode sensors regarding the distance between probes.

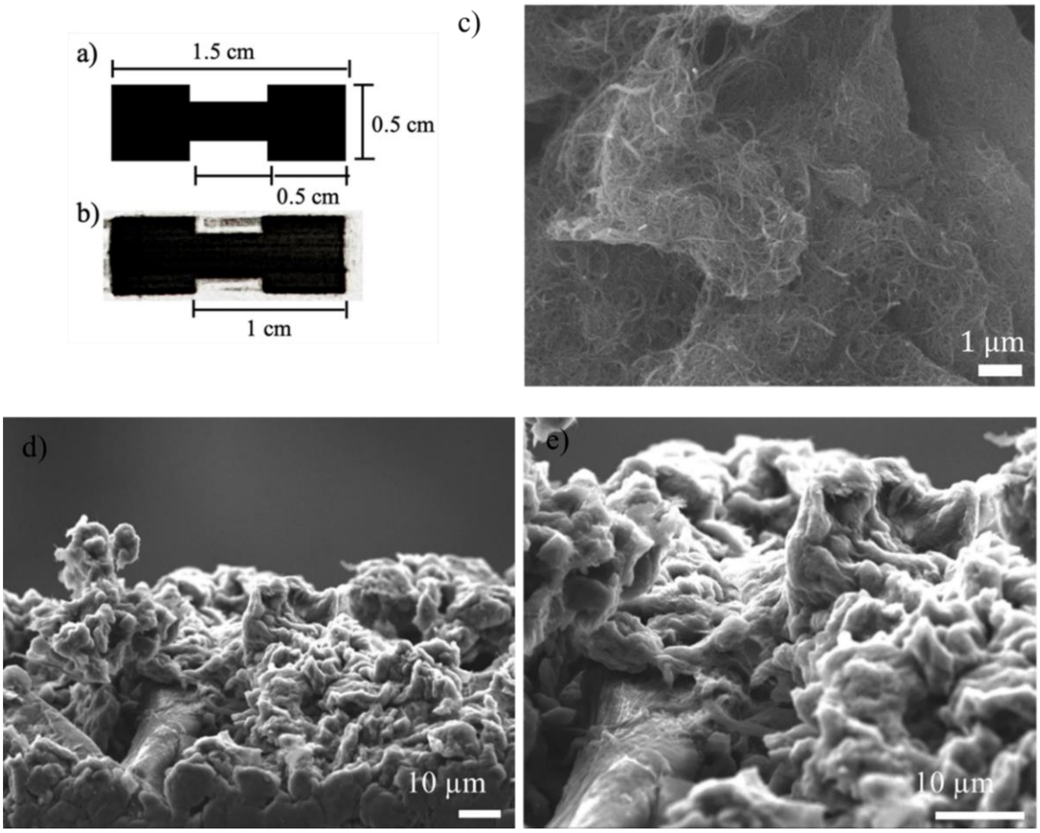

Figure 3.12: a) electrode template, b) formulation 1.4 printed on Whatman filter paper grade 1 (50 printing cycles), SEM image of the electrode sensor, c) top-view and d) and e) cross-section.

As shown in **Figure 3.12b**, the deposited CNTs ink is much darker than the printing on *formulation 1.1-1.3*, confirming more CNTs deposition. SEM images, **Figure 3.12c**, confirm CNTs deposition throughout the paper substrate with high density and connectivity at approximately 105 ± 5.9 CNTs/μm^2. However, due to the porosity of the filter paper substrate, the CNTs thickness was inconsistent throughout the printed area, as confirmed in **Figure 3.12d and e**. There are some areas where the filter paper is presented without any CNTs coverage; hence, further printing may be required to cover the substrate surface entirely.

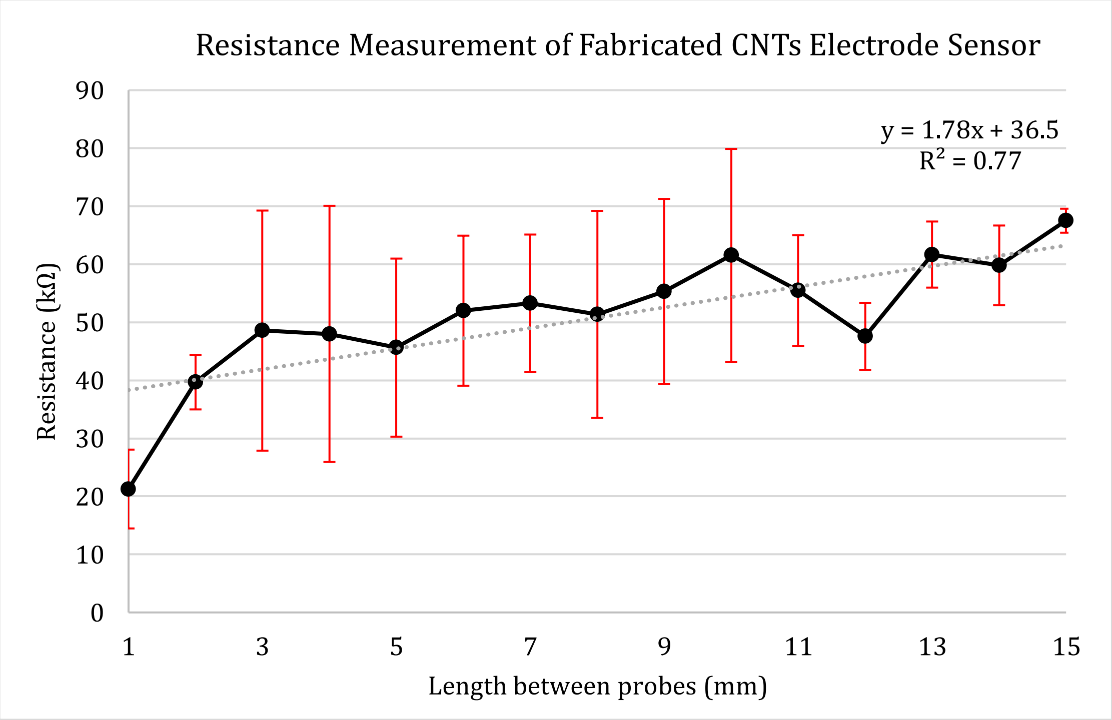

Figure 3.13: Resistance measurement of formulation 1.4 printed on Whatman filter paper grade 1 (50 printing cycles)

The resistance of the fabricated electrode sensor was measured, as shown in **Figure 3.13**. The resistance increases as the length between the probe increase, where no steady resistance is spotted. The fabricated electrode sensor has a specific resistivity of 1.78 ± 0.11 kΩm, indicating that the material is conductive and appropriate for further detection.

3.4 Conclusion

The CNTs ink formulations were prepared and studied to determine the most compatible ink for electrode fabrication using inkjet printing. *Formulations 1.1* (side-wall functionalised MWCNTs dispersed in water solution) and *1.4* (pristine-MWCNTs-COOH dispersed in water solution using SDS) were the two outstanding CNTs ink formulations regarding their homogeneity and inkjet printing efficiency. The two CNTs ink formulations were compared as they are different in terms of MWCNTs length, diameter, and the preparation process. SEM shows higher connectivity between CNTs in *formulation 1.4* once deposited by the Canon inkjet printer. CNTs are densely packed throughout the designated areas of approximately 105 ± 5.9 CNTs/μm^2. XPS characterisation also confirmed the expected chemical composition of the formulated ink. Different ink compositions of *formulation 1.4* were studied where the wt% of SDS was varied while the concentration of MWCNTs remained constant. The results show that the formulated ink becomes homogenised when SDS is over 5 wt%.

The Epson and Canon inkjet printers were studied due to the differences in printing technology. SEM confirmed that the Canon inkjet printer provides more CNTs ink deposition than the Epson inkjet printer. However, in the case of *formulation 1.1,* there were printing difficulties on both Epson and Canon inkjet printers which caused the nozzle to clog. Even though the CNTs deposition is successful, the printed material is not conductive enough to fabricate an electrode. Therefore, *formulation 1.4* was more appropriate for electrode fabrication with a measured specific resistivity of 1.78 ± 0.11 kΩm.

Therefore, in the next chapter, different paper substrates will be investigated to identify the most appropriate paper substrate for CNTs printing and electrode fabrication.

4 Paper-based Electrode Sensors and Paper Substrates Comparison

As shown in *Chapter 3*, the CNTs-based electrode sensor fabricated on Whatman filter paper grade 1 suffered from CNTs ink spreading out of the designated area due to the paper thickness and ink adsorption, making the fabricated electrode sensor inaccurate. Different types of paper substrates will be investigated to overcome this challenge, as discussed in this chapter.

4.1 Introduction

This chapter investigates different types of paper substrates to identify the optimal paper substrate for electrode sensor fabrication using an inkjet printer. The paper substrates with different porosity, thickness, texture, and surface chemistry, including Whatman filter paper grade 1 and 3, matte paper and glossy paper, will be examined.

In the first step, the interaction between the formulated CNTs ink (refer to *Chapter 3* for details) and the paper substrates will be studied. This is to get a general understanding of the paper substrate surface characteristics.

The second step is to observe the paper substrate compatibility with the CNTs ink through electrode fabrication using a Canon inkjet printer. The printing accuracy and precision, as well as the fabricated electrode sensor durability, will be investigated.

To assess the paper substrate characteristics and electrode sensor fabrication efficiency, a range of analytical techniques were utilised:

1. Printing test
2. SEM characterisation (*section 4.2.3.3.1*)
3. Resistance measurement (*section 4.2.3.3.2)*
4. XPS characterisation (*section 4.2.3.3.3*)
5. Anodic stripping voltammetry (ASV) analysis (*section 4.2.2*)

4.2 Experimental and Method

4.2.1 Material and Equipment

Whatman qualitative filter paper grade 3 (CAS no.: 1003-917) was purchased from Merck. Premium glossy photo paper and matte photo paper were purchased from Wilko Retail Ltd. Screen-printed carbon on PVC substrate was purchased from PINE research instrumentation, Durham, United Kingdom (UK). The platinum counter electrode was purchased from Jiangsu Premium Electric Instrument Co. Ltd, China.

The potentiostat was purchased from EMStat3 PalmSens, Alvertek Ltd., Romsey, UK. PSTrace software was purchased from PalmSens. ImageJ software was purchased from ImageJ. Other materials and characterisation techniques are the same as previously mentioned in *section 3.2.1, Chapter 3*.

4.2.2 Anodic Stripping Voltammetry (ASV) Analysis

ASV analysis comprises two steps: 1. pre-concentration (Reduction) and 2. Anodic stripping analysis (Oxidation). The potential is applied to preconcentrate the target species onto the WE surface, in which the preconcentration duration is controlled by the deposition time. This allows the electrode sensor to detect the target species at a lower detection limit [197]. Next, the preconcentrated target species are stripped back to the sample solution, which then be detected through potential scanning. As a result, the current created will correspond to the concentration of the target species [198]. **Figure 4.1** shows the schematic diagram of an ASV analysis sensing system.

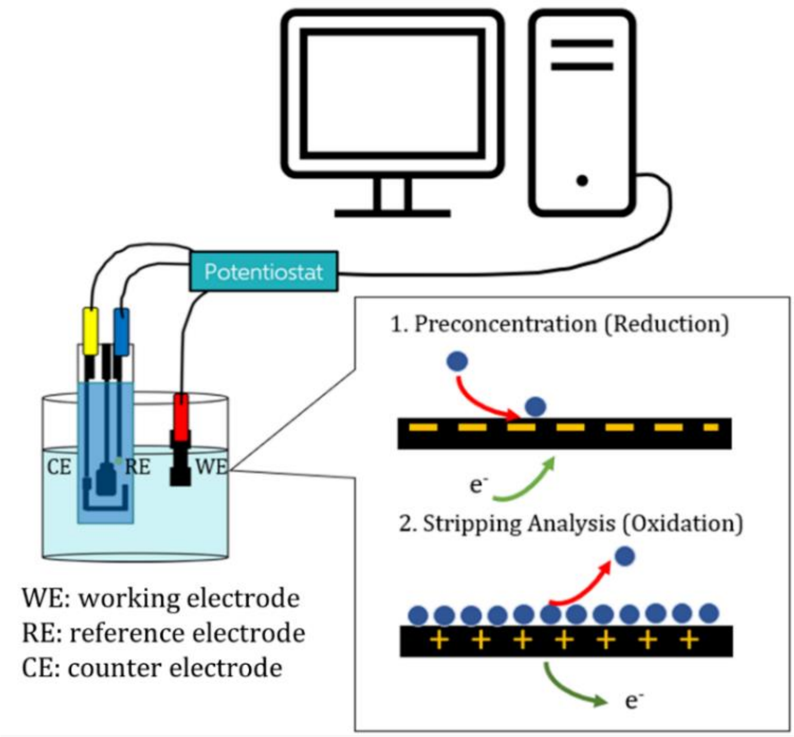

Figure 4.1: A schematic of the ASV analysis setup

4.2.3 Methodology

4.2.3.1 Observation of the Paper Substrate Interaction with the Formulated CNTs Ink

1 mL of CNTs ink was pipetted onto the paper substrates to observe their interaction and identify the most compatible paper substrate for electrode sensor fabrication visually.

4.2.3.2 CNTs Printing on Different Types of the Paper Substrate

The CNTs ink was printed onto each paper substrate for 50 printing cycles. After each cycle, the printing was left to dry for 2-3 mins before the next printing.

4.2.3.3 Characterisation

4.2.3.3.1 SEM Characterisation

The top-view morphology of uncoated paper substrates and CNTs printed paper substrates were characterised at 5000x, 15000x, and 20000x magnification. Number of CNTs deposition per unit area and the CNTs length and diameter were measured using ImageJ. The standard of the mean was calculated.

4.2.3.3.2 Resistance Measurement

The fabricated CNTs electrode sensor on each paper substrates resistance was measured at 1 mm – 20 mm (1 mm interval) length between probes. Three measurements were conducted for each interval, and a standard of the mean was calculated. Refer to *Chapter 3* for full details.

4.2.3.3.3 XPS Characterisation

The paper substrates survey (wide spectra), C1s, and O1s spectra were recorded at pass energy for 120.00 sec, three scanning for each sample per spectrum. The data were analysed by CasaXPS. Peak fitting for core-line spectra was performed using expected chemical shifts from the literature [185,191]. Refer to *Chapter 3* for full details.

4.2.3.3.4 Anodic Stripping Voltammetry Analysis (ASV)

ASV was used to observe their sensing performance. A platinum electrode was used as a CE and a silver/silver chloride on a commercial screen-printed carbon on PVC substrate as a RE. PSTrace5 software was used to measure 10 ppm copper (Cu) in 0.5M acetate buffer (provided by a colleague in the research group) at 5 sec deposition time repetitively and 5 sec to 60 sec (10 sec intervals) at 100 µA current range, at a deposition potential (E) from -0.6V to 0.4V with 0.01 E step (0.2V E_{pulse}) and time equilibrium at 5 sec (0.02 sec T_{pulse}), differential pulse.

4.3 Results and Discussion

4.3.1 Paper Substrates Interaction Observation

Figure 4.2 shows 1 mL of CNTs ink being dropped onto Whatman filter paper grade 1 (**Figure 4.2a**), premium glossy photo paper (**Figure 4.2b**), and matte photo paper (**Figure 4.2c**). This is to study the difference in the interaction between the CNTs ink and the paper substrates with different porosity, thickness, and roughness.

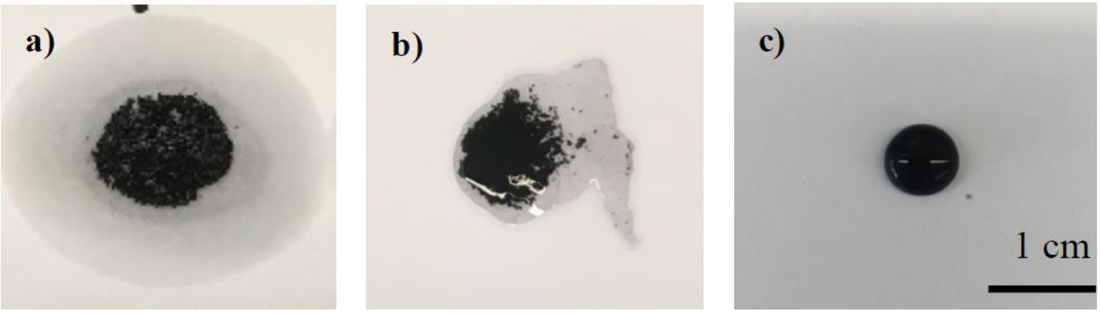

Figure 4.2: CNTs ink dropped on a) Whatman filter paper grade 1, b) premium glossy photo paper, and c) matte photo paper

Figure 4.2a shows the spreading and penetration of solvent on Whatman filter paper grade 1, leaving CNTs behind on the substrate surface. This is due to the porosity of the filter paper. **Figure 4.2b** illustrates a slightly different interaction where the CNTs ink remained on the substrate surface and the associated solvent. This is possibly due to the coating on the substrate surface. However, the solvent evaporates after a period, leaving the CNTs on the surface. Unlike matte photo paper, **Figure 4.2c**, the CNTs ink droplet was formed on the substrate surface, indicating the hydrophobic properties of the substrate surface or it is non-porous.

From the visual observation, it can be concluded that matte photo paper may not be compatible for CNTs inkjet printing, while filter paper and glossy photo paper are likely to provide better CNTs ink adsorption performance for electrode fabrication. Therefore, further investigation on these two substrates will be discussed later in the chapter.

4.3.2 Fabricated Paper-based Electrodes and Printing Observation

Since Whatman filter paper grade 1 and glossy photo paper provide a promising interaction towards the formulated CNTs ink, CNTs ink was printed onto the paper substrates for 50 printing cycles. This is to observe the printing accuracy and precision on different paper substrates and quantify the number of CNTs deposition. In addition, the formulated CNTs ink was also printed onto Whatman filter paper grade 3 as it has the same porosity but different thickness, to gain more understanding of the printing compatibility and accuracy.

Figure 4.3 shows the results of CNTs printing on Whatman filter paper grade 1 (**Figure 4.3a**), glossy photo paper (**Figure 4.3b**) for 20 – 50 printing cycles, and Whatman filter paper grade 3 (**Figure 4.3c**) for 50 printing cycles.

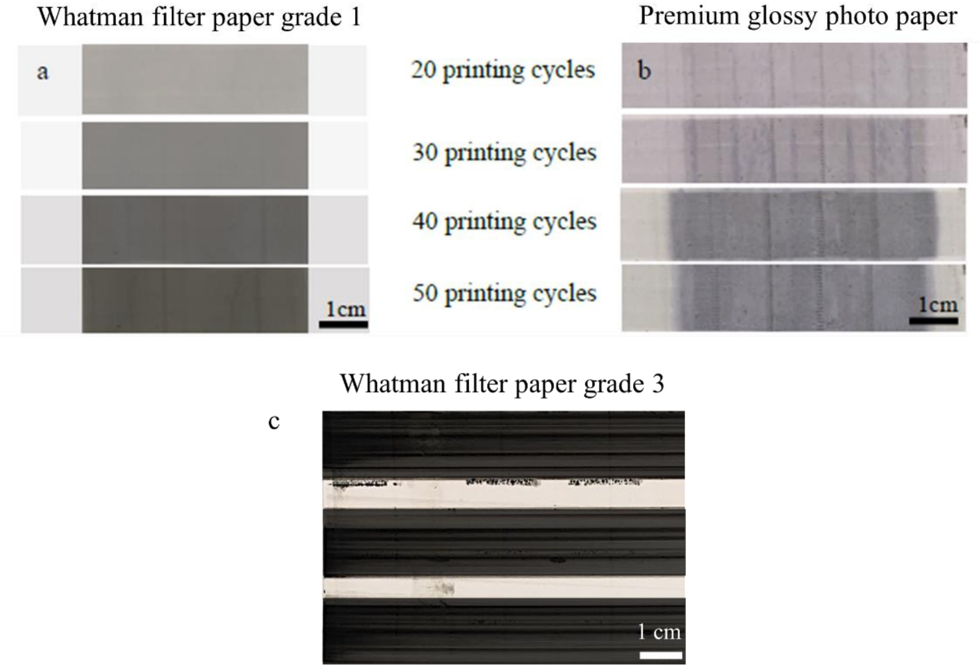

Figure 4.3: Formulated CNTs ink printed on a) Whatman filter paper grade 1, b) premium glossy paper at 20 – 50 printing cycles, and c) Whatman filter paper grade 3 printing repeats at 50 printing cycles.

As shown on **Figure 4.3**, the printing on filter papers is more accurate and precise with no spreading of the solvent outside the designated area, especially on Whatman filter paper grade 3. A much darker shade is obtained on Whatman filter paper grade 3 (**Figure 4.3c**) than on Whatman filter paper grade 1 (**Figure 4.3a**) and glossy photo paper (**Figure 4.3b**), at equivalent printing cycles, indicating more CNTs deposition on the substrate surface. The printing on the glossy photo paper (**Figure 4.3b**) is less accurate where the spreading of the formulated CNTs ink can be seen.

Figure 4.3a and c highlight the difference in CNTs deposition regardless of the same porosity. Denser CNTs deposition can be seen on Whatman filter paper grade 3, with less solvent spreading. This is an indication that the thickness of the paper substrate influences the printing efficiency.

4.3.3 SEM Characterisation

4.3.3.1 Fabricated CNTs Electrode Sensors

Figure 4.4 shows the fabricated CNTs electrode sensor on Whatman filter paper grade 1. The fabricated CNTs electrode sensor shows high CNTs deposition throughout the designated area with similar accuracy as on Whatman filter paper grade 1 (*section 3.3.2.2.2, Chapter 3*).

Figure 4.5 shows the SEM top-view morphology of the fabricated CNTs electrode sensors on Whatman filter paper grade 1 (**Figure 4.5a**), 3 (**Figure 4.5b**) and glossy photo paper (**Figure 4.5c**). This is to observe the CNTs distribution on the paper substrates. **Figure 4.6** shows the SEM image of untreated Whatman filter paper (**Figure 4.6a**) and glossy photo paper (**Figure 4.6b**).

Figure 4.4: Fabricated CNTs electrode sensor on Whatman filter paper grade 3

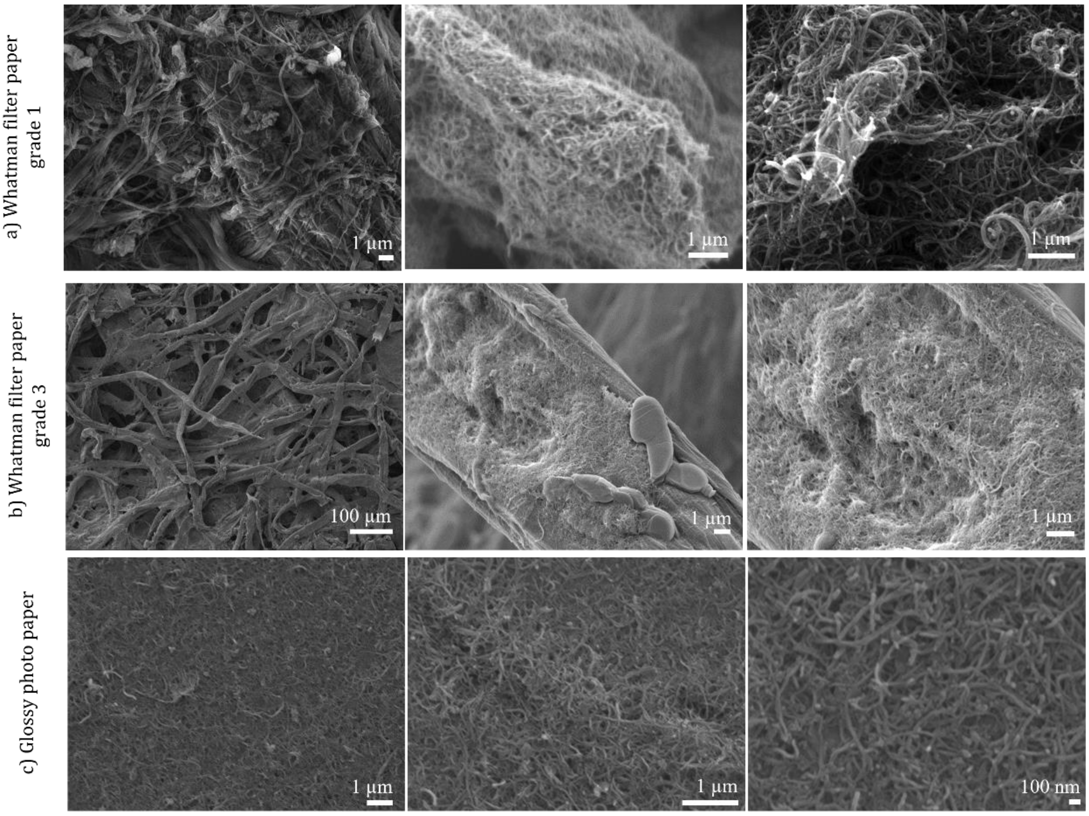

Figure 4.5: SEM top-view images of fabricated CNTs electrode sensors on a) Whatman filter paper grade 1, b) Whatman filter paper grade 3, and c) glossy photo paper

Figure 4.5 shows densely packed CNTs distribution on all paper substrates, with high connectivity. Similar CNTs distribution can be seen on Whatman filter paper grade 1 (**Figure 4.5a**) and 3 (**Figure 4.5b**) at approximately 105 ± 5.9 CNTs/μm^2 and 117.4 ± 4.6 CNT/μm^2, respectively. However, visually, as the printing continues, the spreading of the printed ink was observed on Whatman filter paper grade 1, which reduces the accuracy of the printing. Thus, a thicker paper substrate reduces the ink distribution spreading sideway.

Figure 4.5c shows a completely different CNTs distribution on glossy photo paper. CNTs remain on the surface of the paper substrate with high connectivity, especially across certain areas of the paper substrate. The number of CNTs deposition is approximately 90.5 ± 2.8 CNT/μm^2. This is due to the flow of the deposited CNTs ink towards the cracks. It is believed that this would be beneficial as the cracks can manually be created to control the arrangement of the CNTs.

4.3.3.2 Untreated Paper Substrates

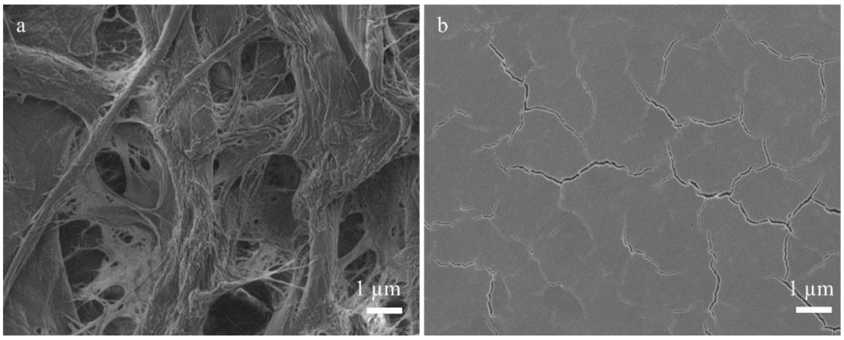

Figure 4.6: SEM top-view morphology of a) Whatman filter paper grade 3, and b) glossy photo paper

Figure 4.6 confirms the difference in surface morphology of Whatman filter paper and glossy photopaper, which affects CNTs distribution on each paper substrate. Whatman filter paper, **Figure 4.6a**, shows high porosity with random arrangement, explaining the behaviour of CNTs ink penetration in random orientations. While glossy photo paper, **Figure 4.6b**, shows a completely different surface characteristic, where the substrate shows a much smoother surface texture with some cracks. The cracks on the substrate surface explain the CNTs ink flow towards the cracks, causing certain areas to be more concentrated by the CNTs ink.

4.3.4 Resistance Measurement

Figure 4.7 shows the resistance of fabricated CNTs electrode sensor on Whatman filter paper grades 1 and 3 and glossy photo paper, with respect to the length between probes. The resistance gradually increases as the length between probes increases, theoretically expected, for all paper substrates. The relationship between the resistance and these variables is shown in **Equation 5**.

$$R = \rho \frac{l}{A} \qquad \text{(Equation 5)}$$

R = Resistance (ohm)

ρ = Specific resistivity (ohm · m)

l = Length (m)

A = Cross-sectional area (m^2)

As shown on **Figure 4.7**, CNTs electrode sensor on Whatman filter paper grades 1 and 3 shows similar resistance as the length between probes increases, with a specific resistivity of approximately 1.78 ± 0.11 kΩm and 2.85 ± 0.30 kΩm, respectively. Therefore, these two paper substrates are likely to provide similar sensing performance. However, in the case of glossy photo paper, much higher specific resistivity was measured, at approximately 8.60 ± 2.50 kΩm.

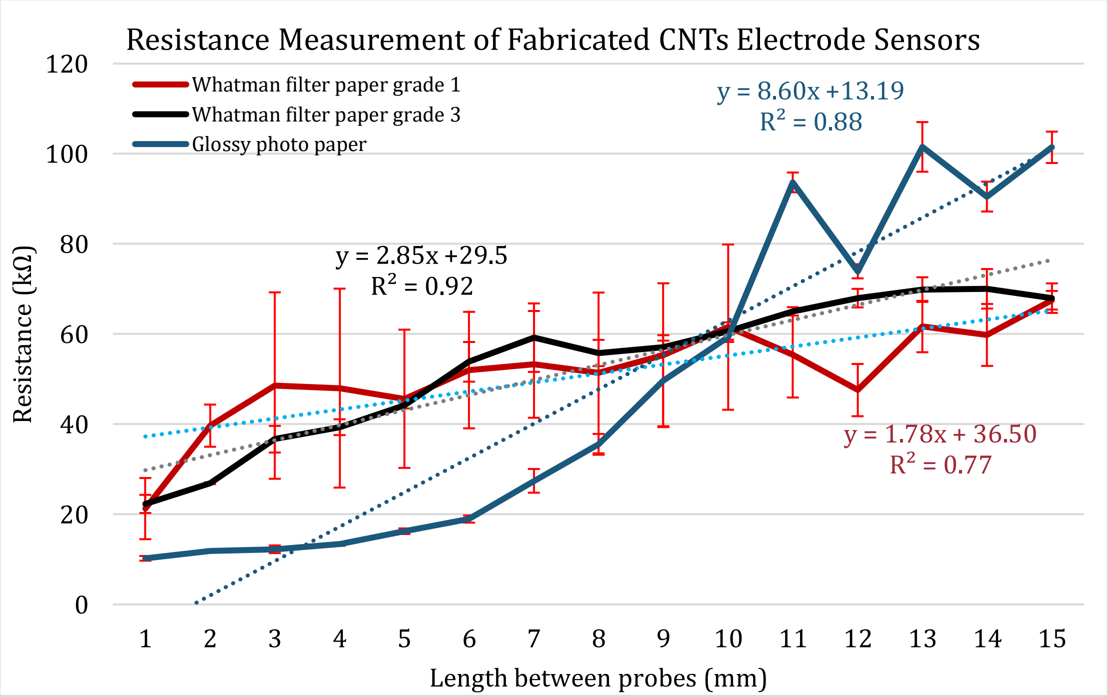

Figure 4.7: Resistance measurement of the fabricated CNTs electrode sensors on Whatman filter paper grade 1 and 3, and glossy photo paper

It can be concluded that Whatman filter paper would be more compatible for CNTs electrode sensors fabrication as it provides lower specific resistivity than glossy photo paper. However, due to the previous challenges on filter paper thickness and electrode sensor fabrication efficiency of Whatman filter paper grade 1, Whatman filter paper grade 3 would be more compatible for electrode sensors fabrication.

4.3.5 XPS Characterisation

4.3.5.1 Untreated Whatman Filter Paper Grades 1 and 3

Figure 4.8 shows the wide spectra and C1s spectra of Whatman filter paper grade 1 (**Figure 4.8a**) and 3 (**Figure 4.8b**). The intensities of the BE are used to calculate the atomic percentages (%) of each element, as summarised in **Table 4.1** and **Table 4.2**.

Whatman filter paper grades 1 (**Figure 4.8ai**) and 3 (**Figure 4.8bii**) show a similar composition of C and O contents at 64.4 % C and 35.6 % O, and 63.6% C and 36.4% O, respectively, as stated in **Table 4.1**. These values are in agreement with other studies, which state that the filter paper comprises over 98% cellulose, with approximately 60.4% carbon and 39.6% oxygen [199,200]. The C1s spectra of Whatman filter paper grades 1 (**Figure 4.8aii**) and 3 (**Figure 4.8bii**) compose of 9.4 % C-C/H, 73.0 % C-O and 17.6% O-C-O for Whatman filter paper grade 1, and 10.9% C-C/H, 70.1% C-O and 19.0% O-C-O for Whatman filter paper grade 3, at 285.0 eV, 286.8 eV, and 288.2 eV, respectively (**Table 4.2**). The C-C/H peak is a sign of possible contamination that may arise during sample handling. However, it is not significant for CNTs electrode sensors fabrication.

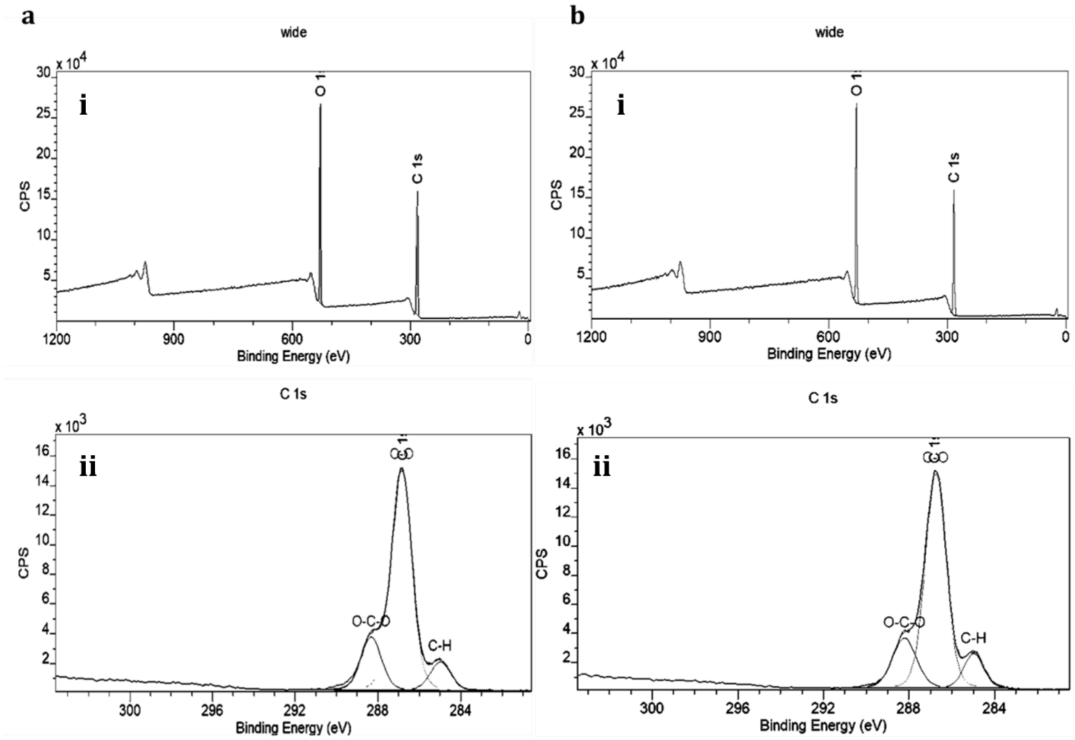

Figure 4.8: i) Wide spectra and ii) C1s spectra of untreated a) Whatman filter paper grade 1, and b) Whatman filter paper grade 3

Table 4.1: Atomic percentages of untreated Whatman filter paper grade 1 and 3

	C 1s	O 1s
Whatman filter paper grade 1	64.4 %	35.6 %
Whatman filter paper grade 3	63.6 %	36.4 %

Table 4.2: Percent composition of untreated Whatman filter paper grade 1 and 3

	C-C/H	C-O	O-C-O
BE (eV)	285.0	286.8	288.2
Whatman filter paper grade 1	9.4 %	73.0 %	17.6 %
Whatman filter paper grade 3	10.9 %	70.1 %	19.0 %

Compare the wide signal of Whatman filter paper grades 1 and 3 (**Figure 4.8**) to glossy photo paper (*Appendix B*); the wide spectra show differences in surface chemistry of the paper substrates. The glossy photo paper composes of 12.9 % C, 68.1 % O, 0.6 % N, and 18.4 % Si, which likely makes the surface characteristic more hydrophobic than filter paper, that mainly contains cellulose. This explains why the CNTs ink deposition is not as efficient as on the filter paper.

4.3.6 ASV Analysis

To observe the sensing performance, the fabricated CNTs electrode sensors on Whatman filter paper grade 3 were used as a WE to detect Cu^{2+} using ASV analysis. **Figure 4.9 and Figure 4.10** shows ASV analysis of Cu in acetate using fabricated CNTs electrode sensors on Whatman filter paper grade 3, at 5 sec and 10 sec to 120 sec (10 sec intervals) (**Figure 4.10**), and 5 sec deposition time, repeatedly for 3 times (**Figure 4.10**). Refer to *Appendix B* for standard ASV analysis using commercial WE.

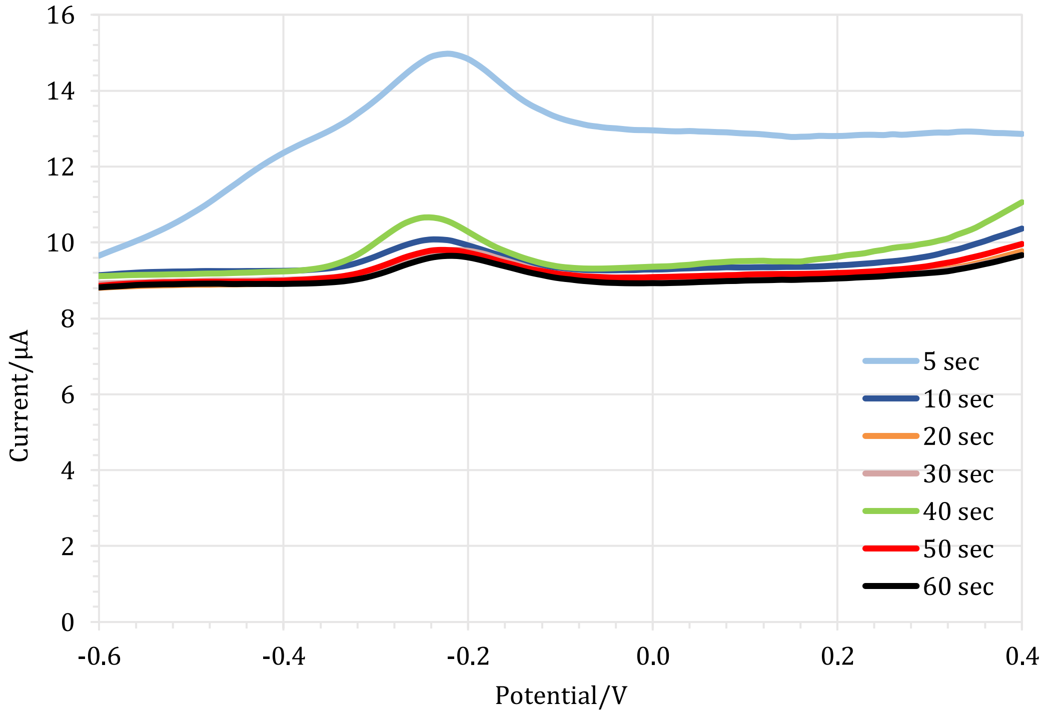

Figure 4.9: ASV analysis of fabricated CNTs electrode sensors on Whatman filter paper grade 3 at 5 sec to 60 sec deposition time (condition: 10 ppm Cu in acetate)

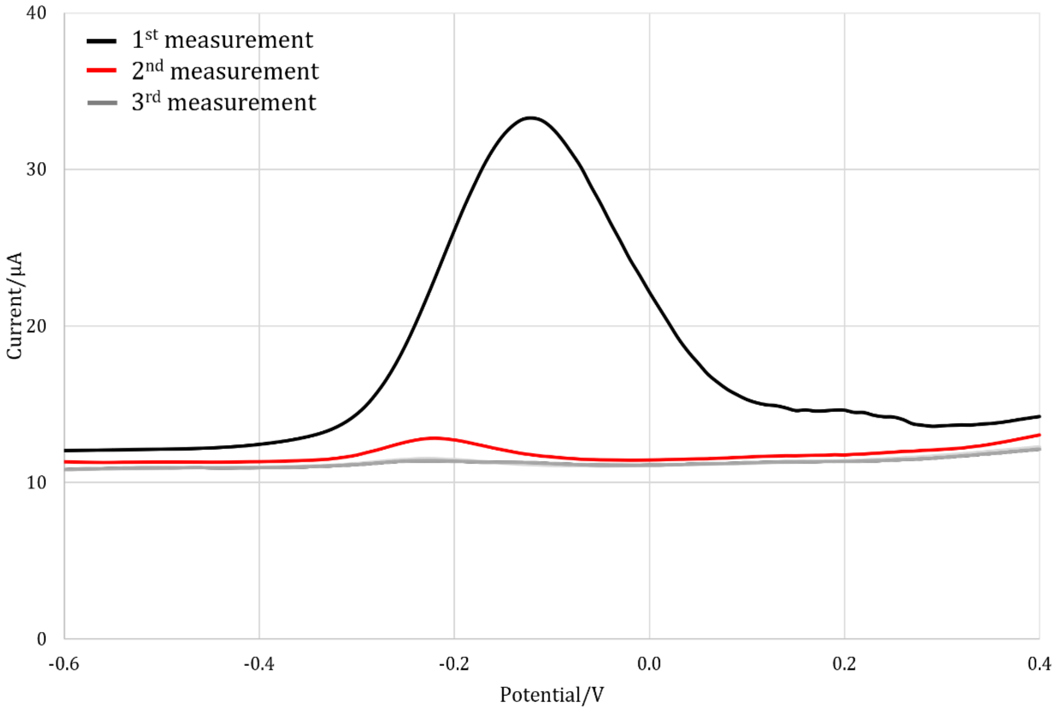

Figure 4.10: ASV analysis of fabricated CNTs electrode sensors on Whatman filter paper grade 3 at 5 sec deposition time (condition: 10 ppm Cu in acetate)

As shown in **Figure 4.9**, a clear peak can be seen only at 5 sec deposition time while other measurements, at different deposition times, remain low. It is likely that the fabricated CNTs electrode sensors are suitable for single use only. To confirm this statement, **Figure 4.10** shows the multiple ASV analysis at 5 sec deposition time, where only the first measurement shows a clear peak while the rest remained low. This confirms that the fabricated electrode sensors may suffered from poor durability and stability due to aqueous absorption and degradation. Therefore, further studies are required to overcome these challenges.

4.4 Conclusion

Different paper substrates, including Whatman filter paper grades 1 and 3, matte photo paper, and glossy photo paper, were studied to identify the most compatible paper substrate for CNTs ink deposition and electrode sensor fabrication using an inkjet printer. Visual observation, SEM, resistance measurement, XPS, and ASV analysis were utilised to assess the paper substrates compatibility.

Visually, matte photo paper showed hydrophobic surface characteristics towards CNTs ink, indicating incompatible behaviour with the water-based CNTs ink. While the CNTs ink penetrates through Whatman filter paper, leaving the CNTs on the material surface, showing high compatibility with the CNTs ink. Similar to glossy photo paper, the CNTs ink solvent partially penetrates the paper substrate at a slower rate.

SEM images showed high CNTs connectivity and distribution on the substrate surface for both Whatman filter papers and glossy photo paper, but in a different arrangement. In the case of Whatman filter paper, the CNTs deposited throughout the material surface homogeneously. Whereas on glossy photo paper, the CNTs are more concentrated on certain areas, especially at the cracks on the surface. The SEM images of bare substrates were characterised, confirming such behaviours are due to the surface characteristics where the filter paper is porous while glossy photo paper is smoother but contains cracks. Quantitatively, there are more CNTs deposition on Whatman filter paper (105 ± 5.9 CNTs/μm^2 and 117.4 ± 4.6 CNT/μm^2 for grades 1 and 3) than on glossy photo paper (90.5 ± 2.8 CNT/μm^2). Resistance measurement of the fabricated CNTs electrode sensors shows lower specific resistivity on filter paper at 1.78 ± 0.11 kΩm for Whatman filter paper grade 1 and 2.85 ± 0.30 kΩm for Whatman filter paper grades 3 than glossy photo paper (8.60 ± 2.50 kΩm).

XPS showed the composition of Whatman filter paper and glossy photo paper. Whatman filter paper composes mainly of cellulose with a composition of 64.4 % C and 35.6 % O (grade 1), and 63.6% C and 36.4% O (grade 3); therefore, the substrate is hydrophilic by nature and is more compatible with CNTs ink. While glossy photo paper contains multiple components, including Si, C, N, and O content. This likely induces the hydrophobicity of the substrate surface; therefore, it interacts with the CNTs ink differently.

ASV analysis for Cu^{2+} detection using fabricated CNTs electrode sensors on Whatman filter paper was conducted to observe the detection performance. The electrode sensor suffered from poor durability and stability due to aqueous absorption and degradation as it is appropriate for single use only. Therefore, the next chapter will examine possible techniques to enhance the paper substrate's durability and stability.

5 Plasma Polymerisation on Filter Paper to Enhance Electrode Sensor Performance and Stability Using PFC and AA

As shown in *Chapter 4*, the CNTs-based electrode sensor fabricated on a Whatman filter paper grade 3 suffered from poor durability and stability due to water absorption and filter paper degradation, making the electrode inappropriate for multiple uses. Therefore, the technique of PP will be utilised to overcome this issue, as discussed in this chapter.

5.1 Introduction

PP is a process wherein a plasma source is used to generate a gas discharge, which can polymerise a monomer (gas or liquid) onto the material surface to form thin films [153]. The main advantage of using PP is its ability to modify the surface characteristics of a substrate without modifying the bulk properties. PP is highly suitable as it is a clean, dry and solvent-free process that can coat a variety of shapes/geometries, including fibres and membranes. (Refer to *Chapter 2* for more details)

The methodology utilised to improve the performance and stability of CNTs-based electrode sensors on filter paper using PP has been summarised in **Figure 5.1**.

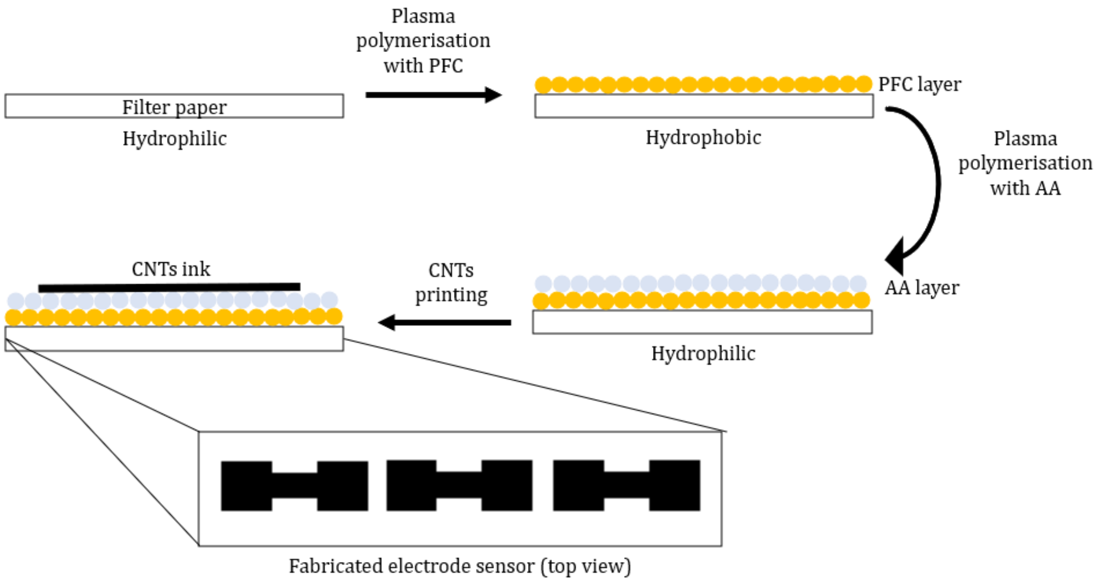

Figure 5.1: PP process of PFC and AA on Whatman filter paper grade 3

The first step was to improve the hydrophobic properties and stop water ingress into the Whatman filter paper to overcome the degradation in an aqueous environment. This was achieved by coating the filter paper with PFC via PP (**Figure 5.2a**). The PFC used in this work composes of fluorocarbon, where all hydrogens of a cyclobutane are replaced by fluorine (F). Fluorocarbons have been widely used to introduce hydrophobic properties to the material surface [201]. The second step was to induce hydrophilicity to the surface of PFC-coated filter paper for the water-based CNTs ink to be printed/deposited on the filter paper. To achieve this, AA (**Figure 5.2b**) was deposited onto the filter paper using PP. The advantage of using PP is that you can layer distinctly different chemistries. It would not be possible, for example, to cast a polymer AA on fluoropolymer from a solvent.

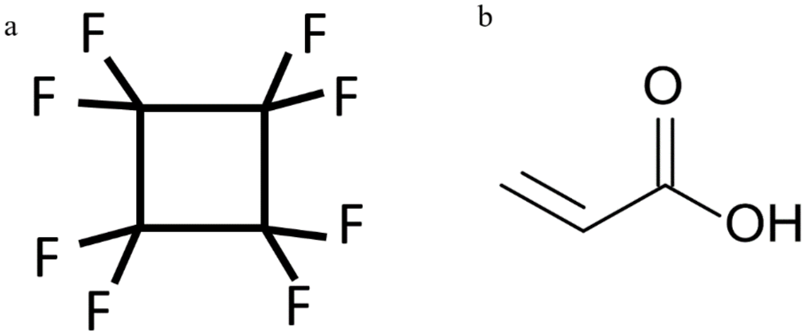

Figure 5.2: Structure of a) PFC and b) AA.

To assess the change in surface properties of plasma-treated Whatman filter paper, a range of analytical techniques were utilised:

1. Contact angle (CA) measurement (*section 5.2.4.5.1*)
2. XPS characterisation (*section 5.2.4.5.2*)
3. SEM characterisation (*section 5.2.4.5.3*)
4. Resistance measurement (*section 5.2.4.5.4*)

5.2 Experimental and Method

5.2.1 Material and Equipment

AA was purchased from Merck (CAS no.: 79-10-7). PFC was purchased from Apollo Scientific (CAS no.: 115-25-3). Whatman filter paper grade 3 was purchased from Sigma-Aldrich (CAS no.: 1003-917). The formulation of CNTs ink can be found in *Chapter 3*. The camera (40 – 1000x magnification) for the CA measurement was purchased from Juision Ltd. XPS was from Kratos Analytical, and SEM was from JEOL Ltd.

5.2.2 Plasma Polymerisation

The plasma reactor (**Figure 5.3**) was custom built using a glass barrel (500 mm length, 100 mm diameter) from De Dietrich Process Systems Ltd, Stafford, UK (part number 2PL10050330N000). The glass barrel was clamped between two custom-built stainless-steel plates, which served as two ground electrodes and attached to a bespoke stand with an integrated Faraday cage. Different monomers used separate glass barrels to avoid any contamination. The glass barrel also acted as a holder for the substrate (Whatman filter paper or silicon wafer (Si) wafer).

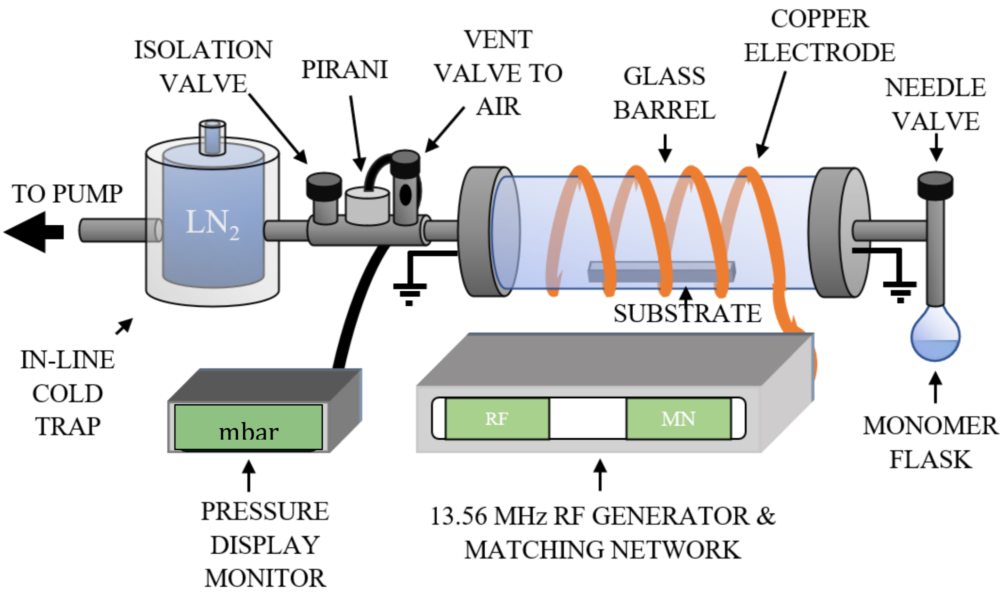

Figure 5.3: Plasma reactor

The vacuum system was maintained using an Edwards RV3 rotary vane pump (base pressure: 2 x 10-3 mbar). The pressure within the system was monitored by

Thermovac TTR 96N SC Pirani gauge and Display One Controller (Leybold UK Ltd, UK). An in-line liquid nitrogen cold trap was installed to enhance the system base pressure and prevent monomer vapours from reaching the rotary pump. Plasma was ignited using a RFG-C-100-13 power generator and automatic matching network (Coaxial Power System Ltd, Eastbourne, UK), operated at a frequency of 13.56MHz, connected to a 1 cm thick copper wire (Tranect Ltd, Liverpool, UK) wrapped around the glass barrel, three times.

For compressed gas monomers like PFC, the gas cylinder was connected to the glass barrel using a needle valve (Chell Instruments Ltd, North Walsham, UK). While for liquid monomer solutions like AA, a 5 mL aliquot of the monomer solution was added in a 50 mL round bottom flask (Scientific Laboratory Supplies Ltd, Z-10068) and connected to the barrel via a needle valve. Freeze-pump thaw degassing was carried out using liquid nitrogen.

Refer to *Chapter 2* for full details on plasma polymerisation.

5.2.3 CA Measurement

A custom-built system was constructed to obtain the CA measurement. The system consists of a camera (Jiusion 40 – 1000x magnification digital microscope), light and support, connected to the laptop, as shown in **Figure 5.4**. Refer to *Chapter 2* for full details on the CA measurement principle.

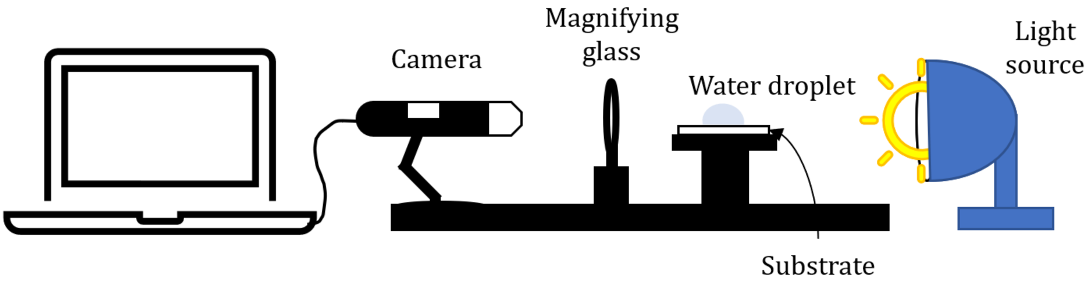

Figure 5.4: CA measurement system

.

5.2.4 Methodology

5.2.4.1 PP on Whatman Filter Paper Grade 3 and Si Wafer (PFC and AA Coating)

Prior to initiating the PP process, the glass barrel was thoroughly cleaned using isopropyl alcohol, acetone, and DI water to remove excess chemical residues. Prior to polymerisation using PFC and AA, an air plasma was operated at 60 W, 2x10^{-1} mbar for 10 min, to decontaminate the barrel. It should be noted that the different glass barrels and needle valves were used for each type of monomer to minimise potential cross-contamination.

5.2.4.2 PFC Plasma Coating

The glass barrel was pre-conditioned with PFC at 20 W, 2x10^{-1} mbar for 10 min. The filter paper/ Si wafer was placed inside the glass barrel, and a plasma polymer coating of PFC coating was conducted at 20 W, 2x10^{-1} mbar for 10 min.

5.2.4.3 AA Plasma Coating

Plasma polymer coating of AA was pre-conditioned under the following plasma operational parameters:

- 5 W, 2x10^{-1} mbar for 10, 15, 20 min
- 10 W, 2x10^{-1} mbar for 10, 15, 20 min
- 50 W, 2x10^{-1} mbar for 10, 15, 20 min

AA plasma polymerisation was performed on PFC-coated and untreated substrates, as per the parameters aforementioned.

5.2.4.4 CNT Inkjet Printing

The CNTs ink was printed on the AA-PFC filter paper using an Inkjet printer (CANON PIXMA TS205) for 50 printing cycles. After each cycle, the printing was left to dry for 2-3 minutes before the next printing.

5.2.4.5 Surface Characterisation

5.2.4.5.1 CA Measurement

10 µL of the aqueous solution (DI water and CNTs) was aliquoted using a pipette on the substrate (PFC-coated filter paper, AA-coated filter paper and AA-PFC filter paper). A photograph was taken using the camera, followed by measuring the CA between the substrate and DI water/CNTs ink using ImageJ software. Six CA measurements for each condition were conducted, and a standard error of the mean was calculated.

5.2.4.5.2 XPS Characterisation

The samples were attached onto XPS sample bars using clips. Survey (wide-scan spectra) and core line C1s, O1s and F1s spectra were recorded at pass energies of 160 eV and 20 eV for 160.00 sec and 120.00 sec, respectively. Samples were measured using a large area acquisition of 700 x 300 µm, an emission angle of 0° relative to the surface normal, and a power of 225 W (15 kV x 15 mA) using a monochromated Al Kα source. Three scans were performed for each sample per spectrum. The data were analysed using CasaXPS (ver.2.3.22PR 1.0, Casa Software Ltd). All spectra were calibrated by offsetting the BE according to the C-C chemical state of the C1s spectrum (285.0 eV). Peak fitting for core-line spectra was performed using expected chemical shifts from the literature [185,191]. (Refer to *section 3.2.2, Chapter 3* for full details)

5.2.4.5.3 SEM Characterisation

Untreated filter paper, PFC-coated filter paper, or AA-PFC filter paper was cut into 1 cm x 1cm pieces. The substrate morphology and cross-section were characterized at 1000x magnification (for surface morphology) and 250x magnification (for cross-section). ImageJ software was used to measure the filter paper thickness, and a standard of the mean was calculated.

5.2.4.5.4 Resistance Measurement

The fabricated CNTs electrode sensor on AA-PFC filter paper resistance was measured at 1 mm – 20 mm (1 mm interval) length between 2. Three measurements were conducted for each interval, and a standard of the mean was calculated.

5.3 Results and Discussion

5.3.1 Interaction Between Plasma Coated Filter Paper and Water Solution

Figure 5.5 shows the surface properties of plasma-polymerised filter paper in an aqueous environment (water solution). Untreated filter paper (**Figure 5.5a**), PFC-coated filter paper (**Figure 5.5b**), and AA-PFC filter paper (**Figure 5.5c**) were dropped in a beaker with DI water. **Figure 5.5d** shows the water droplets at five different spots on PFC-coated filter paper. At the same time, PFC-coated filter paper was left in the water solution for one month (**Figure 5.5e**).

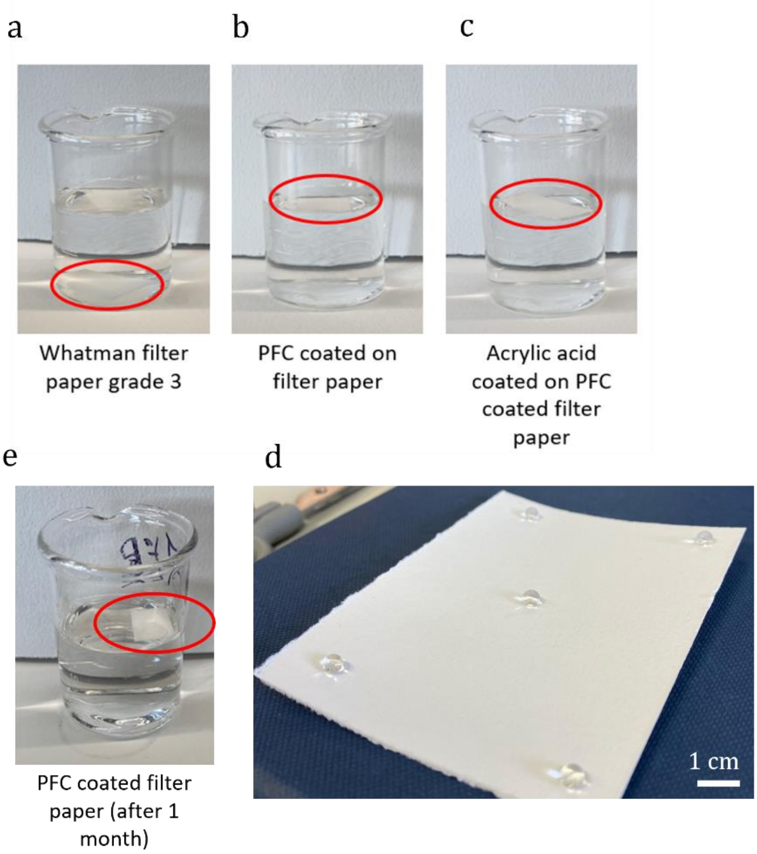

Figure 5.5: a) untreated filter paper, b) PFC-coated filter paper (20 W, $2x10^{-1}$ mbar for 10 min), c) AA-PFC filter paper (50 W, $2x10^{-1}$ mbar for 10 min) dropped in water solution, d) water dropped on PFC-coated filter paper, and e) PFC-coated filter paper in water solution after one month

As shown in **Figure 5.5a**, the untreated filter paper sunk to the bottom of the beaker, confirming the hydrophilic nature of the filter paper. This can be credited to the water absorbed by filter paper composed of cellulose. **Figure 5.5b** shows the PFC-coated filter paper floating on top of the water surface, indicating the hydrophobic properties induced by plasma coating on the filter paper. To confirm this, water was aliquoted on five different spots (four corners and in the middle) of PFC-coated filter paper, as shown in **Figure 5.5d**. It can be seen that water does not absorb into the PFC-coated filter paper in all five spots. This also highlights the uniform and homogenous coating achieved after PP. To assess the durability of the PFC-coating, PFC-coated filter paper was left in the water beaker for a month. **Figure 5.5e** shows the hydrophobic nature of PFC-coated filter paper remained unchanged after a month, highlighting the potential of PP to achieve a durable and highly- stable PFC coating on the filter paper.

Figure 5.5c shows that the AA-PFC filter paper was also floating on water but slightly submerged. This indicates that the filter paper does not absorb water and the durability of the PFC coating. Whether the AA layer is still present or soluble in the DI water cannot be determined.

5.3.2 CA Measurement

5.3.2.1 PFC Coating

Figure 5.6 shows the CA of untreated filter paper and PFC-coated filter paper with DI water and CNTs ink. As shown in **Figure 5.6a**, the untreated filter paper absorbed the DI water (**Figure 5.6ai**) and the CNTs ink (**Figure 5.6aii**) completely, resulting in a 0° CA. After PFC coating (**Figure 5.6b**), the CA increases to 120.59° ± 2.67 and 104.67° ± 1.24 for DI water (**Figure 5.6bi**) and CNTs ink (**Figure 5.6bii**), respectively. The photographs show droplet formation, thus confirming the presence of PFC coating on the filter paper at a reasonable thickness and preventing any water absorption. The CA with DI water was higher than that of CNTs ink. This difference can be credited to the lower surface tension of CNTs ink than DI water (*Appendix C*).

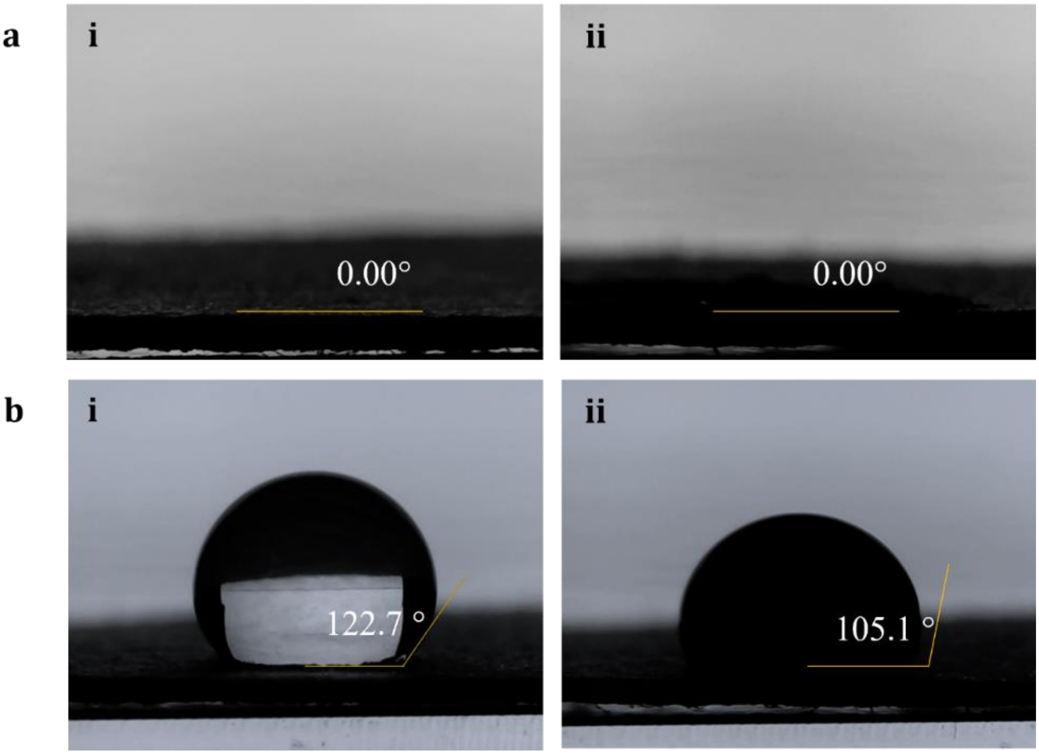

Figure 5.6: CA measurement of a) untreated filter paper and b) PFC coated filter paper (coating condition: 20 W, $2x10^{-1}$ mbar for 10 min) with i) DI water and ii) CNTs ink.

To understand how the roughness of the filter paper was affecting CAs, PP was performed on a Si wafer substrate. **Figure 5.7** shows the CA of the untreated silicon wafer and PFC-coated Si wafer with DI water/CNTs ink. The CA of an untreated Si wafer was 34.8° ± 1.24 with DI water (**Figure 5.7ai)** and 11.1° ± 4.54 with CNTs ink (**Figure 5.7aii**). After PFC coating, the CA increased to 97.40° ± 5.12 in the case of DI water (**Figure 5.7bi**) and 63.01 ° ± 1.61 in the case of CNTs ink (**Figure 5.7bii**). In comparing untreated (**Figure 5.7a**) with PFC-coated substrates (**Figure 5.7b**), it can be seen that the CA was higher for PFC-coated substrates. This highlights the plasma coating of PFC increases the hydrophobicity of both filter paper and Si wafer.

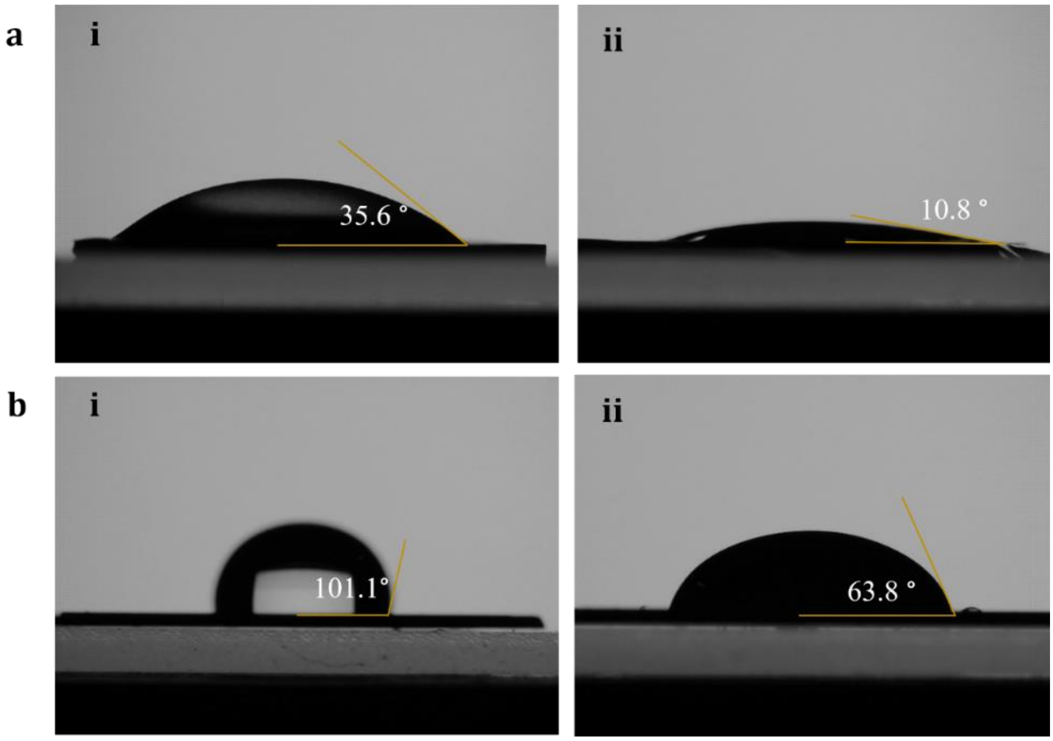

Figure 5.7: CA measurement of a) untreated Si wafer and b) PFC coated Si wafer (coating condition: 20 W, 2×10^{-1} mbar for 10 min) with i) DI water and ii) CNTs ink.

In a comparison of **Figures 5.10bii and 5.11bii**, it can be concluded that CNTs ink CA is lower than DI water for both filter paper and Si wafer due to lower surface tension. At the same time, there are lower CAs on filter paper than on Si wafer (DI water and CNTs ink) because of surface roughness. Since the filter paper is rough, more air is trapped in the material, causing higher water repellence and higher CA. These results confirm that the properties of a substrate (such as surface roughness) influence the quality (or extent) of hydrophobicity induced by PP.

5.3.2.2 AA Coating

Table 5.1 summarises the CA of AA-coated filter paper and AA-coated silicon wafer, with DI water and CNTs ink, at different power discharges (5 W and 50 W). As shown in the table, the CA of untreated and AA-coated filter paper at both power discharges was 0.00°. This is expected as AA does not impart the same hydrophobic property of PFC as discussed previously in *section 5.3.2.1*. Further, AA coating may not provide a barrier layer that prevents the absorption of water into the filter paper. As discussed later, the AA coating will be soluble in DI water and CNTs ink.

In the case of the Si wafer, the untreated Si wafer had a CA of 19.14 ° ± 1.77 and 11.1° ± 4.54 with DI water and CNTs ink, respectively. Upon PP, CA of AA-coated silicon wafer with DI water was 34.8° ± 1.24 and 55.44 ° ± 1.68, and with CNTs ink was 17.85° ± 1.68, and 25.36 ° ± 4.35 at 5W, and 50W, respectively. The DI water/ CNTs ink CAs on the Si wafer were significantly higher than that on filter paper, for both untreated and plasma-coated. This can be credited to the solid nature of the Si (i.e., no absorptive capacity).

The surface smoothness of the Si wafer allows further exploration of changes in CA. Unlike AA-filter paper, the AA-Si wafer showed an increase in CA with plasma coating and an increase in CA with an increase in the power in the plasma discharge. These results also indicate that the AA coating provides a contiguous coating and that whilst they may be partially soluble in DI water and CNTs ink, they are not entirely soluble. An increase in CA with AA -plasma coating indicates that at least some (if not all) coating is not soluble in DI and CNT ink. The increase in CA from 5w to 50W indicates that the latter is a more hydrophobic coating.

Table 5.1: CAs between DI water/CNTs ink and AA-coated substrates (filter paper and Si wafer) at 5 W and 50 W for 10 min

CA measurement	DI water	CNTs ink
Untreated filter paper	0.00 °	0.00 °
5 W AA-filter paper	0.00 °	0.00 °
50 W AA-filter paper	0.00 °	0.00 °
Untreated Si wafer	19.14° ± 1.77	11.1° ± 4.54
5 W AA-Si wafer	34.8° ± 1.24	17.85° ± 1.68
50 W AA-Si wafer	55.44° ± 1.68	25.36° ± 4.35

5.3.2.3 AA-PFC Coating

Table 5.2 summarises the CA of AA-coated filter paper and AA-PFC silicon wafer, with DI water and CNTs ink, at different power discharges (5 W and 50 W). Putting AA on PFC substrates lowers the CA, which is the objective to increase printability. As discussed previously in *section 5.3.2.1*, there is no water ingress into the filter paper after PFC-coating.

Table 5.2: CAs between DI water/CNTs ink and AA-PFC substrates (filter paper and Si wafer) at 5 W and 50 W for 10 min

CA measurement	DI water	CNTs ink
5 W AA-PFC filter paper	66.59° ± 8.04	41.45° ± 3.36
50 W AA-PFC filter paper	83.77° ± 5.0	42.32° ± 1.62
5 W AA-PFC Si wafer	33.7° ± 3.65	6.0° ± 0.76
50 W AA-PFC Si wafer	45.0° ± 4.10	23.1° ± 3.11

As shown in **Table 5.2**, the CA decreases upon AA-coating on both substrates (filter paper and Si wafer). In the case of DI water for 5 W and 50 W AA-PFC filter papers, the CA decreases from 120.59° ± 2.67 (PFC-coated filter paper) to 66.59° ± 8.04 (5W) and 83.77° ± 5.0 (50 W). The same trend applied to CNTs ink, where the CA decreases from 104.67° ± 1.24 (PFC-coated filter paper) to 41.45° ± 3.36 (5 W) and 42.32° ± 1.62 (50 W). The CA increases from 5 W to 50W for DI water, while there is no change in CNTs ink CA. In comparing AA-PFC filter paper with AA-PFC Si wafer, and AA-PFC Si wafer, **Table 5.2** shows the success of reducing CA for both DI water and CNTs ink. The CA decreases from 97.40° ± 5.12 (PFC-coated Si wafer) to 33.7 °± 3.65 and 45.0° ± 4.10 with DI water and from 63.01 ° ± 1.61 to 6.0° ± 0.76 and 23.1° ± 3.11 with CNTs ink for 5 W and 10 W AA-PFC Si wafers, respectively. The results on Si wafer for plasma power are consistent that higher power (50 W) furbishes a more hydrophobic contacting.

Without further data on the AA-PFC Si wafer on the coatings and interaction with DI water and CNTs ink, it is very challenging to draw a further conclusion on what may be behind these effects. In *section 5.3.4*, surface analysis is undertaken to provide further insight into these wetting experiments. It can be concluded that regardless of the difference in CA, the trend observed from both AA-PFC substrates shows the success of AA coating, especially at 5 W, as the lowest CA were observed.

5.3.3 SEM Characterization

As previously stated, the aim of PP is to modify the surface properties of the substrate without interfering with the bulk properties such as morphology. Therefore, the morphology of the substrate (filter paper) was assessed using the technique of SEM (**Figure 5.8**). **Figure 5.8** shows the morphology of the top view (**a,c,f**) and cross-section view (**b,d,e**) of untreated, PFC-coated and AA-PFC filter paper, respectively.

Comparing **Figure 5.8a** with **Figures 5.8c and e**, it can be seen that PFC and AA coating does not change the top morphology of the filter paper. Similarly, in the case of cross-section, the thickness of the filter paper remained within the same range at 250.39 ± 1.13 µm, 247.85 ± 2.59 µm and 247.25 ± 3.01 µm for untreated (**Figure 5.8b**), PFC-coated (**Figure 5.8d**), and AA-PFC (**Figure 5.8f**) filter paper, respectively. This indicates that PP does not change the bulk characteristic but only the material's surface properties.

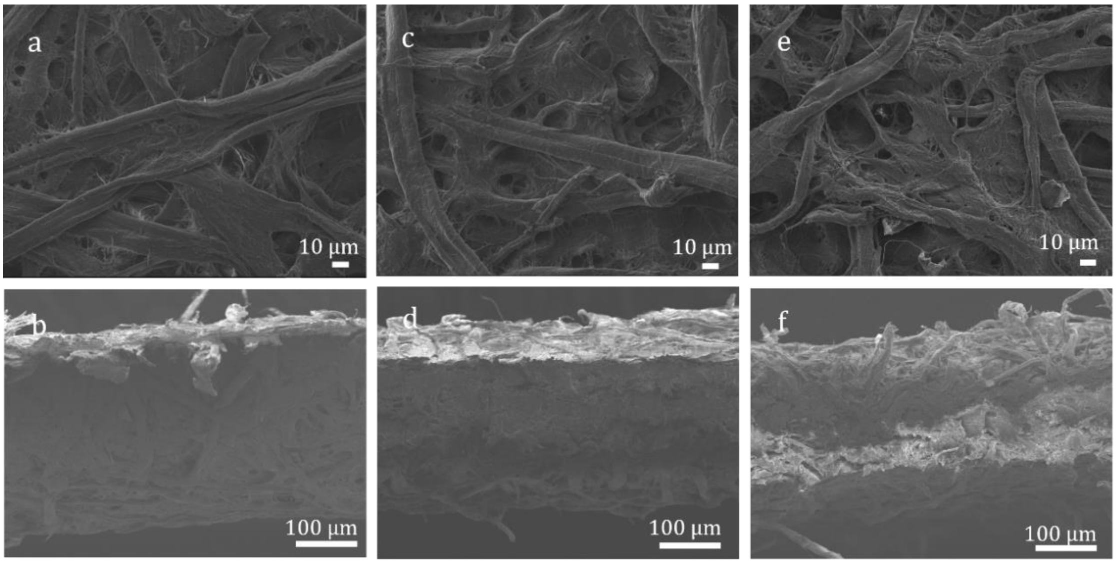

Figure 5.8: SEM images of untreated filter paper a) top view and b) cross-section, PFC-coated filter paper c) top view and d) cross-section and AA-PFC filter paper e) top view and f) cross-section

5.3.4 XPS Characterization

The behaviour seen in *section 5.3.2* on CA (DI water/ CNTs ink) is difficult to reconcile without further data on the plasma coating. To analyse the changes in the surface chemistry of the substrate after the PP technique, XPS characterisation was performed on PFC-coated (*section 5.3.4.1*), AA-PFC-coated (*section 5.3.4.2*), and CNT-printed on AA-PFC filter paper (*section 5.3.4.3*), as discussed below. (Refer to *Section 4.3.5.1, Chapter 4,* for untreated filter paper and *Appendix C* for untreated Si wafer XPS data)

5.3.4.1 Comparison between PFC-Coated Filter Paper and Si Wafer

Figure 5.9 and Figure 5.10 shows the wide spectra and C1s spectra of PFC-coated filter paper and PFC-coated Si wafer, respectively. The spectra consist of counts per second (cps) against the specific BE of the atom. The intensities of the BE are used to calculate the atomic percentages (%) of each element, as summarised in **Tables 5.3 - 5.6**.

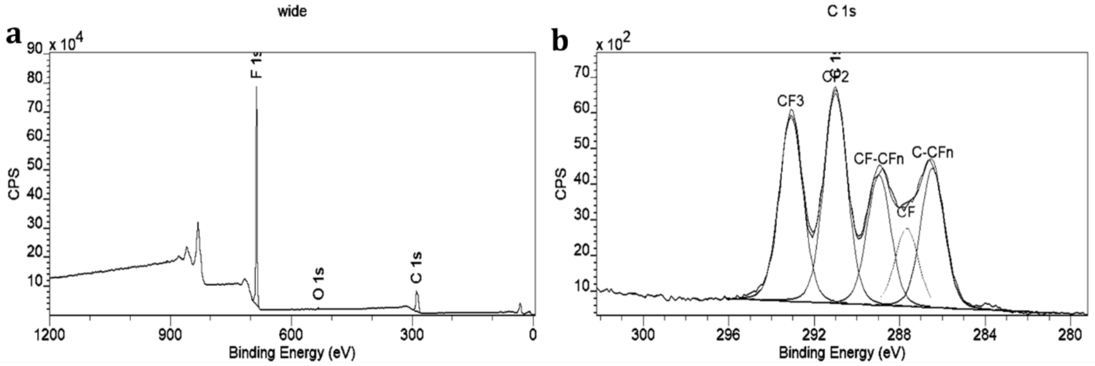

Figure 5.9: a) wide spectra and b) C1s spectra of PFC-coated filter paper at 20W for 10 min, 2 x 10^{-1} mbar

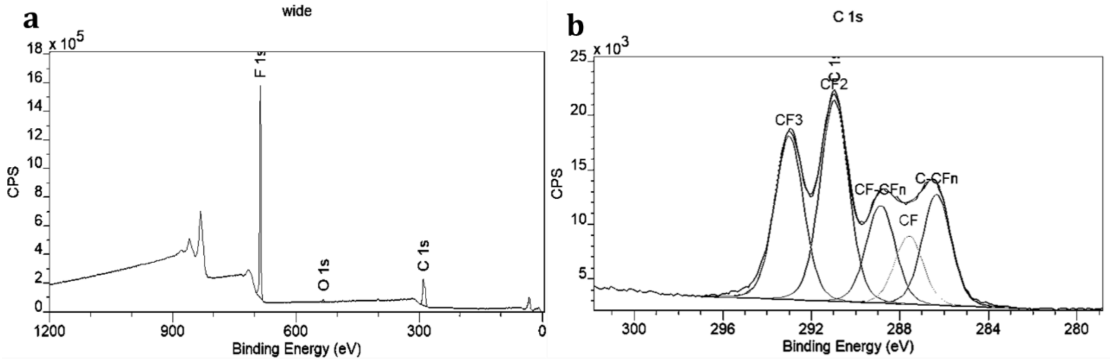

Figure 5.10: a) wide spectra and b) C1s spectra of PFC-coated Si wafer at 20W for 10 min, 2 x 10^{-1} mbar

As shown in the wide spectra of PFC-coated filter paper (**Figure 5.9a)**, PP using PFC introduces a peak for F at 686.00 eV. This confirmed that PFC is successfully coated onto the filter paper. In comparing **Figure 5.9** with untreated filter paper (*section 4.3.5, Chapter 4*), the results highlight the lack of O content and the changes in C1s spectra with the F signal upon PFC-coating. This indicates that the PFC coating layer is thicker than the XPS sampling depth.

The overall composition was calculated (**Table 5.3**) as 54.9 % F, 44.6 % C, and 0.5 % O. Moreover, upon PFC-coating, the O composition reduced from 36.4 % on untreated filter paper (*section 4.3.5.1, Chapter 4*) to 0.5 %. The C1s spectra in

Figure 5.9b shows the presence of C-CFn, CF, CF-CFn, CF2 and CF3 on PFC-coated filter paper at BE of 287.7 eV, 289.0 eV, 291.0 eV and 293.1 eV and at a composition of 18.7%, 10.6%, 17.6%, 28.3% and 24.8% at, respectively (**Table 5.5**).

To further investigate how PP impacts different types of substrates with varying surface properties, XPS analysis was performed on a PFC-coated Si wafer (**Figure 5.10)**. The wide spectra **(Figure 5.10a)** shows F content being introduced on a PFC-coated Si wafer at 686.00 eV. The overall composition was 51.7 %, 47.2 %, and 1.0 % for F, C and O respectively (**Table 5.4**). In comparing **Figure 5.10a** and **Table 5.4** to **Figure 5.9a** and **Table 5.3**, it can be observed that the F, C, and O composition of PFC-coated filter paper and PFC-coated Si wafer is very similar.

Figure 5.10b shows the C1s spectrum of the PFC-coated Si wafer. It can be seen that C-CFn, CF, CF-CFn, CF2 and CF3 were a presence on PFC-coated Si wafer at a composition of 17.3%, 10.6%, 15.2%, 31.6% and 25.5% (**Table 5.6**), which is similar to that of PFC layer on PFC-coated filter paper as summarised in **Figure 5.9b and Table 5.5**. These data all confirm that with very similar chemistry, PFC has been successfully coated on two types of substrates using PP.

Comparison between AA-Coated Filter Paper and Si Wafer

Table 5.3 summarises the composition of AA-coated filter paper at 5 W and 50 W power discharge. Overall, using corelines from the wide spectra, **Table 5.3** show higher C content than O for all discharge power. For the AA-coated filter paper, C content increased with the power discharge, whereas O content decreased when comparing 5 W to 50 W.

Table 5.4 summarises the composition of AA-coated Si wafer at 5 W and 50 W power discharge. C content also increased while O content decreased with power discharge.

Comparing **Table 5.3 and 5.4**, a similar trend was observed for both AA-coated filter paper and AA-coated Si wafer. Overall, AA-coated filter papers have higher C content and lower O content than AA-coated Si wafers. As shown in **Table 5.3**, C content increased from 78.7 % to 83.0 % in the case of 5 W and 50 W AA-coated filter paper, respectively. Similarly, AA-coated Si wafer C content increased from 74.0 % (5 W) to 81.6 % (50 W) (**Table 5.4**). The O content decreased as the power discharge increased, from 21.3 % to 17.0 % for AA-coated filter paper (**Table 5.3**) and 26.0 %, and 18.4 % for AA-coated Si wafer, at 5 W, and 50 W, respectively (**Table 5.4**). It can be concluded from **Tables 5.3 and 5.4** that there is a slightly different in AA-coating on filter paper and Si wafer. The possible explanations are that the coatings are thinner than the XPS sampling depth, so particularly in the case of AA-coated filter paper, the filter paper can still be seen, or the substrates are having some effects on the surface chemistry of the deposit.

Table 5.3: Atomic percentages of untreated filter paper, PFC-coated filter paper at 20 W for 10 min and AA-coated filter paper at 5 W and 50 W for 10 min, 2 x 10^{-1} mbar

	C 1s	O 1s	F 1s
Untreated filter paper	63.6 %	36.4 %	-
PFC-coated filter paper	44.6 %	0.5 %	54.9 %
5 W AA-coated filter paper	78.7 %	21.3 %	-
50 W AA-coated filter paper	83.0 %	17.0 %	-

Table 5.4: Atomic percentages of PFC-coated Si wafer at 20 W for 10 min and AA-coated silicon wafer at 5 W, and 50 W for 10 min, 2 x 10^{-1} mbar

	C 1s	O 1s	F 1s	Si 2p
Untreated Si wafer	11.6 %	21.5 %	-	66.9 %
PFC-coated Si wafer	47.2 %	1.0 %	51.7 %	-
5 W AA-coated Si wafer	74.0 %	26.0 %	-	-
50 W AA-coated Si wafer	81.6 %	18.4 %	-	-

Table 5.5 summarises the peak-fitting of the C1s spectra, providing chemical state composition for AA-coated filter paper at different power discharges (5 W and 50 W). While **Table 5.6** summarises the C1s spectra of AA-coated Si wafer at different power discharges. On both filter paper and Si wafer, the presence of carboxylic acid (O-C=O/COOH) peak confirms AA deposition on both substrates.

As shown in **Table 5.5**, O-C=O was introduced onto the paper substrate at 12.0% and 5.5% at 289.0 eV for 5 W and 50 W, respectively. A similar trend was observed on the AA-coated Si wafer, as shown in **Table 5.6**. O-C=O content decreased from 17.1% at 5 W to 6.4% at 50 W AA-coated Si wafer (**Table 5.6**).

By comparing **Table 5.5 and 5.6**, it can be seen that, at any given power discharge, lower percentages of O-C=O were observed on filter paper than on Si wafer. This could result from the coating thickness (i.e., coating thickness is lower than the XPS sampling depth) or that the substrate properties influence the nature of plasma deposition. As discussed earlier, one possibility is that AA likely penetrates the filter paper; a potential consequence of this could be a thinner overall deposit on the filter paper (confirmed by the Si wafer). However, based on the data available, it is not possible to determine which of these possibilities applies.

Nevertheless, what is clear from these data is that 5 W provides greater O-C=O retention than 50 W, with a COOH composition of 12.0% for filter paper (**Table 5.5**) and 17.1% for Si wafer (**Table 5.6**).

Table 5.5: Percent composition of untreated filter paper, PFC-coated filter paper at 20 W for 10 min and AA-coated filter paper at 5 W and 50 W for 10 min, 2 x 10^{-1} mbar

	C-C/H	C-O	C=O	O-C-O	O-C=O	C-CFn	CF	CF-CFn	CF2	CF3
BE (eV)	285.0	286.8	287.7	288.2	289.0	286.5	287.7	289.0	291.0	293.1
Untreated filter paper	10.9 %	70.1 %	-	19.0 %	-	-	-	-	-	-
PFC-coated filter paper	-	-	-	-	-	18.7 %	10.6 %	17.6 %	28.3 %	24.8 %
5 W AA-coated filter paper	70.2 %	12.0 %	5.8 %	-	12.0 %	-	-	-	-	-
50 W AA-coated filter paper	73.1 %	13.7 %	7.7 %	-	5.5 %	-	-	-	-	-

Table 5.6: Percent composition of PFC coated silicon wafer at 20 W for 10 min and AA-coated silicon wafer at 5 W, and 50 W for 10 min, 2 x 10^{-1} mbar

	C-C/H	C-O	C=O	O-C=O	C-CFn	CF	CF-CFn	CF2	CF3
BE (eV)	284.9	286.1	287.3	289.1	286.3	287.6	288.9	291.0	293.0
PFC-coated Si wafer	-	-	-	-	17.3 %	10.6 %	15.2 %	31.6 %	25.5 %
5 W AA-coated Si wafer	62.1 %	13.9 %	6.3 %	17.1 %	-	-	-	-	-
50 W AA-coated Si wafer	66.3 %	17.8 %	9.4 %	6.4 %	-	-	-	-	-

5.3.4.2 AA-PFC Filter Paper

Figure 5.11 shows the wide spectra (**ai, and bi**) and C1s spectra (**aii, and bii**) of 5 W, and 50 W AA-PFC filter papers, respectively. This was conducted to optimise the PP condition and identify the plasma-polymerised substrate most appropriate for electrode sensors fabrication.

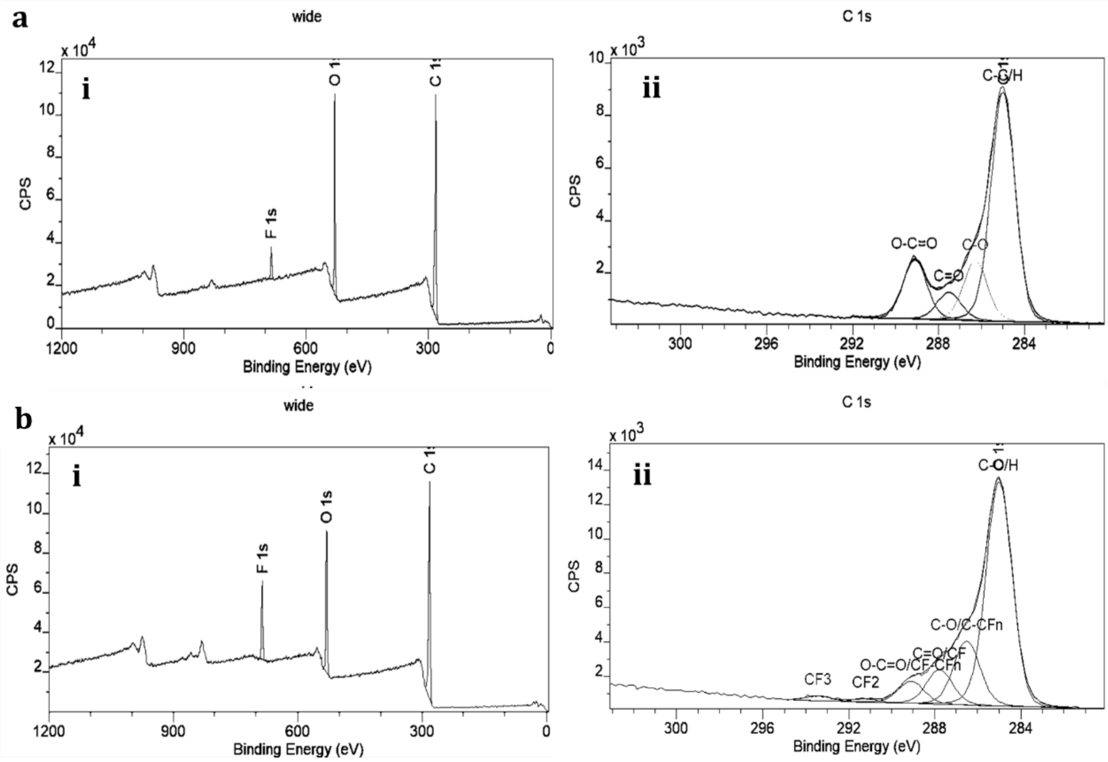

Figure 5.11: i) wide spectra and ii) C1s spectra of AA-PFC coated filter paper at a) 5 W, and b) 50 W for 10 min, 2 x 10^{-1} mbar

Figure 5.11 shows three major peaks: C, F and O in the case of all power as shown on the wide spectra. AA-PFC coated filter paper plasma-coated at 5 W, and 50 W consist of 75.4 % C, 22.0 % O and 2.6 % F, and 73.2 % C, 17.7 % O and 9.1 % F, respectively (**Table 5.7**). Upon AA-coating, F content decreases, and O content increases at all coating conditions compared to PFC-coated filter paper (*section 5.3.4.1*, **Table 5.3**), thus, confirming AA deposition, especially at 5 W. The AA coating imparts hydrophilic characteristics on the substrate surface for CNTs inkjet printing.

Figure 5.11 ai-bi also highlights that AA coatings do not mask all signals from the underlying PFC and the prominent increase in F content as the power discharge increased from 5W to 50 W. F content increased from 2.6 % (5 W) to 9.1 % (50W). This is possibly due to a thinner AA-coating than the XPS sampling depth for 50 W AA-coating (and that XPS can see through the AA layer to the underlying PFC) or the sputtering of F from PFC in AA-plasma. Nevertheless, CA data shows a sufficiently hydrophilic substrate surface to print onto.

Table 5.7: Atomic percentages of AA-PFC filter paper at 5 W, and 50 W for 10 min, 2 x 10^{-1} mbar

	C 1s	O 1s	F 1s
5 W AA-PFC filter paper	75.4 %	22.0 %	2.6 %
50 W AA-PFC filter paper	73.2 %	17.7 %	9.1 %

Figures 5.11 aii and **bii** shows the C1s spectra of 5 W and 50 W of AA-PFC filter papers, and the functional group composition was calculated and summarised in **Table 5.8**. **Table 5.8** shows a decrease in O-C=O (289.1 eV) composition as the power discharge increased, from 15.7% at 5 W to 6.3 % (combination of O-C=O and CF-CFn) at 50 W. Further, at 50 W, a signal from CF3 can be seen. This indicates that at 50 W, the AA-coating is either thinner than the XPS sampling depth, or there has been sputtering of PFC.

The XPS data help explain the CA behaviour of the plasma-polymerised filter paper since there is evidently a difference in AA-surface chemistry at 5 W and 50 W. The lower CA at 5W fits with greater retention of O-C=O (or conversely, the greater level of F in the 50W). Either way, from these observations, it can be concluded that 5 W power discharge is more likely to be more compatible for CNTs printing due to the greater wettability of 5W AA deposition and likely higher propensity for H-bonding with the CNTs through the higher density of O-C=O.

Table 5.8: Area percentages of acrylic acid coated on PFC filter paper at 5 W and 50 W for 10 min, 2 x 10^{-1} mbar

<table>
<tr><th></th><th>C-C/H</th><th>C-O</th><th>C-CFn</th><th>C=O</th><th>CF</th><th>O-C=O</th><th>CF-CFn</th><th>CF2</th><th>CF3</th></tr>
<tr><td>BE (eV)</td><td>285.0</td><td colspan="2">286.5</td><td colspan="2">287.5</td><td colspan="2">289.1</td><td>291.3</td><td>293.5</td></tr>
<tr><td>5 W AA-PFC filter paper</td><td>61.1 %</td><td>15.9 %</td><td>-</td><td>7.3 %</td><td>-</td><td>15.7 %</td><td>-</td><td>-</td><td>-</td></tr>
<tr><td>50 W AA-PFC filter paper</td><td>63.7 %</td><td colspan="2">18.1 %</td><td colspan="2">9.8 %</td><td colspan="2">6.3 %</td><td>0.9 %</td><td>1.3 %</td></tr>
</table>

5.3.4.3 CNTs Electrode Sensors on AA-PFC Filter Paper

Figure 5.12 shows the fabricated CNTs electrode sensors on untreated filter paper **(Figure 5.12a),** 5 W **(Figure 5.12b),** and 50 W **(Figure 5.12c)** AA-PFC filter paper. **Figure 5.12a** shows more CNTs deposition with higher accuracy and precision on untreated filter paper than on 5 W **(Figure 5.12b)** and 50 W **(Figure 5.12c)** AA-PFC filter paper. It is possible that the surface chemistry of AA-PFC filter papers has an effect on the CNTs printing performance.

Such printing inconsistency in the CNT electrode may disrupt the electron pathway and conductivity, especially on 50 W AA-PFC filter papers. To assess this, the resistance measurements were performed, as discussed in *section 5.3.4.3.2.*

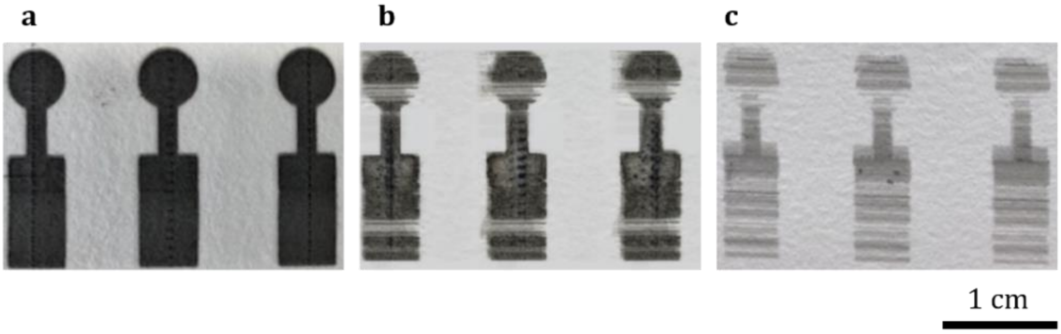

Figure 5.12: CNTs printed on a) untreated filter paper, b) 5 W AA-PFC filter paper and c) 50 W AA-PFC filter paper (AA coating condition: 5 10 min, 2 x 10 $^{-1}$ mbar)

5.3.4.3.1 XPS Characterisation of CNTs Electrode Sensor on AA-PFC Filter Paper

Figure 5.13 shows the wide spectra of fabricated CNTs electrode sensors on untreated filter paper (**Figure 5.13a**), 5 W (**Figure 5.13b**), and 50 W (**Figure 5.13c**) AA-PFC filter papers. **Table 5.9** summarises the composition of CNTs ink on untreated filter paper and CNTs electrode sensor on untreated filter paper, 5 W and 50 W AA-PFC filter papers. (Refer to *section 3.3.1.3.3, Chapter 3*, for a droplet of CNTs ink on untreated filter paper XPS data)p

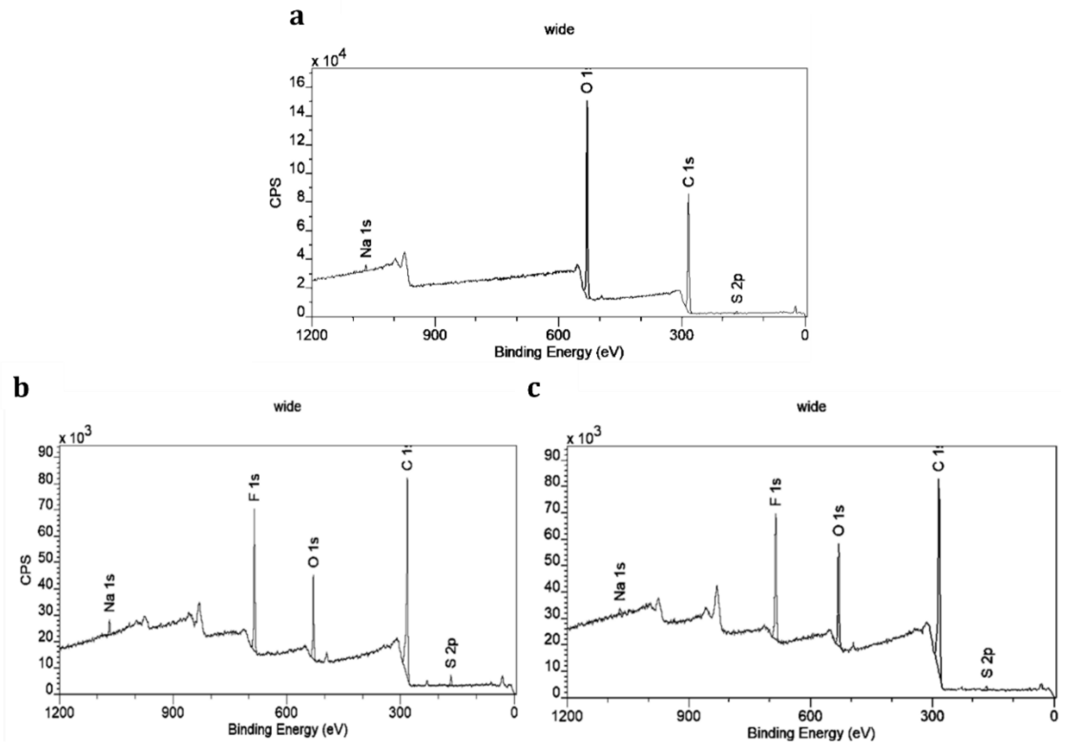

Figure 5.13: Wide spectra of CNTs printed on a) untreated filter paper, b) 5 W, and c) 50 W AA-PFC filter paper, 10 min, 2 x 10 $^{-1}$ mbar

Table 5.9: Atomic percentages of CNTs ink droplet on untreated filter paper and fabricated CNTs electrode sensors on untreated filter paper, 5 W and 50 W AA-PFC filter papers

	C 1s	O 1s	F 1s	S 2p	Na 1s
CNTs ink droplet on untreated filter paper	90.6 %	7.9 %	-	0.9 %	0.7 %
CNTs on untreated filter paper	65.4 %	33.8 %	-	0.4 %	0.4 %
CNTs on 5 W AA-PFC filter paper	75.8 %	10.6 %	11.5 %	1.5 %	0.5 %
CNTs on 50 W AA-PFC filter paper	78.1 %	10.5 %	10.5 %	0.7 %	0.2 %

Figure 5.13a shows the wide spectra of the CNTs electrode sensor on 5 W AA-PFC filter paper with a composition of 75.8 % C, 10.6 % O, 11.5 % F, 1.5 % S and 0.5 % Na, as summarised in **Table 5.9**. As shown in **Figure 5.13b**, the peaks for S and Na arise from SDS surfactant within the CNTs ink formulation. S and Na composition are higher on 5 W (1.5 % and 0.5 %) than on 50 W (0.7 % and 0.2 %) AA-PFC-coated filter paper, indicating more CNTs ink deposition at lower power discharge. However, the increase in F content on both substrates most likely

indicates that CNTs ink deposition dissolves the AA layer, causing the PFC layer to re-appear in the XPS. Despite this potential issue, the XPS data indicate that printing is likely to be more consistent on the 5 W AA-PFC filter paper than on 50 W AA, as the XPS reveals more CNTs ink deposition.

5.3.4.3.2 Resistance Measurement of CNTs Electrode Sensor on AA-PFC filter paper

Resistance measurement was conducted on fabricated CNTs electrode sensors on 5 W and 50 W AA-PFC filter papers; however, no signal can be measured on 50 W AA-PFC filter papers. **Figure 5.14** shows the resistance of the fabricated CNTs electrode sensors on untreated filter paper and 5 W AA-PFC filter papers with respect to the distance between the probes.

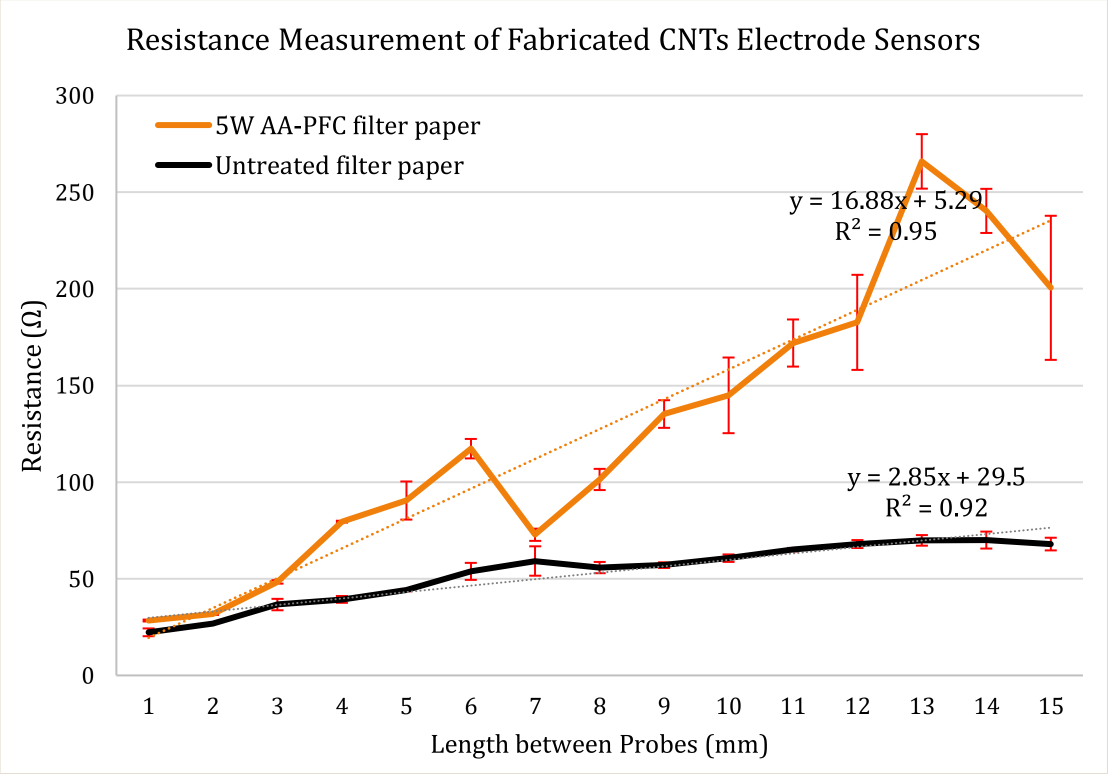

Figure 5.14: Resistance measurement of CNTs printed on 5 W AA-PFC filter paper and untreated filter paper

As shown in **Figure 5.14**, the resistance gradually increases as the length between probes increases, theoretically expected, in the case of both untreated and AA-PFC filter paper. However, the specific resistivity of 5 W AA-PFC-coated filter paper (16.88 ± 3.85 kΩm) is higher than CNTs printing on the untreated substrate (2.85 ± 0.30 kΩm). This confirms that the CNTs electrode fabricated on the plasma-coated filter paper is not as electrically conductive nor as accurate as the untreated filter paper. A further investigation is required to optimise the AA on PFC coating to improve CNTs deposition and printing accuracy. Different plasma will be investigated in the next chapter.

5.4 Conclusion

The technique of PP was utilised to coat PFC and AA on Whatman filter paper grade 3 to enhance the durability and stability of the CNT-based paper sensor in test sample solutions. Various analytical and characterisation techniques, including CA measurement, SEM, XPS and resistance measurements, were utilised to assess the effects of PP on the substrate.

After PFC coating, the CA increased from 0° to 120.59° ± 2.67 and 104.67 ° ± 1.24 for DI water and CNTs ink, respectively. This confirmed that plasma-coated PFC could induce hydrophobic characteristics in the filter paper and prevent absorption into the filter paper. XPS characterisation showed an increase in F content and a decrease in O content, confirming that PFC introduces hydrophobic characteristics onto the paper surface and repels an aqueous solution. SEM images show similar top-view morphology, cross-section and thickness (247.85 ± 2.59) as untreated filter paper (250.39 ± 1.13 µm), thus indicating the potential of PP to improve/modify surface properties without affecting the bulk properties such as morphology and thickness.

To allow the fabrication of water-based CNTs ink on a hydrophobic PFC-coated filter paper, AA was plasma polymerised onto PFC-coated filter paper. 5 W and 50 W power discharges at 10 min were tested to identify the most appropriate coating for CNTs ink printing. After AA coating, the CA reduced at all coating conditions, especially for the 5 W coating condition, where the CA reduced from 120.59° ± 2.67 and 104.67 ° ± 1.24 to 66.59° ± 8.04 and 41.45° ± 3.36 for DI water and CNTs ink, respectively. The XPS spectra of AA-PFC filter paper showed an increase in O content and a decrease in F content, confirming the presence of AA coating. XPS also revealed that at low power discharge of 5W, more carboxylate groups were introduced onto the substrate surface than at higher power. Therefore, a 5W power discharge was selected for AA-coating on PFC and printing CNTs. The XPS spectra of fabricated CNTs electrode sensors on AA-PFC filter paper at 5W showed the presence of S and Na peaks, confirming the presence of CNTs. However, an increase in F content (from the PFC layer) was observed, indicating that CNTs ink solubilises the AA layer and leads to uneven printing, which is the subject of future work. Nevertheless, the fabricated CNT-AA-PFA sensor was highly conductive with a specific resistivity of approximately 16.88 ± 0.99 kΩm.

It can be concluded that PFC and AA were successfully coated onto the filter paper. PFC enhanced the durability of the filter paper when immersed in DI water, lasting for up to a month, while the AA allows CNTs printing for electrode sensors fabrication. However, further studies and surface modification are required to improve the CNTs printing and electrode sensors fabrication efficiency. Therefore, the next chapter will examine other possible plasma polymers to compare the plasma coating efficiency and electrode sensors fabrication.

6 Plasma Polymerisation of AAm on PFC-Coated Filter Paper

As shown in *Chapter 5*, there were challenges in CNTs electrode sensors fabrication on AA-PFC-coated filter paper, including poor CNTs ink printability and the solubility of AA in CNTs ink. This is possibly due to the negative net charge of both the AA surface and the CNTs ink; therefore, PP of AAm are trialled in this chapter to overcome these challenges, with these PPs presenting amine/nitrogen functional groups.

6.1 Introduction

AAm ($C_3H_5NH_2$), **Figure 6.1**, an organic material, is a colourless to yellowish liquid [202]. The deposition of AAm can be seen visually through the colour changes on the paper substrate surface. AAm is a hydrophilic amine-functionalised polymer [203]; the principle reason for trialling AAm is that it could potentially impart NH_2 groups that would be available for protonation [204]. The working hypothesis is that the CNTs printing will be improved by the provision of amine (NH_2) groups. Therefore, it would be able to modify the PFC filter paper substrate surface and introduce hydrophilic characteristics to the substrate surface for CNTs printing and electrode sensor fabrication.

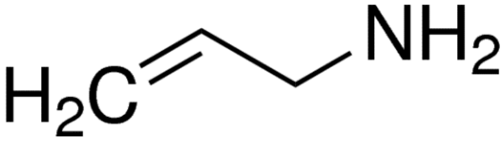

Figure 6.1: Chemical structure of allylamine [202]

Due to several factors, this research chooses AAm as an alternative plasma coating material. First, AAm provides hydrophilic properties, through the introduction of nitrogen functionality e.g. amine groups, to the paper substrate surface [205]. Therefore, through electrostatic interactions, the formulated CNTs ink should be printable onto the coated substrate. Second, plasma-coated AAm is mechanically and chemically stable in various aqueous solvents [166]. As a result, CNTs ink should be able to be deposited onto the paper substrate without dissolving the AAm coating layer.

In this chapter, AAm will be coated onto PFC-coated Whatman filter paper grade 3. The purpose of AAm coating is similar to what was conducted in *Chapter 5*. AAm coating on PFC filter paper will be compared with AA- PFC filter paper from *Chapter 5*. This is to gain more understanding of different plasma coatings for CNTs printing performance and their compatibility with CNTs electrode sensors fabrication. Once the most appropriate plasma coating material is identified, a high durability and stability paper-based sensor can successfully be fabricated for further detection.

To assess the change in surface properties of AAm-treated filter paper, the following techniques were utilised:

1. CA measurement (*section 6.2.2.3.1*)
2. XPS characterisation (refer to *section 6.2.2.3.2*)
3. Resistance measurement (refer to *section 6.2.2.3.3*)

6.2 Experimental and Method

6.2.1 Material and Equipment

AAm (purity ≥99%) (CAS no: 107-11-9) was purchased from Sigma-Aldrich. Other materials are the same as previously mentioned in *section 5.2.1, Chapter 5*.

6.2.2 Methodology

6.2.2.1 PP on Whatman Filter Paper Grade 3 (PFC and AAm)

For PFC plasma coating, please refer to *section 5.2.4.2, Chapter 5*

6.2.2.1.1 AAm Plasma Coating

AAm was pre-conditioned under the following plasma operational parameters:

- 5 W, 2x10^{-1} mbar for 10 min
- 20 W, 2x10^{-1} mbar for 10 min

AAm plasma polymerisation was performed on PFC-coated and untreated substrates, as per the parameters above.

6.2.2.2 CNTs Inkjet Printing

The CNTs ink was printed onto the AAm-PFC-coated filter paper for 50 printing cycles. After each cycle, the printing was left to dry for 2-3 minutes before the next printing.

6.2.2.3 Coated Filter Paper and CNT Electrode Sensor Observation and Characterization

6.2.2.3.1 CA Measurement

The CA between DI water and CNTs on AAm-PFC-coated filter paper under each plasma coating condition was measured. (Refer to *section 5.2.3, Chapter 5* for details)

6.2.2.3.2 XPS Characterisation

Survey (wide spectra), and C1s, N1s, O1s and F1s spectra of AAm-PFC-coated filter paper were recorded. (Refer to *section 3.2.2, Chapter 3* for details) Peak fitting for core-line spectra was performed using expected chemical shifts from the literature [185,191]. **Table 6.1** summarises the BE of the common chemical states in the C1s spectrum, which was used as a reference for surface chemistry identification.

Table 6.1: XPS reference table with C1s binding energy for allylamine [206–209]

Chemical state	**BE (eV)**
C-C/C-H	285.0
C-N	285.7 – 286.0
C-O/C=N/C≡N	286.5-286.7
C=O/O=C-N	287.9 -288.3

6.2.2.3.3 Resistance Measurement

The fabricated CNTs electrode sensor on AAm-PFC-coated filter paper resistance was measured. Three measurements were conducted for each interval, and a standard error of the mean was calculated. (Refer to *section* 3.2.3*, Chapter 3* for details)

6.3 Result and Discussion

6.3.1 CA Measurement

Table 6.2 shows the CA for DI water or CNTs ink on the AAm-PFC filter paper to observe the effects of varying power discharges (5 W and 20 W at 2 x 10 $^{-1}$ mbar for 10 min).

Table 6.2: CA measurement of AAm-PFC filter paper at different coating conditions with DI water and CNTs ink

	DI water	CNTs ink
PFC-coated filter paper	120.59° ± 2.67	104.67° ± 1.24
5 W AAm-PFC filter paper	18.59°± 1.90	14.89° ± 1.36
20 W AAm-PFC filter paper	40.32°± 2.34	34.70° ± 2.46

As shown in **table 6.2**, the CA decreases upon AAm-coating on PFC-coated filter paper. In the case of DI water for 5 W and 20 W AAm-PFC filter papers, the CA decreases from 120.59° ± 2.67 (PFC-coated filter paper, *section 5.3.2.1, Chapter 5*) to 18.59 °± 1.90 (5W) and 40.32 °± 2.34 (20 W). In the case of CNTs ink, the same trend applied; the CA decreases from 104.67° ± 1.24 (PFC-coated filter paper, *section 5.3.2.1, Chapter 5*) to 14.89 °± 1.36 (5 W) and 34.70 °± 2.46 (20 W).

Table 6.2 also highlights the increase in CA of DI water and CNTs ink as the power discharge of AAm-coating increases. In the case of CNTs ink, the CA increases between 5 W and 20 W. Generally, as the power discharge increases, based on previous research, it is reasonable to expect that the hydrophilic property of AAm reduces due to a reduction in the surface density of nitrogen functionalities and/or amine-functional groups and increased PP cross-linking [205].

By comparing **Table 5.2** from *section 5.3.2.3, Chapter 5*, with **Table 6.2**, it can be seen that, at a given plasma treatment time and power discharge, the CA of DI water was higher than CNTs ink for both AA-coating and AAm-coating. Nevertheless, the CA of AAm-PFC filter paper provides lower CA than AA-PFC filter paper for all power discharges, indicating (potentially) better compatibility with CNTs ink. This is possibly due to a more favourable electrostatic interaction between AAm and CNTs ink than AA and CNTs ink.

6.3.2 XPS Characterisation

6.3.2.1 AAm-PFC Filter paper

Figure 6.2 shows the wide spectra of 5 W and 10 W AAm-PFC filter paper. **Table 6.3** summarises the composition of AAm-PFC filter paper at each power discharge. **Figure 6.3** shows the C1s spectra of 5 W and 10 W AAm-PFC filter paper, and the composition was calculated and summarised in **Table 6.4**. This was conducted to optimise the PP condition and identify the plasma-polymerised filter paper that was most appropriate for electrode sensors fabrication.

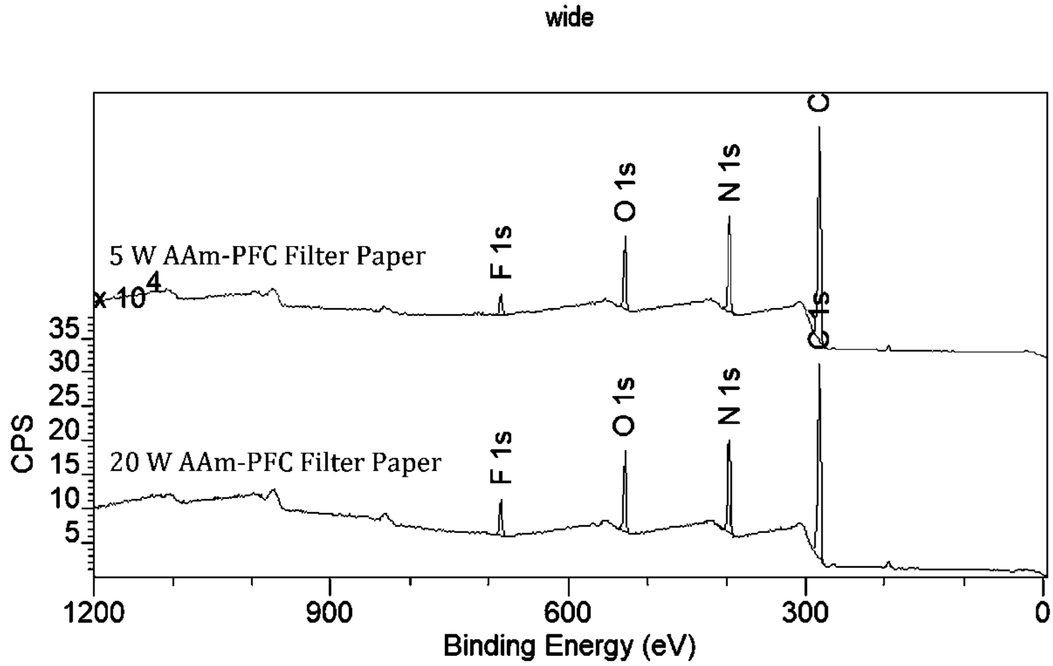

Figure 6.2: Wide spectra of AAm-PFC filter paper (5 W, and 20 W at 10 min, 2 x 10^{-1} mbar)

Table 6.3: Area percentages of AAm-PFC filter paper at 5 W, and 20 W (2 x 10^{-1} mbar, 10 min)

	C 1s	N 1s	O 1s	F 1s
5 W AAm-PFC filter paper	73.2 %	15.7 %	9.3 %	1.9 %
20 W AAm-PFC filter paper	70.6 %	16.1 %	10.3 %	3.0 %

Figure 6.2 shows four major peaks: C, N, O, and F in the case of all power as shown on the wide spectra. As shown in **Table 6.3**, the N signal represents a 15-16 % composition for both 5 W and 20 W, indicating a similar amount of N. The F signal is particularly interesting, which is higher in the 20 W, indicating either the AAm coating is thinner than the XPS sampling depth or sputtering of the PFC during the plasma process. **Figure 6.2** also highlights the introduction of O content, higher

than PFC-coated filter paper (0.5 % O). The O content arises from either residual H_2O and/or air in the AAm plasma and from post-plasma reactions with air [210].

Whilst F is seen in the wide scan, the fitting of the C1s (**Figure 6.3** and quantified in **Table 6.4)** reveals no distinguishable C-Fx functionalities in the 5 W AAm-PFC filter paper. However, in the case of 20 W AAm-PFC filter paper, the presence of C-Fx signals is clear at high binding energy in the C1s of the 20W AAm-PFC filter paper (**Figure 6.3**) with 0.6 % CF2 (291.5 eV) and 0.6 % CF3 (293.4 eV). A consequence of this is that other peaks fitted in the C1s of 20W may have contributions from both AAm and PFC, i.e., C-O/C=N/C≡N/C-CFn (286.7 eV), C=O/O=C-N/CF (287.9 eV), and CF-CFn/O-C=O (289.1 eV). Based on relatively low F (wide scan) and CF2 and CF3 signals, the contributions from C-CFn, CF and CF-CFn are likely to be relatively minor.

Figure 6.3 and Table 6.4 also highlights that the C-N component in 5 W and 20 W AAm-PFC filter paper is relatively constant at 15-16 %, indicating that total amine surface density in the PPs is high and equal in both PPs.

Figure 6.4 and Table 6.5 show the N1s spectra of 5 W and 20 W AAm-PFC filter paper. The fitting indicates a relatively similar N-C, N=C, and NCO composition on both 5 W and 20 W AAm-PFC filter paper. From the N1s spectra of both power discharges, there are likely to be amines on the substrate surface from PP of AAm. Nevertheless, with more F and higher CA on 20 W AAm-PFC filter paper, 5 W AAm-PFC filter paper may likely be more appropriate for CNTs printing and electrode sensor fabrication.

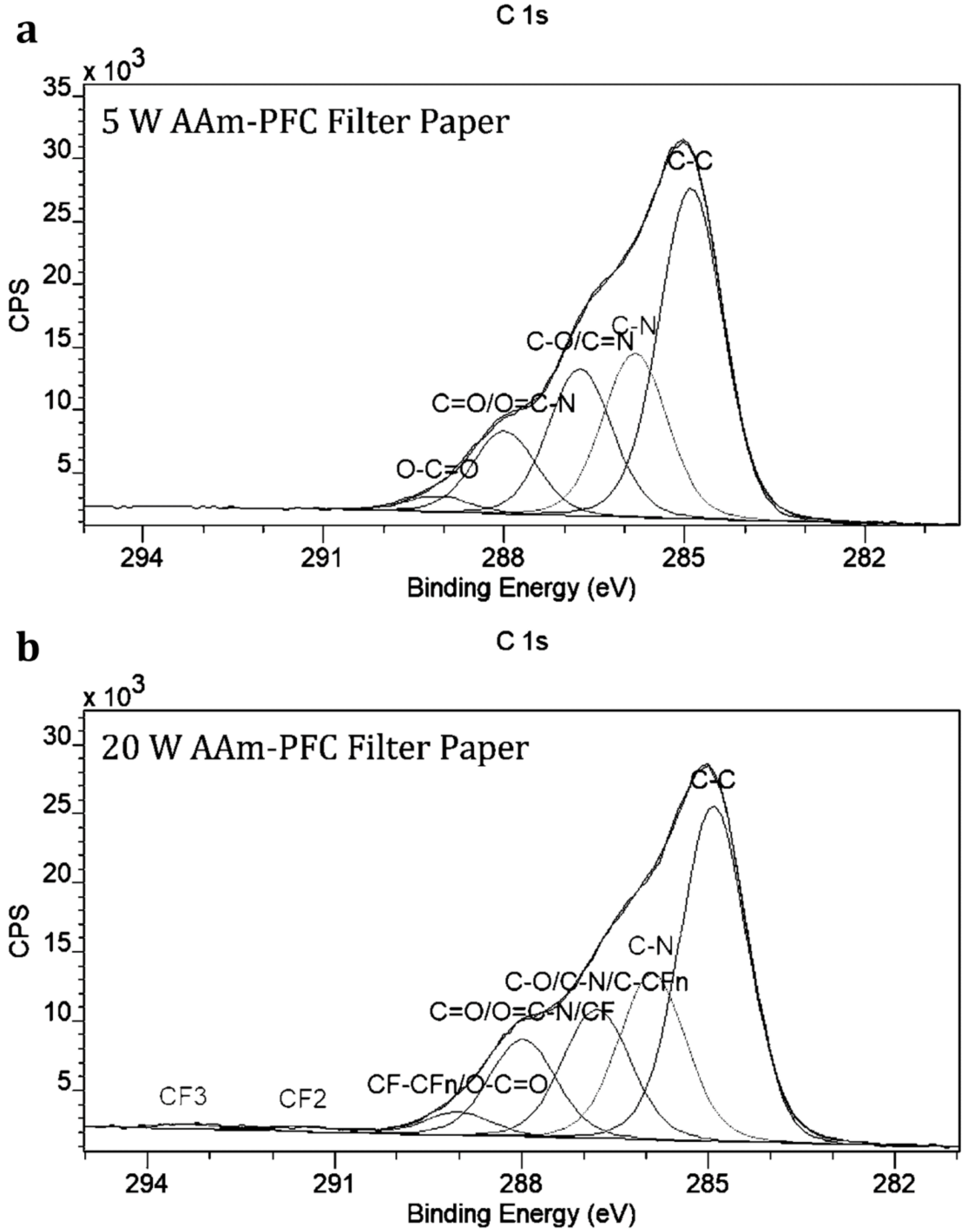

Figure 6.3: C1s spectra of a) 5 W and b) 20 W AAm-PFC filter paper (10 min, 2 x 10 $^{-1}$ mbar)

Table 6.4: Atomic percentages of AAm-PFC filter paper at 5 W, 10 W, and 20 W (2 x 10^{-1} mbar, 10 min)

	C-C	C-N	C-O/C=N/ C≡N	C-CFn	C=O/O=C-N	CF	CF-CFn	O-C=O	CF2	CF3
BE (eV)	284.9	285.8	286.7		287.9		289.1		291.5	293.4
5 W AAm-PFC filter paper	44.7 %	22.1 %	19.9 %	-	11.1 %	-	-	2.1 %	-	-
20 W AAm-PFC filter paper	44.1 %	21.8 %	17.1 %		12.8 %		3.0 %		0.6 %	0.6 %

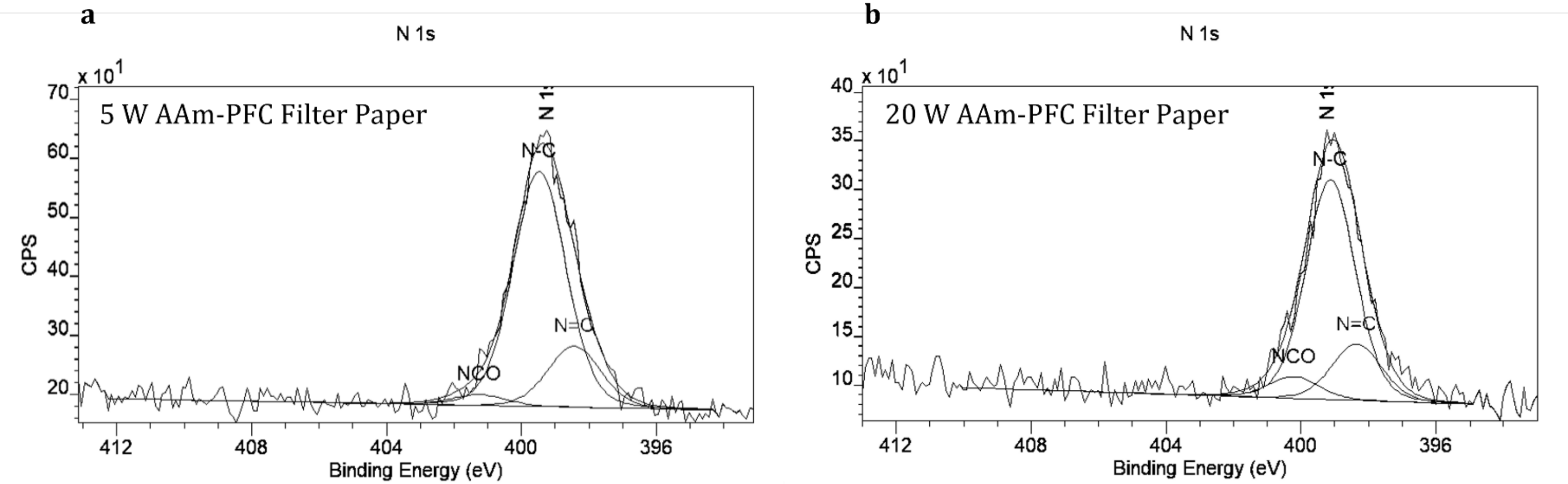

Figure 6.4: N1s spectra of AAm-PFC filter paper at 5 W, 10 W, and 20 W (2 x 10^{-1} mbar, 10 min)

Table 6.5: N1s spectra atomic percentages of AAm-PFC filter paper at 5 W, 10 W, and 20 W (2 x 10^{-1} mbar, 10 min)

	N=C	N-C	NCO
BE (eV)	398.4	399.5	401.3
5 W AAm-PFC filter paper	19.8 %	76.7 %	3.5 %
20 W AAm-PFC filter paper	18.8 %	74.0 %	7.2 %

6.3.2.2 CNTs Electrode Sensors on AAm-PFC Filter Paper

XPS was undertaken for CNTs ink printed onto Aam-PFC filter paper. **Figure 6.5 and Figure 6.6** shows the wide spectra (**Figure 6.5**) and the C1s spectra (**Figure 6.6**) of fabricated CNTs electrode sensors on 5 W and 20 W AAm-PFC filter paper (10 min, 2 x 10 $^{-1}$ mbar). **Table 6.6 and 6.7** summarises the elemental and chemical state composition of CNTs electrode sensors on 5 W and 20 W AAm-PFC filter papers.

In comparison to the XPS of CNTs ink (*section 3.3.1.3.3, Chapter 3*), the N1s and F1s signals (**Figure 6.5**) indicate that the C1s of CNTs on AAm-PFC filter paper (**Figure 6.6**) is a sampling of both CNTs ink and underlying PP since there is no F1s and N1s signal in the CNTs ink. The C1s spectra of CNTs on AAm-PFC filter paper was fitted according to the C=C: π-π* ratio (4.5:1) of the CNTs ink (**Figure 3.8**, section *3.3.1.3.3, Chapter 3)* in order to investigate CNTs deposition on AAm-PFC filter paper.

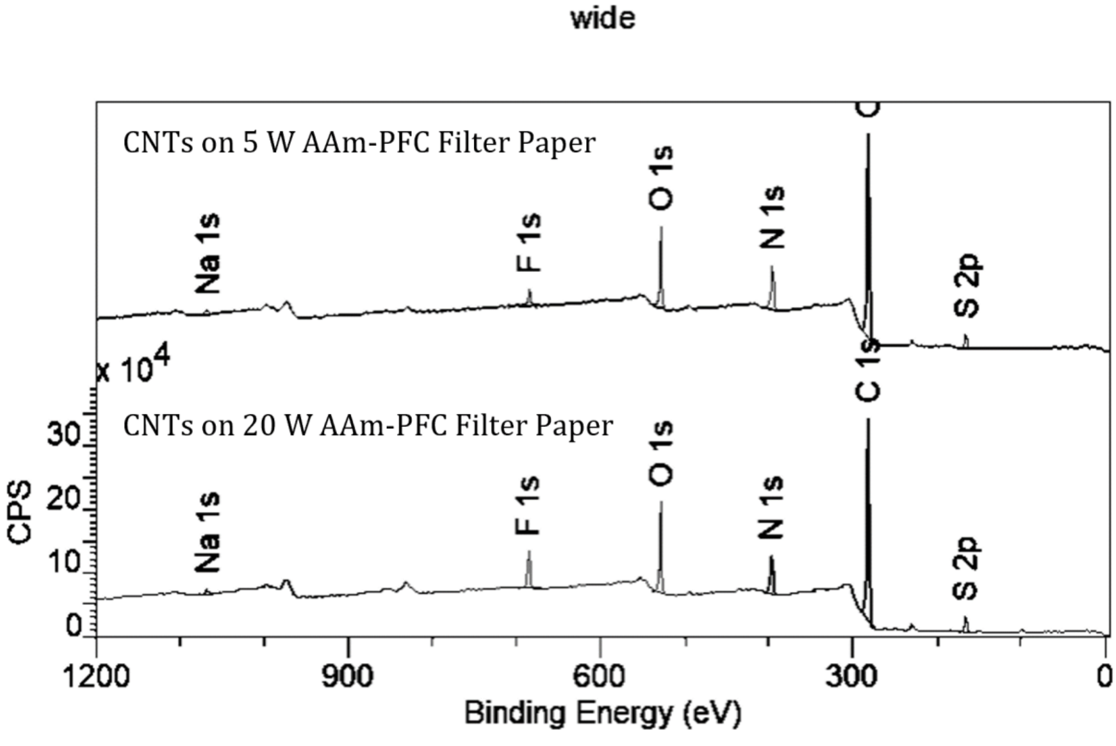

Figure 6.5: Wide spectra of CNTs on AAm-PFC filter paper at 5 W, and 20 W, 2 x 10^{-1} mbar, 10 min.

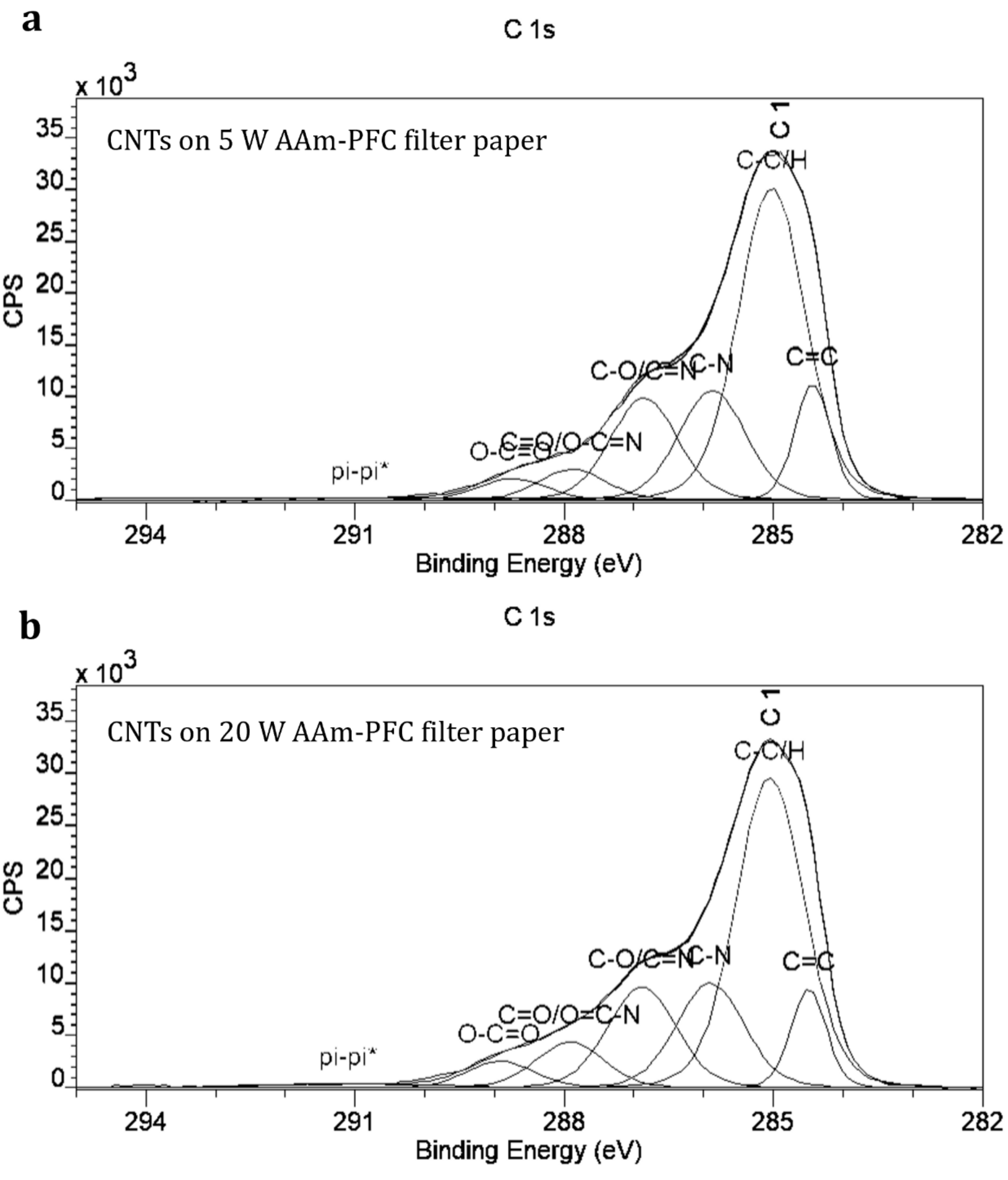

Figure 6.6: C1s spectra of CNTs on AAm-PFC filter paper at a) 5 W, and b) 20 W, 2 x 10^{-1} mbar, 10 min

Figure 6.5 and Figure 6.6 show that S and Na and π-π* content were introduced after CNTs printing. S and Na are unique to the formulated CNTs ink (not seen in AAm PP) and there is no π-π* signal seen on AAm PPs. Consequently, seeing π-π* and C=C signals on C1s spectra (which also not seen in the C1s of AAm-PFC filter paper) indicates presence of CNTs ink on the substrate surface.

Figure 6.5 and Table 6.6 show no significant different in S 2p and Na 1s signals, at a composition of 2.4 % and 0.3 % for 5 W, and 2.5% and 0.2 % for 20 W, respectively. This indicates that the CNTs deposition is similar.

Figure 6.6 and Table 6.7 highlight slightly higher C=C and π-π* content on 5W AAm-PFC filter paper (**Figure 6.6a**) than on 20W AAm-PFC filter paper (**Figure 6.6b**), at a composition of 9.5 % C=C and 2.1 % π-π* for 5 W and 7.8 % C=C (284.5 eV) and 1.7% π-π* (291.0 eV) for 20 W. This confirms the CNTs deposition on both AAm-PFC filter papers.

In comparison to the CNTs electrode sensor on AA-PFC filter paper (**Figure 5.12b and Table 5.9,** *section 5.3.4.3.1 Chapter 5*), the CNTs electrode sensor on AA-PFC filter paper is composed of higher F content (11.5 %) than on AAm-PFC filter paper (2.0 %) (**Figure 6.5 and Table 6.6**), at equivalent PP condition of 5 W power discharge. This is because, as mentioned in the previous chapter, the CNTs ink possibly dissolves the AA layer. Therefore, this indicates that AAm-PFC filter paper provides a more stable surface than AA-PFC filter paper, on which to print the CNTs.

Table 6.6: Atomic percentages of fabricated CNTs electrode sensor on AAm-PFC filter paper at 5 W, and 20 W (2 x 10^{-1} mbar, 10 min) [1]

	C 1s	N 1s	O 1s	F 1s	S 2p	Na 1s
CNTs on 5 W AAm-PFC filter paper	75.8 %	8.4 %	11.2 %	2.0 %	2.4 %	0.3 %
CNTs on 20 W AAm-PFC filter paper	74.0 %	7.6 %	12.3 %	3.3 %	2.5 %	0.2 %

Table 6.7: Area percentages of fabricated CNTs electrode sensor on AAm-PFC filter paper at 5 W, and 20 W (2 x 10^{-1} mbar, 10 min)

	C=C	C-C/H	C-N	C-O/ C=N/ C≡N	C=O/ O=C-N	O-C=O	π – π*
BE (eV)	284.5	285.0	285.8	286.8	287.9	288.9	291.0
CNTs on 5 W AAm-PFC filter paper	9.5 %	48.1 %	16.7 %	15.6 %	4.7 %	3.3 %	2.1 %
CNTs on 20 W AAm-PFC filter paper	7.8 %	47.8 %	16.1 %	15.5 %	7.0 %	4.1 %	1.7 %

---

[1] S and Na are markers of CNTs ink

6.3.2.3 CNTs Electrode Sensors Fabrication on AAm-PFC Filter Paper

Figure 6.7 shows the images of CNTs electrode sensor on 5 W (**figure 6.7a**), and 20 W (**figure 6.7b**) AAm-PFC filter paper (10 min, 2 x 10 $^{-1}$ mbar).

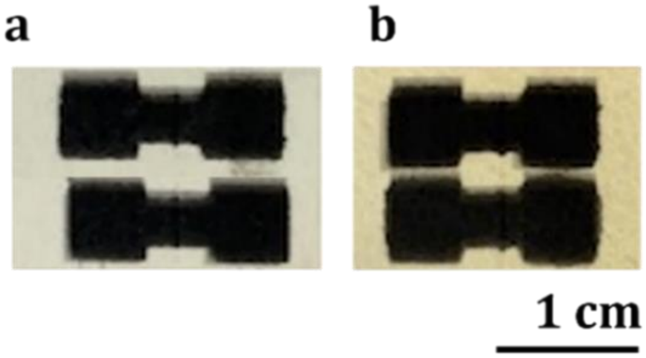

Figure 6.7: CNTs electrode sensor on a) 5 W, and b) 20 W AAm-PFC filter paper (10 min, 2 x 10 $^{-1}$ mbar)

As shown in **Figure 6.7**, CNTs ink was successfully deposited onto AAm-PFC filter paper (5 W and 20 W). Both fabricated CNTs electrode sensors show similar CNTs printing consistency. The CNTs distribution has been confirmed by the XPS in the previous section, indicating that the CNTs deposition is likely to be similar.

In comparing **Figure 6.7** with **Figure 5.12** (*section 5.3.4.3, Chapter 5*), the fabricated electrode sensor on AAm-PFC filter papers was more accurate and precise, with higher printing consistency than on AA-PFC filter papers. Generally, this indicates higher CNTs ink compatibility on AAm-PFC filter paper than on AA-PFC filter paper. Therefore, it is likely to provide higher conductivity than AA-PFC filter paper.

Encouragingly, compared to the CNTs electrode sensor on untreated filter paper, **Figure 3.12** (*section 3.3.2.2.2, Chapter 3*), the CNTs printing performance appears very similar. Therefore, resistance measurements are carried out in *section 6.3.3* to confirm this statement.

6.3.3 Resistance Measurement of the Fabricated Electrode Sensor on 5 W AAm-PFC Filter Paper

Figure 6.8 shows the resistance of the fabricated CNTs electrode sensors on untreated filter paper, 5 W AA-PFC, and 5 W and 20 W AAm-PFC filter papers with respect to the distance between probes.

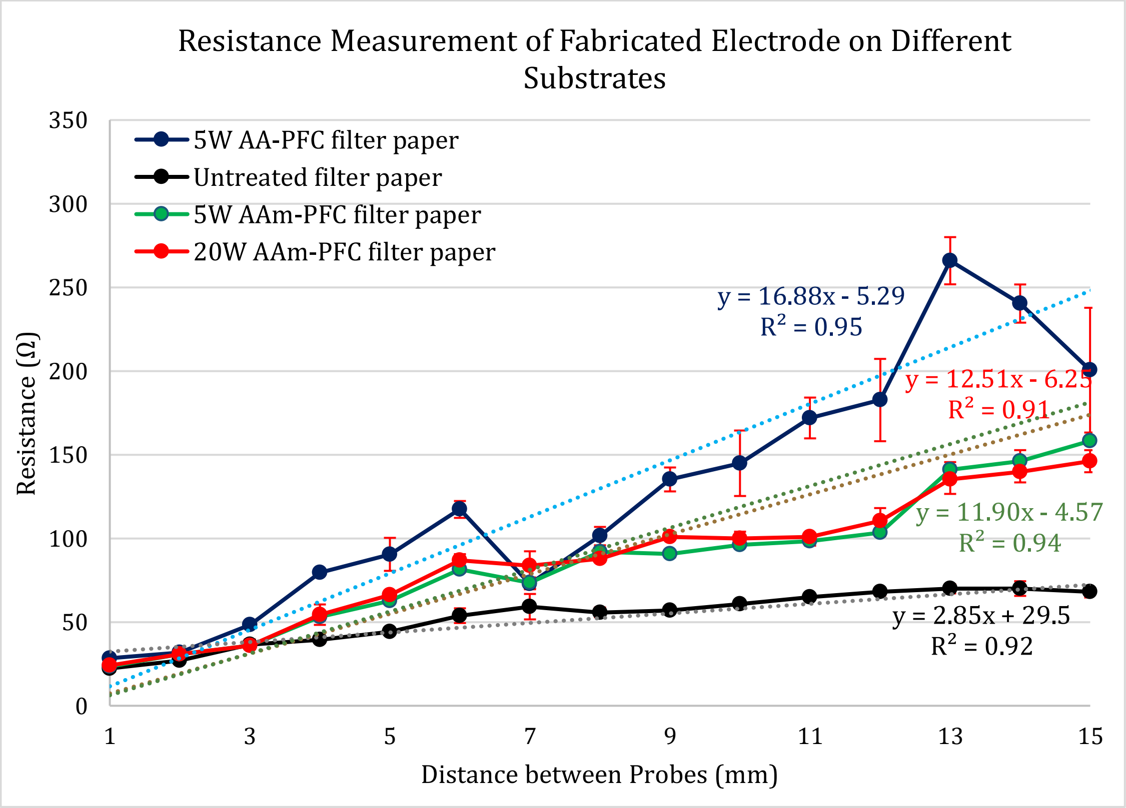

Figure 6.8: Resistance measurement of the fabricated electrode on untreated filter paper, 5 W AAm-PFC filter paper and 5 W AA- filter paper

Figure 6.8 shows similar trends for all fabricated electrode sensors, where the resistance increases with the length between probes. The resistance of CNTs electrode sensors on 5 W AAm-PFC filter paper (11.90 ± 0.31 kΩm) and 20 W AAm-PFC filter paper (12.51 ± 0.36 kΩm) is lower than on 5 W AA-PFC filter paper (16.88 ± 3.85 kΩm); indicating higher conductivity. However, the specific resistivity of the CNTs electrode sensor on AAm-PFC filter paper remains higher than on untreated filter paper (2.85 ± 0.30 kΩm). Whilst CNTs electrode sensors fabricated on AAm plasma-treated filter paper may be more of higher fidelity than AA, and the AAm surface is more durable for printing, overall, the printed electrode is still less conductive and accurate than on untreated filter paper.

The hypothesis is that the fidelity of printing correlates with the NH_2 surface concentration and is not directly supported by the C1s fit (21-22% C-N in both PPs). It is possible that there is scrabbling of primary amine to other C-N functionalities in the plasma, which would be more marked at higher plasma power. This hypothesis can be tested by surface labelling with TFBA (part of future work). A further investigation is required to optimise the PP process and coating conditions to improve CNTs deposition and printing accuracy: In our lab group, we have recently shown that NH_2 concentration can be significantly enhanced by plasma deposition at low power (5.5 W) and high pressure (2×10^{-1} mbar). Further testing of this hypothesis will be part of future work and is beyond the scope of this thesis.

6.4 Conclusion

The technique of PP was utilised to coat AAm on PFC-coated filter paper on Whatman filter paper grade 3 to enhance the CNTs ink compatibility for paper-based CNTs electrode sensor fabrication compared to AA coating (*Chapter 5*). Various analytical and characterisation techniques, including CA measurement, XPS, and resistance measurements, were utilised to assess the effect of AAm on filter paper.

Two different power discharges were tested to identify the most appropriate coating for CNTs printing. The CA reduced in all coating conditions, especially at the 5 W coating condition, where the CA decreased from 120.59° ± 2.67 and 104.67 ° ± 1.24 to 18.6 °± 6.8 and 14.9 °± 6.1 for DI water and CNTs ink. The CAs were lower than on AA-PFC filter paper, indicating better CNTs ink compatibility. The XPS spectra of AAm-PFC filter paper showed an introduction of N content, indicating the potential possibility of AAm-coating. The XPS also revealed that in both PPs, the presence of C-N indicates that there may be primary amines on the substrate surface. In the case of CNTs printed AAm-PFC filter paper, F content was detected on all power discharges, especially on 20 W; this may reflect thinner AAm-coating, or more F sputtering at 20 W. It is suspected that the coating is thinner since there are CF2 and CF3 in the C1s of 20 W AAm-PFC filter paper.

The specific resistivity of the CNTs electrode sensor on 5 W AAm-PFC filter paper (11.90 ± 0.31 kΩm) was lower than on 5 W AA-PFC filter paper (16.88 ± 0.99 kΩm) but higher than on untreated filter paper. Therefore, it can be concluded that AAm coating is more compatible with CNTs electrode sensor fabrication than AA coating. CNTs electrode sensor on AAm-PFC filter paper provides high durability and conductivity. However, further studies on AAm coating conditions are required to enhance CNTs printing and electrode fabrication performances.

7 Conclusions

The major objective of this research is to fabricate highly durable paper-based CNTs electrode sensors using a home inkjet printer (Canon PIXMA TS205). Various analytical and characterisation techniques, including SEM characterisation, XPS characterisation, CA measurement, ASV analysis and resistance measurement, were utilised to assess the fabricated CNTs electrode sensors.

Different CNTs ink formulations were examined to identify the most compatible ink formulation for paper-based CNTs electrode sensor fabrication. Pristine-MWCNT-COOH with SDS surfactant dispersed in DI water was found to provide optimal homogeneity and inkjet printer compatibility. The specific resistivity of the fabricated CNTs electrode sensor on Whatman filter paper grade 1 is 1.78 ± 0.11 kΩm. However, the fabricated CNTs electrode sensors on Whatman filter paper grade 1 suffered from CNTs ink spreading out of the designated area due to the paper thickness and ink adsorption; therefore, different types of paper substrates were investigated to overcome this challenge.

Among all the investigated paper substrates, Whatman filter paper grade 3 provided the optimal CNTs printing efficiency. The fabricated CNTs electrode sensors on Whatman filter paper grade 3 provided a specific resistivity of 2.85 ± 0.30 kΩm. SEM images showed high CNTs connectivity and distribution at approximately 117.4 ± 4.6 CNT/μm^2. XPS confirmed the deposition of CNTs onto Whatman filter paper grade 3. ASV analysis was utilised to observe the detection performance of the fabricated electrode sensors. However, the sensors suffered from poor durability and stability due to water absorption and filter paper degradation, making the electrode sensors inappropriate for multiple uses. Therefore, PP was utilised to overcome this issue.

PP of PFC and AA on Whatman filter paper grade 3 was performed. PFC was successfully coated onto the filter paper and introduced hydrophobic characteristics onto the paper substrate, stopping water ingress into the filter paper to overcome the degradation in an aqueous environment. The CA of DI water and CNTs ink increased from 0.00° to 120.59° ± 2.67 and 104.67 ° ± 1.24 for DI water and CNTs ink, respectively, confirming the PFC-coating on the substrate surface. XPS characterisation shows an increase in F content and a decrease in O content, confirming that PFC introduces hydrophobic characteristics onto the paper surface and repels an aqueous solution.

To allow CNTs printing for electrode sensor fabrication, AA was plasma polymerised onto PFC-coated filter paper. The CA reduced to 66.59° ± 8.04 and 41.45° ± 3.36 for DI water and CNTs ink, respectively, upon AA-coating. This confirms the AA-coating. The XPS spectra of AA-PFC filter paper showed an increase in O content and a decrease in F content, confirming the presence of the AA layer. From the CA measurement and XPS characterisation, 5 W AA-coating on PFC filter paper resulted in having the lowest CA and most AA-coating; therefore, it was selected for CNTs electrode sensor fabrication. The fabricated CNTs electrode sensors on a 5 W AA-PFC filter paper resulted in having approximately 16.88 ± 0.99 kΩm, which is higher than on untreated filter paper. Furthermore, the CNTs printing accuracy is not as efficient as on untreated filter paper; therefore, further investigation will be required to improve the CNTs printing and electrode fabrication efficiency.

Since there were challenges in fabricating CNTs electrode sensors on AA-PFC filter paper, AAm-coating was examined to overcome this issue. AAm was plasma polymerised onto PFC filter paper. Lower CA was observed on AAm-PFC filter paper at 18.6 °± 6.8 and 14.9 °± 6.1 for DI water, and CNTs ink in the case of 5 W AAm-coating. XPS spectra of AAm-PFC filter paper showed the introduction of N content, confirming AAm-coating. The XPS also revealed that 5 W AAm-coating likely introduced more amine group onto the substrate than higher power; therefore, CNTs electrode sensors were fabricated onto a 5 W AAm-PFC filter paper. The fabricated electrode sensors on a 5 W AAm-PFC filter paper showed better CNTs printing performance than on a 5 W AA-PFC filter paper, with a specific resistivity of 11.90 ± 0.31 kΩm. The specific resistivity of CNTs on 5 W AAm-PFC filter paper was lower than on a 5 W AA-PFC filter paper but higher than on untreated filter paper.

It can be concluded that PP of PFC and AAm successfully enhanced the durability and stability of the fabricated CNTs electrode sensors in an aqueous environment while maintaining the CNTs printing efficiency to a reasonable extent. The fabricated CNTs electrode sensors on AAm-PFC filter paper were conductive and appropriate for further detection and application. Further investigation may be required to improve the plasma coating and the conductivity of the fabricated electrode sensors on the plasma-polymerised substrate; however, this will be part of the future work and beyond the scope of this thesis.

8 Future Works

According to this research project, these are the limitation experienced:

- The durability and stability of the fabricated CNTs electrode sensors on untreated filter paper are inappropriate for multiple uses in an aqueous environment. Application should therefore be for single-use sensors.
- The CNTs ink compatibility and printing efficiency on plasma-polymerised filter paper for CNTs electrode sensors fabrication are lower than on untreated filter paper
- The conductivity of fabricated CNTs electrode sensors on plasma-polymerised filter paper is lower than on untreated filter paper.
- The optimal PP condition for AA-coating and AAm-coating to reduce the CA of CNTs ink for electrode sensor fabrication is yet to be identified

Therefore, further studies should investigate:

- Possible factors that could improve the durability and stability of the fabricated electrode sensor on untreated filter paper, such as
    - Introducing a hydrophobic barrier on top of the printed electrode sensors.
    - Introducing flow channel to minimise sample solution and excess interaction with the electrode sensors
- Other possible polymers to enhance the plasma-polymerised filter paper compatibility with the CNTs ink.
- The optimal PP condition of AAm-coating to improve CNTs printing performance. The parameters that should be considered are pressure, plasma polymerisation time and power discharge. (e.g., PP of AAm at lower power and higher pressure)

  - Measuring the density of NH_2 group in AAm-PFC filter paper through labelling with TFBA
- Fabricated electrode sensors performance, including
  - Cyclic voltammetry analysis to study the electrochemical properties
  - ASV analysis to detect various target species to observe their detection performance
  - AFM characterisation to study the electrode mechanical properties
- Electrode sensors design, geometry, and complex electrode combinations, once optimal electrode sensors were achieved. For example, multi-layer printing could add mediator and enzyme layers for a single-use electrochemical (amperometric) biosensor, which may be able to compete with established screen-printed sensors.
- Ion-selective membrane preparation for inkjet printing on the fabricated CNTs electrode sensors for target species detection. For instance, an ion-selective electrode sensor for potassium ion detection where the printed addition of an ionophore-containing layer could provide a short-lived ion-selective membrane. This could be applied for single-use measurement of key ions in medical applications.

9 References

1 N. Anzar, R. Hasan, M. Tyagi, N. Yadav and J. Narang, *Sensors Int.*, 2020, **1**, 100003.

2 Nanotechnologies, https://ec.europa.eu/health/scientific_committees/opinions_layman/en/nanotechnologies/l-2/6-health-effects-nanoparticles.htm, (accessed 4 April 2022).

3 Basic of Nanotechnology, https://www.brighthubengineering.com/manufacturing-technology/104742-the-basics-of-nanotech/#:, (accessed 4 April 2022).

4 M. Rabbani, M. E. Hoque and Z. Bin Mahbub, in *Nanofabrication for Smart Nanosensor Applications*, eds. K. Pal and F. Gomes, Elsevier, 2020, pp. 163–186.

5 H. Araki, W. Yang, Q. Hu, H. Suzuki and T. Noda, in *Novel Materials Processing by Advanced Electromagnetic Energy Sources*, ed. S. Miyake, Elsevier Science Ltd, Oxford, 2005, pp. 369–372.

6 H. He, L. A. Pham-Huy, P. Dramou, D. Xiao, P. Zuo and C. Pham-Huy, *Biomed Res. Int.*, 2013, **2013**, 12.

7 Y. Zhang, T. Ren and J. He, *ACS Appl. Mater. Interfaces*, 2018, **10**, 11343–11349.

8 U. Cigane, A. Palevicius and G. Janusas, *J Mater Sci*, 2021, **56**, 13479–13498.

9 S. Zhu, H. Meng, Z. Gu and Y. Zhao, *Nano Today*, 2021, **39**, 3.

10 M. N. Tchoul, W. T. Ford, M. L. P. Ha, I. Chavez-Sumarriva, B. P. Grady, G. Lolli, D. E. Resasco and S. Arepalli, *Chem. Mater.*, 2008, **20**, 3120–3126.

11 S. Rathinavel, K. Priyadharshini and D. Panda, *Mater. Sci. Eng. B*, 2021, **268**, 115095.

12 M. N. Tchoul, W. T. Ford, M. L. P. Ha, I. Chavez-Sumarriva, B. P. Grady, G. Lolli, D. E. Resasco and S. Arepalli, *Chem. Mater.*, 2008, **20**, 3120–3126.

13 A. Eatermadi, H. Daraee, H. Karimkhanloo, M. Kouhi, N. Zarghami, A. Akbarzadeh, Y. H. M. Abasi and S. W. Joo, *Nanoscale Res. Lett.*, 2014, **9**, 393.

14 J. P. Salvetat-Delmotte and C. A. Rubio, *Carbon N. Y.*, 2002, **40**, 1729–2734.

15 D. D. Liana, B. Raguse, J. J. Gooding and E. Chow, *Sensors*, 2012, **12**, 11505–11526.

16 M. Sher, R. Zhuang, U. Demiri and W. Asghar, *Expert Rev. Mol. Diagn.*, 2017, **17**, 351–366.

17 N. A. Meredith, C. Quinn, D. M. Cate, T. H. Reilly and C. S. Volckens, I I I JHenry, *Analyst*, 2016, **141**, 1874–1887.

18 X. Q. He, S. Kitipornchai, C. M. Wang and K. M. Liew, *Int. J. Solids Struct.*, 2005, **42**, 6032–6047.

19 S. K. Park, Q. Mahmood and H. S. Park, *Nanoscale*, 2013, **5**, 12304–12309.

20 T. Akyazi, L. Basabe-Desmonts and F. Benito-Lopez, *Anal. Chim. Acta*, 2018, **1001**, 1–17.

21 Z. Lin, T. Le, X. Song, Y. Yao, Z. Li, K. Moon, M. M. Tentzeris and C. Wong, *J. Electron. Packag.*, 2013, **135**, 11001.

22 T. Wang, M. A. Roberts, I. A. Kinloch and B. Derby, *J. Phys D Appl Phys*, 2012, **45**, 15304–31531.

23 E. T. S. G. da Silva, S. Miserere, L. T. Kubota and A. Merkoci, *Anal. Chem.*, 2014, **86**, 10531–10534.

24 D. M. Cate, J. A. Adkins, J. Mettakoonpitak and C. S. Henry, *Anal. Chem.*, 2015, **87**, 19–41.

25 J. Li, F. Rossignol and J. Macdonald, *Lab Chip*, 2015, **15**, 2538–2558.

26 D. Hoath, *Fundamentals of Inkjet Printing: The Science of Inkjet and Droplets*, Wiley-vch, 2015.

27 R. Tortorich, H. Shamkhalichenar and J.-W. Choi, *Appl. Sci.*, 2018, **8**, 288.

28 M. Iqbal, D. K. Dinh, Q. Abbas, M. Imran, H. Sattar and S. A. U. Ahmad, 2019, **2**, 349–371.

29 N. Yadav, V. K. Garg, A. K. Chhillar and J. S. Rana, *Chemophere*, 2021, **280**, 1–24.

30 I. Khan, K. Saeed and I. Khan, *Arab. J. Chem.*, 2019, **12**, 908–931.

31 T. Sahu, Y. K. Ratre, S. Chauhan, L. V. K. S. Bhaskar, M. P. Nair and H. K. Verma, *J. Drug Deliv. Sci. Technol.*, 2021, **63**, 7.

32 M. Nasrollahzadeh, S. M. Sajadi, M. Sajjadi and Z. Issaabadi, *Interface Sci. Technol.*, 2019, **28**, 113–143.

33 O. M. Ikumapayi, E. T. Akinlabi, A. O. M. Adeoye and S. O. Tatoba, *Mater. Today Proceeding*, 2021, **44**, 1154–1162.

34 G. Guisbiers, S. M. Rosales and F. L. Deepak, *J. Nanomater.*, 2012, **2012**, 1–2.

35 A. Ojha, *Waterborne Pathog.*, 2020, 385–432.

36 E. Mostafavi, P. Soltantabar and T. J. Webster, *Biomater. Transl. Med.*, 2019, 191–212.

37 K. W. Cho, S. H. Sunwoo, Y. J. Hong, J. H. Koo, J. H. Kim, S. Baik, T. Hyeon and D. H. Kim, *Chem. Rev.*, 2022, **122**, 5068–5143.

38 R. J. B. Pinto, D. Bispo, C. Vilela, A. M. P. Botas, R. A. S. Ferreira, A. C. Menezes, F. Campos, H. Oliveira, M. H. Abreu, S. A. O. Santos and C. S. R. Freire, *Materials (Basel).*, 2020, **13**, 223–228.

39 D. Vllasaliu and I. Singh, *Eur. Pharm. Rev.*, 2014, **4**, 1360–8606.

40 R. D. Cançado and M. Muñoz, *Rev. Bras. Hematol. Hemoter.*, 2011, **33**, 461–469.

41 X. Hou, T. Zaks, R. Langer and Y. Dong, *Nat. Rev. Mater.*, 2021, **6**, 1078–1094.

42 A. Augustine, R. Augustine, A. Hasan, V. Raghuveeran, D. Rouxel, N. Kalarikkal and S. Thomas, *J. Mater. Sci. Mater. Med.*, 2019, **30**, 96.

43 A. I. Martínez-Banderas, A. Aires, M. Quintanilla, J. A. Holguín-Lerma, C. Lozano-Pedraza, F. J. Teran, J. A. Moreno, J. E. Perez, B. S. Ooi, T. Ravasi, J. S. Merzaban, A. L. Cortajarena and J. Kosel, *ACS Appl. Mater. Interfaces*, 2019, **11**, 43976–43988.

44 M. A. Doucey and S. Carrara, *Trends Biotechnol.*, 2019, **37**, 86–99.

45 F. Gu, L. Zhang, X. Yin and L. Tong, *Nano Lett*, 2008, **8**, 2757–2761.

46 D. Wang, B. Zhu, X. He, Z. Zhu, G. Hutchins, P. Xu and W. N. Wang, *Environ. Sci. Nano*, 2018, **5**, 1096–1106.

47 V. Scardaci, *Appl. Sci.*, 2021, **11**, 8035–8051.

48 S. K. Godlaveeti, H. Maseed, D. P. Shaik, E. A. Al-Ammar, A. M. Tighezza, M. Sillanpaa, A. R. Somala and R. R. Nagireddy, *Int. J. Hydrogen Energy*, 2022, **47**, 15571–15582.

49 S. Abdalla, F. Al-Marzouki, A. A. Al-Ghamdi and A. Abdel-Daiem, *Nanoscale*

Res. Lett., 2015, **10**, 358.

50 G. Anagnostopoulos, P. N. Pappas, Z. Li, I. A. Kinloch, R. J. Young, K. S. Novoselov, C. Y. Lu, N. Pugno, J. Parthenios, C. Galiotis and K. Papagelis, *ACS Appl. Mater. Interfaces*, 2016, **8**, 22605–22614.

51 I. Singh and P. K. Mishra, *Mater. Today Proceeding*, 2020, **29**, 327–332.

52 M. Lorenzetti, G. Bernardini, T. Luxbacher, A. Santucci, S. Kobe and S. Novak, *Biomed. Mater.*, 2015, **10**, 045012.

53 W. C. Lin, S. H. Lee, M. Karakachian, B. Y. Yu, Y. Y. Chen, Y. C. Lin, C. H. Kuo and J. J. Shyue, *Phys. Chem. Chem. Phys.*, 2009, **11**, 6199–6204.

54 S. J. Stine, K. D. Popowski, T. Su and K. Cheng, *Curr Stem Cell Res Ther*, 2020, **15**, 674–684.

55 V. S. Nguyen, D. Rouxel and B. Vincent, *Ultrason. Sonochem.*, 2014, **21**, 149–153.

56 R. Goyal, M. Sharma and U. K. Amberiya, *Int. J. Eng. Res. Technol.*, 2014, **3**, 3001–3009.

57 J. Jeevanandam, A. Barhoum, Y. S. Chan, A. Dufresne and M. K. Danquah, *Beilstein J. Nanotechnol.*, 2018, **9**, 1050–1074.

58 Advantages & Disadvantages of Nanotechnology, https://smallbusiness.chron.com/advantages-disadvantages-nanotechnology-37398.html, (accessed 4 April 2022).

59 A. K. Hussein, *Renew. Sustain. Energy Rev.*, 2015, **42**, 460–476.

60 M. Allsopp, A. Walters and D. Santillo, *Nanotechnologies and nanomaterials in electrical and electronic goods: A review of uses and health concerns*, 2007.

61 S. B. Y. Saadeh and M. D. D. Vyas, *Am J Robot Surg*, 2014, **1**, 4–11.

62 I. A. Joubert, M. Geppert, S. Ess, R. Nestelbacher, G. Gadermaier, A. Duschl, A. C. Bathke and M. Himly, *NanoImpact*, 2020, **17**, 100201.

63 C. Li, H. Liu, Y. Sun, H. Wang., F. Guo, S. Rao, J. Deng, Y. Zhang, Y. Miao, C. Guo, J. Meng, X. Chen, L. Li, D. Li, H. Xu, H. Wang, C. Li and L. Jiang, *J. Mol. Cell Biol.*, 2009, **1**, 37–45.

64 P. C. Ray, H. Yu and P. P. Fu, *Env. Sci Heal. C Env. Carcinog Ecotoxicol Rev*, 2009, **27**, 1–35.

65 Introduction to Nanotechnology, https://nanogloss.com/nanotechnology/advantages-and-disadvantages-of-nanotechnology/, (accessed 5 April 2022).

66 T. Fredriksson, Karlstads University, 2014.

67 N. Saifuddin, A. Z. Raziah and A. R. Junizah, *J. Chem.*, 2013, **2013**, 1–18.

68 P. Poncharal, C. Berger, Y. Yi, Z. L. Wang and W. A. De Heer, *J. Phys. Chem. B*, 2002, **106**, 12104–12118.

69 E. Goldbeum, University at Buffalo, 2009.

70 A. Eatesmadi, H. Dararee, H. Karimkhanloo, M. Kouhi, N. Zarghami, A. Akbarzadeh, M. Abasi, Y. Hanifehpour and S. W. Joo, *Nanoscale Res. Lett.*, 2014, **9**, 393.

71 B. Ribeiro, E. C. Botelho, M. L. Costa and C. F. Bandeira, *Polimeros*, 2017, **27**, 247–255.

72 J. Pitroda, B. Jethwa and S. K. Dave, *Int. J. Constr. Res. Civ. Eng.*, 2016, **2**, 36–42.

73 Y. Ando, X. Zhao, H. Shimoyama, G. Sakai and K. Kaneto, *Int. J. Inorg. Mater.*, 1999, **1**, 77–82.

74 M. A. Fraga, R. S. Pessoa, D. C. Barbosa and V. J. T. Airoldi, *Sensors Mater.*, 2017,

29, 39–56.

75 P. Jindal and V. K. Jinal, *J. Comput. Theor. Nanosci.*, 2006, **3**, 148–152.

76 J. H. Ahn, D. H. Kim and J. A. Rogers, *Compr. Semicond. Sci. Technol.*, 2011, **1–6**, 499–526.

77 A. El-Sayed, A. El-Mottaleb, A. Rubio and N. Zabala, 2009, 1–23.

78 Carbon nanotubes, https://www.cheaptubes.com/product-category/multi-walled-carbon-nanotubes/, (accessed 7 April 2022).

79 K. Ahn, S. Kim and I. J. Yu, *Saf Heal. Work*, 2011, **2**, 65–69.

80 M. Shigeta, K. Kamiya, M. Uejima and S. Okada, *Jpn. J. Appl. Phys.*, 2015, **54**, 35101–35104.

81 A. Aqel, K. M. M. Abou El-Nour, R. A. A. Ammar and A. Al-Warthan, *Arab. J. Chem.*, 2012, **5**, 1–23.

82 Y. Kanai, V. R. Khalap, P. G. Collins and J. C. Grossman, *Phys. Rev. Lett.*, 2010, **104**, 066401–4.

83 J. Klinovaja, M. J. Schmidt, B. Braunecker and D. Loss, *Phys. Rev. B*, 2011, **84**, 85452–85474.

84 A. Lekawa-Raus, J. Patmore, L. Zurzepa, J. Bulmer and K. Koziol, *Adv. Funct. Mater.*, 2014, **24**, 3661–3682.

85 L. A. Algharagholy, *J. Electron. Mater.*, 2019, **48**, 2301–2306.

86 N. Saito, H. Haniu, Y. Usui, K. Aoki, K. Hara, S. Takanashi, M. Shimizu, N. Narita, M. Okamoto, S. Kobayashi, H. Nomura, H. Kato, N. Nishimura, S. Taruta and M. Endo, *Chem. Rev.*, 2014, **114**, 6040–6079.

87 S. Marchesan, K. Kostarelos, A. Bianco and M. Prato, *Mater. Today*, 2015, **18**,

12–19.

88 Q. He, S. Guo, Z. Qian and X. Chen, *Chem. Soc. Rev.*, 2015, **44**, 6258–6286.

89 M. Utsav, *Int. Conf. Nanotechnol.*, 2014, 679–681.

90 B. Sitharaman, M. Van Der Zande, J. S. Ananta, X. Shi, A. Veltien, X. F. Walboomers, L. J. Wilson, A. G. Mikos, A. Heerschap and J. A. Jansen, *J. Biomed. Mater. Res. - Part A*, 2010, **93**, 1454–1462.

91 J. Y. Hwang, U. S. Shin, W. C. Jang, J. K. Hyun, I. B. Wall and H. W. Kim, *Nanoscale*, 2013, **5**, 487–497.

92 Y. Cao, Y. M. Zhou, Y. Shan, H. X. Ju and X. J. Xue, *J. Nanosci. Nanotechnol.*, 2007, **7**, 447–451.

93 N. Saito, T. Okada, H. Horiuchi, N. Murakami, J. Takahashi, M. Nawata, H. Ota, K. Nozaki and K. Takaoka, *Nat. Biotechnol.*, 2001, **19**, 332–335.

94 B. Pei, W. Wang, N. Dunne and X. Li, *Applications of carbon nanotubes in bone tissue regeneration and engineering: Superiority, concerns, current advancements, and prospects*, 2019, vol. 9.

95 E. Bekyarova, Y. Ni, E. B. Malarkey, V. Montana, J. L. McWilliams, R. C. Haddon and V. Parpura, *J Biomed Nanotechnol*, 2005, **5**, 3–17.

96 R. Das, Carbon Nanotubes (CNT) for Electronics & Electrics 2013-2013: Forecasts, Applications, https://www.idtechex.com/en/research-report/carbon-nanotubes-cnt-for-electronics-and-electrics-2013-2023-forecasts-applications-technologies/342, (accessed 20 April 2022).

97 S. Zhu, J. Shen, Y. Chen, J. Ni and Y. Li, *Natl. Sci. Rev.*, 2021, **8**, 261–278.

98 C. Luo, H. Xie, Q. Wang, G. Luo and C. Liu, *J. Nanomater.*, 2015, **2015**, 1–16.

99 Z. Xiao, J. Elike, A. Reynolds, R. Moten and X. Zhao, *Microelectron. Eng.*, 2016,

164, 123–127.

100 M. Mitra, *J. Electron. Res. Appl.*, 2018, **2**, 5–17.

101 Y. Cheng and O. Zhou, *Physique*, 2003, **4**, 1021–1033.

102 A. Nojeh, *ISRN Nanomater.*, 2014, **2014**, 1–23.

103 Applications of Carbon Nanotubes, https://www.azonano.com/article.aspx?ArticleID=4842, (accessed 30 June 2022).

104 C. W. Tan, K. H. Tan, Y. T. Ong, A. B. Mohamed, S. H. S. Zein and S. H. Tan, *Env. Chem Lett*, 2012, **10**, 265–273.

105 V. Schroeder, S. Savagatrup, M. He, S. Lin and T. M. Swager, *Chem Rev.*, 2019, **119**, 599–663.

106 M. Rajabi, K. Mahanpoor and O. Moradi, *Rsc Adv*, 2017, **7**, 47083–47090.

107 D. C. D. S. Alves, B. Healy, L. A. D. A. Pinto, T. R. S. A. Cadaval and C. B. Breslin, *Molecules*, 2021, **26**, 594–639.

108 M. M. A. Aslan, H. W. Kuo, W. Den, M. Usman, M. Sultan and H. Ashraf, *Sustainability*, 2017, **13**, 5717–5771.

109 J. Ma, L. Hou, G. Wu, L. Wang, X. Wang and L. Chen, *Materials (Basel).*, 2020, **13**, 2743–5729.

110 R. P. Tortorich and J. Choi, *Nanomaterial*, 2013, **3**, 453–468.

111 O. V. Kharissova, B. I. Karisov and E. G. C. Ortiz, *Rsc Adv.*, 2013, **3**, 24812–24852.

112 L. T. M. Hoa, *Diam. Relat. Mater.*, 2018, **89**, 43–51.

113 T. Wang, M. A. Robert, I. A. Kinloch and B. Derby, *J. Phys D Appl Phys*, 2012,

2012, 1432–1442.

114 S. Santangelo, G. Messina, G. Faggio, S. H. A. Rahim and C. Milone, *J. Raman Spectros*, 2012, **43**, 1432–1442.

115 B. M. Maciejewka, M. J. Delaporte, A. I. Vasylenko, K. K. Koziol and S. Jurga, *Rsc ADV.*, 2014, **4**, 28826–28831.

116 R. Yudianti, H. Onggo, Sudirman, Y. Saito, T. Iwata and J. Azuma, *Open Mater. Sci. J.*, 2011, **5**, 242–247.

117 K. Jagadish, S. Srikantaswamy, K. Byrappa, L. Shruthi and M. R. Abhilash, *J. Nanomater.*, 2015, **2015**, 381275–381281.

118 M. Ikeda, *Toxicol. Lett.*, 1992, **64–65**, 191–201.

119 S. Magdassu, *The Chemistry of Inkjet Inks*, World Scientific, 2009.

120 R. P. Tortorichm, Louisiana State Univeristy, 2014.

121 Y. Nakama, *Cosmet. Sci. Technol.*, 2017, 231–244.

122 V. A. Karachevtsev, A. Y. Glamazda, A. M. Plokhotnichenko, V. S. Leontiev and A. S. Linnik, *Maat-wiss U. Werkstofftech*, 2011, **42**, 41–46.

123 K. Wusiman, H. Jeong, K. Tulugan, H. Afrianto and H. Chung, *Int. Commun. Heat Mass Transf.*, 2013, **41**, 28–33.

124 H. Cui, X. Yan, M. Monasterio and F. Xing, *Nanomaterials*, 2017, **7**, 262–27.

125 W. Su, B. S. Cook, Y. Fang and M. M. Tentzeris, *Sci. Rep.*, 2016, **6**, 1–12.

126 M. S. Khan, D. Fon, X. Li, J. Tian, J. Forsythe, G. Garnier and W. Shen, *Colloids Surfaces B*, 2010, **75**, 441–447.

127 S. K. Eshkalak, A. Chinnappan, W. A. D. M. Jayathilaka, M. Khatibzadeh, E. Kowsari and S. Ramakrishna, *Appl. Mater. Today*, 2017, **9**, 372–386.

128 J. Brunahl, Royal Institute of Technology Stockholm, 2003.

129 V. B. C. Lee, N. F. Mohd-Naim, E. Tamiya and M. U. Ahmed, *Anal. Sci.*, 2018, **34**, 7–18.

130 H. Lee, M. K. Joyce, P. D. Fleming and J. H. Cameron, *No Title*, H. Cameron, TAPPI Coating Conference, 2002.

131 A. Arena, N. Donato, G. Saitta, A. Bonavita, G. Rizzo and G. Neri, *Sensors Actuators B Chem.*, 2010, **145**, 488–494.

132 Y. Zhou, Y. Wu, L. Ding, X. Huang and Y. Xiong, *TrAC - Trends Anal. Chem.*, 2021, **145**, 116452.

133 B. Merrick, M. Noronha, R. Batra, S. Douthwaite, G. Nebbia, L. B. Snell, S. Pickering, R. P. Galao, J. Whitfield, A. Jahangeer, R. Gunawardena, T. Godfrey, R. Laifa, K. Webber, P. R. Cliff, E. Cunningham, S. J. D. Neil, H. Gettings, J. D. Edgeworth and H. L. Harrison, *Infect. Prev. Pract.*, 2021, **3**, 100186.

134 M. Z. Hua, S. Li, S. Wang and X. Lu, *Micromachines*, 2018, **9**, 1–14.

135 P. Vanysek, H. Tavassol and K. Pilson, *Electrochem. Soc.*, 2013, 224.

136 K. T. J. Smith and J. Stevenson, *Handb. Electrochem.*, 2007, 73–110.

137 Autolab Application Note EC08, 2011, 1–3.

138 Gamry Instrument, Potentiostat Fundamental, https://www.gamry.com/application-notes/instrumentation/potentiostat-fundamentals/, (accessed 30 June 2022).

139 W. Kit-Anan, A. Olarnwanich, C. Sriprachuabwong, C. Karuwan, A. Tuantranont, A. Wisitsoraat, W. Srituravanich and A. Pimpin, *J. Electroanal. Chem.*, 2012, **685**, 72–78.

140 N. R. Stradiotto, H. Yamanaka and M. V. B. Zanoni, *J. Braz. Chem. Soc.*, 2003,

14, 159–173.

141 J. Oh and K. Chow, *Anal. Methods*, 2015, **19**, 7951–7960.

142 Z. Nie, C. A. Nijhuis, J. Gong, X. Chen, A. Kumachev, A. W. Martinez, M. Narovlyansky and G. M. Whitesides, 2010, **10**, 477–483.

143 da C. E. Song, R. P. Tortorich and J. Choi, *ECS J. Solid State Sci. Technol.*, 2015, **4**, 3044–3047.

144 J. D. Whittle, University of Sheffield, 2000.

145 M. Shen and A. T. Bell, *Plasma Polymerisation*, American Chemical Society, 1979.

146 H. Yasuda and Y. Iriyama, *Compr. Polym. Sci. Suppl.*, 1989, **4**, 357–375.

147 H. J. Jang, E. Y. Jung, T. Parsons and C. S. Tae, H SPark, *Polymers (Basel).*, 2021, **13**, 2267–2275.

148 H. J. Jang, E. Y. Jung, T. Parsons, H. S. Tae and C. S. Park, *Polymers (Basel).*, 2021, **13**, 2267–2294.

149 A. A. Zuber, University of South Australia, 2012.

150 P. Raghavendra and T. Pullaiah, *Adv. Cell Mol. Diagnostics*, 2022, **13**, 85–111.

151 S. Lata, S. Chakravorty, T. Mitra, P. K. Pradhan, S. Mohanty, P. Patel, E. Jha, P. K. Panda, S. K. Verma and M. Suar, *Mater. Today Bio*, 2022, **13**, 100200.

152 F. L. Tabares and I. Junkar, *Molecules*, 2021, **26**, 1903–1919.

153 J. Carneiro de Oliveira, A. Airoudj, P. Kunemann, F. Bally-Le Gall and V. Roucoules, *SN Appl. Sci.*, 2021, **3**, 656.

154 M. Macgregor and K. Vasilev, *Materials (Basel).*, 2019, **12**, 191–209.

155 L. Martocq and T. E. L. Douglas, *Coatings*, 2021, **11**, 983–1002.

156 Y. Ucar, Z. Ceylan, M. Durmus, O. Tomar and T. Cetinkaya, *Trends Food Sci. Technol.*, 2021, **114**, 355–371.

157 B. A. Niemira, *Annu. Rev. Food Sci. Technol.*, 2012, **3**, 125–142.

158 P. Gururani, P. Bhatnagar, B. Bisht, V. Kumar, N. C. Joshi, M. S. Tomar and B. Pathak, *Environ. Sci. Pollut. Res.*, 2021, **28**, 65062–65082.

159 A. Michelmore, D. A. Steele, J. D. Whittle, J. W. Bradley and R. D. Short, *RSC Adv.*, 2013, **3**, 13540–13557.

160 A. Asad, D. Sameoto and M. Sadrzadeh, *Micro Nano Technol.*, 2020, 1–28.

161 S. Ligot, E. Bousser, D. Cossement, J. Klemberg-Sapieha, P. Viville, P. Dubois and R. Snyders, *Plasma Process. Polym.*, 2015, **12**, 508–518.

162 G. Aziz, N. De Geyter and R. Morent, in *Advances in Bioengineering*, ed. P. A. Serra, IntechOpen, Rijeka, 2015.

163 Y.-W. Jeong, S. Jung, J. J. Han, H.-J. Park, R. Y. Kim, B.-H. Kim and M.-S. Kook, *Mater. (Basel, Switzerland)*, 2019, **12**, 2581–2597.

164 X. Liu, Q. Feng, A. Bachhuka and K. Vasilev, *ACS Appl. Mater. Interfaces*, 2014, **6**, 9733–9741.

165 F. Bally-Le Gall, A. Mokhter, S. Lakard, S. Wolak, P. Kunemann, P. Fioux, A. Airoudj, S. El Yakhlifi, C. Magnenet, B. Lakard and V. Roucoules, *Plasma Process. Polym.*, 2019, **16**, 1800134.

166 J. B. Nebe, H. Rebl, M. Schlosser, S. Staehlke, M. Gruening, K. D. Weltmann, U. Walschus and B. Finke, *Polymers (Basel).*, 2019, **11**, 1004–1033.

167 K. L. Jarvis and P. Majewski, *Plasma Process. Polym.*, 2013, **10**, 619–626.

168 J. H. Zhao, W. P. Michalski, C. Williams, L. Li, H.-S. Xu, P. R. Lamb, S. Jones, Y. M. Zhou and X. J. Dai, *J. Biomed. Mater. Res. Part A*, 2011, **97A**, 127–134.

169 J. Naderi, C. Giles, S. Saboohi, H. J. Griesser and B. R. Coad, *Biointerphases*, 2020, **15**, 61012.

170 D. Mangindaan, W.-H. Kuo, C.-C. Chang, S.-L. Wang, H.-C. Liu and M.-J. Wang, *Surf. Coatings Technol.*, 2011, **206**, 1299–1306.

171 R. Bitar, P. Cools, N. De Geyter and R. Morent, *Appl. Surf. Sci.*, 2018, **448**, 168–185.

172 A. Manakhov, M. Michlíček, D. Nečas, J. Polčák, E. Makhneva, M. Eliáš and L. Zajíčková, *Surf. Coatings Technol.*, 2016, **295**, 37–45.

173 S.-C. Liao, K.-S. Chen, J.-L. Chien, S.-C. Chen and W.-L. Lin, *Nanomater. (Basel, Switzerland)*, 2019, **9**, 941.

174 A. J. Beck, R. D. Short and A. Matthews, *Surf. Coatings Technol.*, 2008, **203**, 822–825.

175 M. Donegan and D. P. Dowling, *Surf. Coatings Technol.*, 2013, **234**, 53–59.

176 M. T. van Os, University of Twente, Enschede, The Netherland, 2000.

177 M. Sarmadi, *Int. Symp. Plasma Chem.*, 2013, **4**, 1–4.

178 A. Michelmore, J. D. Whittle, J. W. Bradley and R. D. Short, *Where Physics meets Chemistry, Thin Film Deposition from Reactive Plasma*, Frontiers of Chemical Science and Engineering 10, 2016, vol. 4.

179 C. W. Kan, *Active Coatings for Smart Textiles*, Woodhead Publishing, 2016.

180 S. Saboohi, B. R. Coad, A. Michelmore, R. D. Short and H. J. Griesser, *ACS Appl. Mater. Interfaces*, 2016, **8**, 16493–16502.

181 R. Sudhanshu, Indian Institute of Technology Patna, 2020.

182 F. A. Stevie and C. L. Donley, *J. Vac. Sci. Technol. A*, 2020, **38**, 063204.

183 C. D. Easton, C. Kinnear, S. L. McArthur and T. R. Gengenbach, *J. Vac. Sci. \& Technol. A*, 2020, **38**, 23207.

184 D. R. Baer and S. Thevuthasan, in *Handbook of Deposition Technologies for Films and Coatings*, ed. P. M. B. T.-H. of D. T. for F. and C. (Third E. Martin, William Andrew Publishing, Boston, 2010, pp. 749–864.

185 D. Briggs, *Surface Analysis of Polymers by XPS and Static SIMS*, Cambridge University Press, 1998.

186 N. P. van der Meulen and Z. Talip, in *Nuclear Medicine and Molecular Imaging*, ed. A. Signore, Elsevier, Oxford, 2022, pp. 133–142.

187 H. E. EXNER, in *Physical Metallurgy (Fourth Edition)*, eds. R. W. CAHN and P. HAASEN†, North-Holland, Oxford, Fourth Edi., 1996, pp. 943–1032.

188 X-RAY PHOTOELECTRON SPECTROSCOPY (XPS), https://www.mee-inc.com/hamm/x-ray-photoelectron-spectroscopy-xps/#:~:text=XPS is a surface sensitive,have relatively low kinetic energy., (accessed 24 August 2022).

189 M. Descostes, F. Mercier, N. Thromat, C. Beaucaire and M. Gautier-Soyer, *Appl. Surf. Sci.*, 2000, **165**, 288–302.

190 Carbon X-ray Photoelectron Spectra, Carbon Electron Configuration, and Other Elemental Information, https://www.thermofisher.com/uk/en/home/materials-science/learning-center/periodic-table/non-metal/carbon.html, (accessed 24 August 2022).

191 D. Briggs and G. Beamson, *Anal. Chem.*, 1992, **64**, 1729–1736.

192 A. P. Dementjev, A. de Graaf, M. C. M. van de Sanden, K. I. Maslakov, A. V Naumkin and A. A. Serov, *Diam. Relat. Mater.*, 2000, **9**, 1904–1907.

193 I. Muzammil, Y. Li and M. Lei, *Plasma Process. Polym.*, 2017, **14**, 1770019.

194 L. G. and T. J. McCarthy, *Langmuir*, 2006, **22**, 6234–6237.

195 P. Raghavendra and T. Pullaiah, *Adv. Cell Mol. Diagnostics*, 2018, 85–111.

196 W. G. Wong, *Principle of Electronic Communication Systems - Multimeter Measurements Explained | Electronic Design*, 2022.

197 P. Fielden, *Stripping Voltammetry - An Applications Case Study*, Lancaster University, Lancaster, 2019.

198 O. Abollino, A. Giacomino and M. Malandrino, in *Encyclopedia of Analytical Science (Third Edition)*, eds. P. Worsfold, C. Poole, A. Townshend and M. Miró, Academic Press, Oxford, Third Edit., 2019, pp. 238–257.

199 Whatman Grade 3 Qualitative Filter Paper, https://www.cytivalifesciences.com/en/us/shop/whatman-laboratory-filtration/cellulose-filter-papers/qualitative-standard-filter-paper/grade-3-qualitative-filter-papers-p-00207#tech-spec-table, (accessed 30 May 2022).

200 M. Barsbay, O. Guven, M. H. Stenzel, T. P. Davis, C. Barner-Kowollik and L. Barner, *Macromolecules*, 2007, **40**, 7140–7147.

201 L. M. Han, R. B. Timmons and W. W. Lee, *J. Vac. Sci. Technol. B Microelectron. Nanom. Struct.*, 2000, **18**, 799.

202 National Center for Biotechnology Information. PubChem Compound Summary for CID 7853, Allylamine, https://pubchem.ncbi.nlm.nih.gov/compound/Allylamine, (accessed 30 March 2022).

203 A. Choukourov, H. Biederman, D. Slavinska, L. Hanley, A. Grinevich, H. Boldyryeva and A. Mackova, *J. Phys. Chem. B*, 2005, **109**, 23086–23095.

204 A. Beck, J. Whittle, N. Bullett, P. Eves, S. Mcarthur and A. Shard, *Plasma Process. Polym.*, 2005, **2**, 641–649.

205 S. W. Myung and H. S. Choi, 2006, **23**, 505–511.

206 J. Petersen, T. Fouquet, M. Michel, V. Toniazzo, A. Dinia, D. Ruch and J. A. S. Bomfim, *ACS Appl. Mater. Interfaces*, 2012, **4**, 1072–1079.

207 M. S. E. Jagst, *Using Chemical Derivatization X-ray Photoelectron Spectroscopy (CD-XPS)*, 2011.

208 M. Kehrer, J. Duchoslav, A. Hinterreiter, M. Cobet, A. Mehic, T. Stehrer and D. Stifter, *Plasma Process. Polym.*, 2019, **16**, 1–8.

209 J. Petersen, T. Nicolas, J. Fouquet, M. Michel, V. Toniazzo, A. Dinia, D. Ruch and J. A. S. Bomfim, *ACS Appl. Mater. Interfaces*, 2015, **4**, 1–6.

210 M. Vandenbossche and D. Hegemann, *Curr. Opin. Solid State Mater. Sci.*, 2018, **22**, 26–38.

211 N. Fairley, V. Fernandez, M. Richard-Plouet, C. Guillot-Deudon, J. Walton, E. Smith, D. Flahaut, M. Greiner, M. Biesinger, S. Tougaard, D. Morgan and J. Baltrusaitis, *Appl. Surf. Sci. Adv.*, 2021, **5**, 100112.

10 Appendices

Appendix A Table of RSFs, Inkjet Printing Test, and CNTs Ink Formulation 148

Appendix B XPS Data and ASV Analysis 151

Appendix C DI Water and CNTs ink Droplet, AFM and XPS Characterisation 153

Appendix A. Table of RSFs, Inkjet Printing Test, and CNTs Ink Formulation

Table of Relative Sensitivity Factors (RSFs) [211]

Name	R.S.F
Si 2p	0.817
C 1s	1.0
S 2p	1.677
N 1s	1.8
O 1s	2.93
F 1s	4.43
Na 1s	8.52

Inkjet Printer Testing

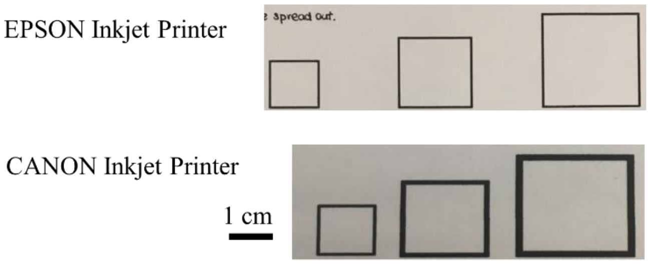

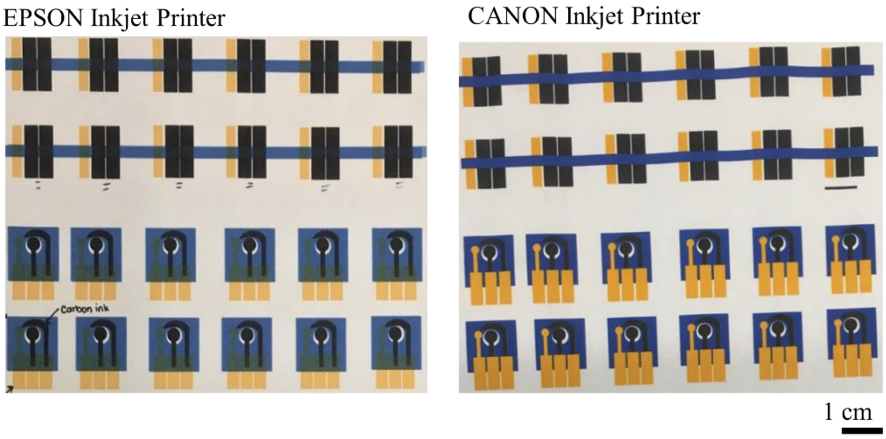

To confirm the performance of the inkjet printer, the inkjet printers filled with provided commercial inks were used to print several electrode templates. After several printing cycles, the repeatability remains precise and accurate vertically and horizontally. Therefore, this guarantees that the results obtained would still be accurate after multiple printing cycles. The minimum feasible distance between the electrodes is approximately 0.75 mm for both printers in terms of printer resolution. Nevertheless, the result may vary with the viscosity of the formulated ink.

MWCNTs Ink Formulation

Attempt #1 Sidewall Functionalization with Diluted Acid Mixture through Sonication

Diluted acids were prepared by diluting 98% sulfuric acid (H_2SO_4) and 70% nitric acid (HNO_3) to 10 M and 4 M, respectively.

108 mg pristine-MWCNTs were added into 15 mL of dilute H_2SO_4 and 5 mL of dilute HNO_3. The mixture was sonicated until homogenised at room temperature (**Attempt #1.1**) and 60°C (**Attempt #1.2**) and centrifuged at 4000 – 5000 rpm for 10 – 15 min. The supernatant was collected and vacuum filtered. The functionalised MWCNTs were dried overnight in the oven at 80 °C and dispersed in DI water (5 mg/mL). Finally, glycerol was added at a 1:3 ratio (glycerol: water) to adjust their viscosity and filtered with a 0.2 μm Millipore syringe filter to prevent nozzle clogging. The ink formulation was sonicated until homogenised and ready for printing.

Attempt #2 Sidewall Functionalization with Diluted Acid Mixture through Magnetic Stirrer

A 100 mg sample of pristine multi-walled carbon nanotubes (MWCNTs) was added into an acid mixture containing 15 mL of 10 M H_2SO_4 and 5 mL of 4 M HNO_3. The mixture was stirred vigorously at room temperature for 18 hours using a magnetic stirrer. After this process, the mixture was neutralised and vacuum filtered using DI water. The sample was dried in the oven at 80 °C overnight. Next, the dried sample was re-dispersed in water (5 mg/mL) and sonicated until homogenised. To adjust the viscosity of the ink, glycerol was added at the volume ratio of 1:3 (glycerol: water) and sonicated until homogenised, as reported in previous research 1. Finally, SDBS and SDS surfactants were added to improve the dispersion in a separate vial. The comparison between the two surfactants was studied to identify the most appropriate surfactant.

Attempt #3 Sidewall Functionalization with Concentrated Acid Mixture Through Sonication at Different Temperature

500 mg pristine-MWCNTs were added into a concentrated acid mixture of 10 mL of 98% H_2SO_4 and 5 mL of 70% HNO_3. The mixture was sonicated at room temperature (**Attempt #3.1**) and 60°C (**Attempt #3.2**) until homogenised, vacuum filtered, and until MWCNTs were completely neutral (pH 7). Next, Functionalized MWCNTs were dried in the oven overnight at 80 °C. Dried functionalised MWCNTs were collected and dispersed in DI water (5 mg/mL). Finally, glycerol was added at a 1:3 ratio (glycerol: water) and filtered with a 0.2 μm Millipore syringe filter. The ink formulation was sonicated until homogenised and ready for printing.

Attempt #4 Preparation of Pristine-MWCNTs in Aqueous Solution with SDS surfactant

140 mg SDS was mixed into the water solution and sonicated until homogenised. 200 mg pristine-MWCNTs was added to the solution mixture and sonicated for 30 minutes. The mixture was centrifuged at 5000 rpm for 5 - 10 min. The supernatant was collected and vacuum filtered. The sample was mixed in water solution to 5 mg/mL concentration.

Appendix B. XPS Data and ASV Analysis

Wide Spectra and C 1s Spectra of Untreated Glossy Photo Paper and Untreated Matte Photo Paper

Glossy Photo Paper

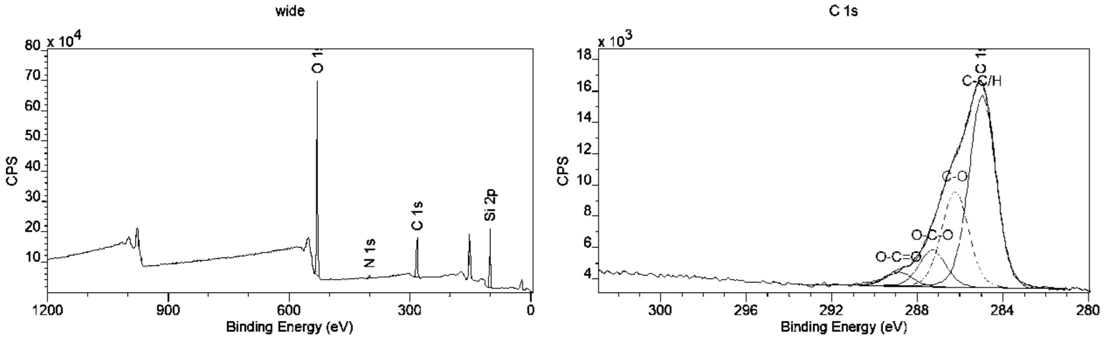

Matte Photo Paper

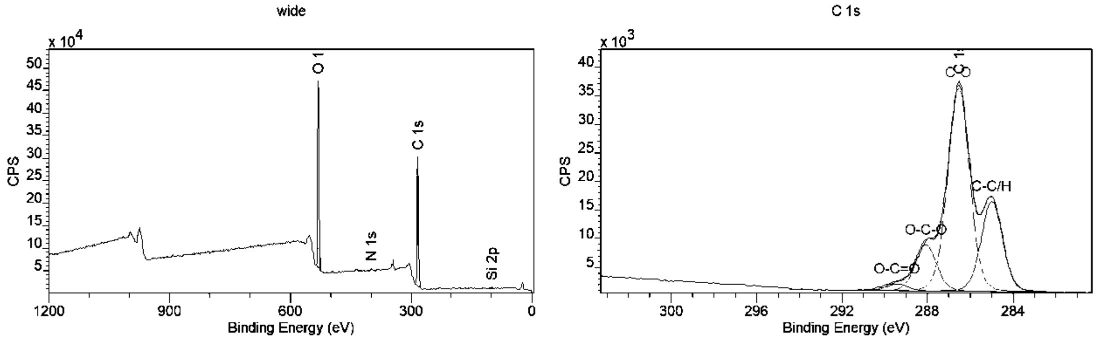

Wide Spectra

	C 1s	O 1s	N 1s	Si 2p
Premium glossy photo paper	12.9 %	68.1 %	0.6 %	18.4 %
Matte photo paper	65.8 %	32.8 %	0.9 %	0.5 %

C 1s Spectra

	C-C/H	C-O	O-C-O	O-C=O
BE (eV)	285.0	286.5	288.1	289.4
Glossy photo paper	56.8 %	28.3 %	10.8 %	4.1 %
Matte photo paper	26.1 %	58.7 %	13.3 %	2.0 %

ASV Analysis Using Commercial WE

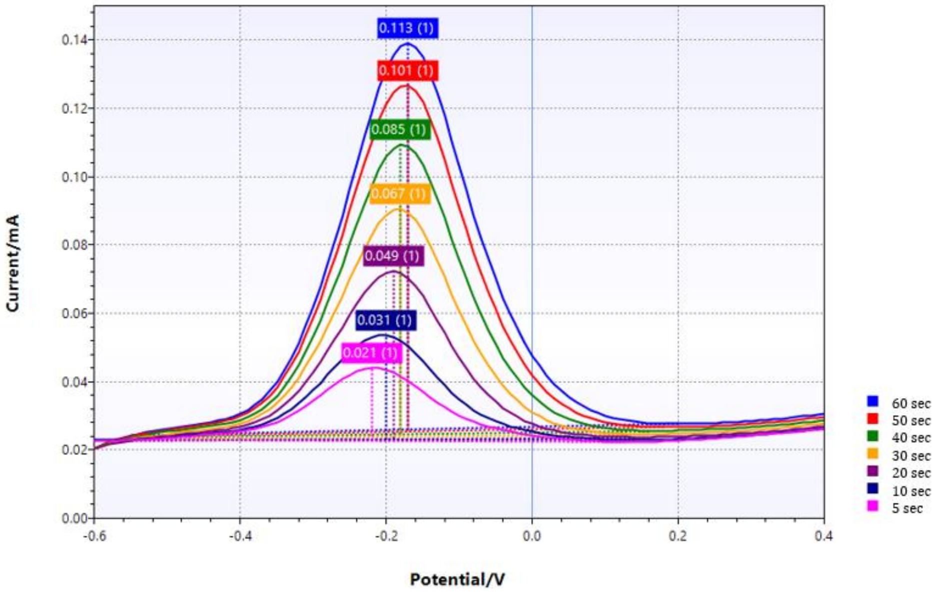

A commercial WE (screen printed carbon on PVC substrate) was used as a standard for ASV analysis to compare the detection performances of the fabricated paper based CNTs electrode sensor on Whatman filter paper grade 3. The results show the measurement at different deposition time (5 sec to 60 sec) and that the commercial WE are appropriate for multiple usage.

Appendix C. DI Water and CNTs ink Droplet, AFM and XPS Characterisation

DI Water and CNTs Ink Droplet

DI water

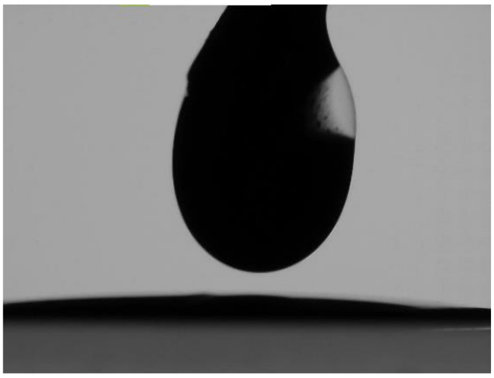

CNTs ink

AFM Characterisation of PFC-Coated Filter Paper

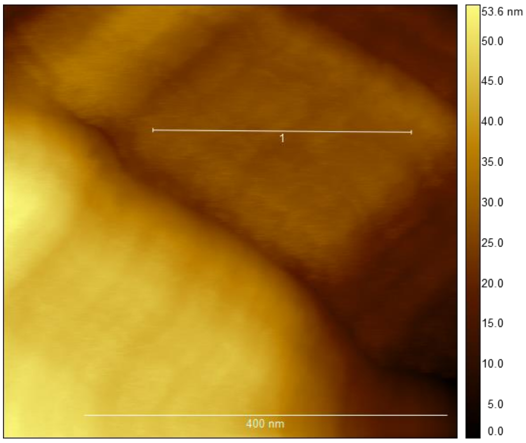

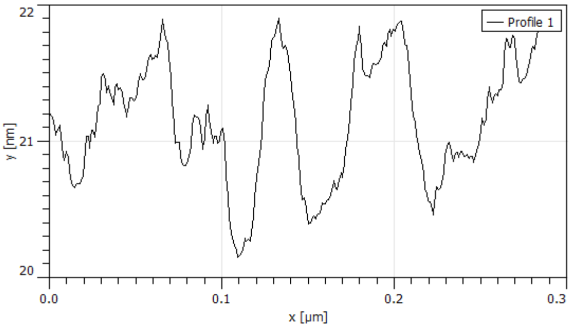

The height fluctuation is between -500 and 500 pm, similar to PFC on silicon wafers and glass.

XPS Characterisation of CNTs on Untreated, 5 W AA-PFC and 50 W AA-PFC Si Wafer

Wide Spectra

CNTs ink	C 1s	O 1s	F 1s	S 2p	Na 1s	Si 2p
Untreated Si wafer	71.9 %	11.6 %	-	4.0 %	1.3 %	11.2 %
5 W AA-PFC Si wafer	88.7 %	6.5 %	1.7 %	1.9 %	1.2 %	-
50 W AA-PFC Si wafer	65.0 %	6.7 %	27.3 %	0.6 %	0.4 %	-

C1s Spectra

CNTs ink	C=C	C-C/H	C-O	C=O	O-C=O	π-π*
BE (eV)	284.5	285.0	285.9	287.1	288.6	291.2
Untreated Si wafer	61.6 %	22.1 %	3.4 %	2.1 %	5.3 %	5.5 %
5 W AA-PFC Si wafer	79.1 %	8.3 %	5.0 %	3.0 %	2.3 %	2.4 %

The C 1s spectra of CNTs on a 50 W AA-PFC Si wafer show a combination of CNTs ink, AA and PFC, which indicates that the AA coatings do not mask all signals from the underlying PFC. This may result from thin CNTs and AA-coating or PFC sputtering.